

University of Heidelberg

Diploma thesis

in Physics

submitted by

Florian Wilken

born in Bonn

2006

Density Functional Treatment of Atomic Strong-Field Ionization Processes

This diploma thesis has been carried out by Florian Wilken at the
Max Planck Institute for Nuclear Physics
under the supervision of
Priv.-Doz. Dr. Dieter Bauer

Dichtefunktionaltheoretische Behandlung atomarer Ionisationsprozesse in starken Feldern

Zeitabhängige Dichtefunktionaltheorie liefert eine prinzipiell exakte Beschreibung eines zeitabhängigen Systems von Elektronen mittels der numerisch vorteilhaften Einteilchen-Kohn-Sham-Gleichungen. Dieser Ansatz trifft allerdings im Fall nichtsequentieller atomarer Ionisationsprozesse in starken Laserfeldern auf Schwierigkeiten. Um diesen zu begegnen untersuchen wir ein eindimensionales Helium-Modellatom in linear polarisierten Laserpulsen mit wenigen optischen Zyklen. Die zeitabhängige Schrödinger-Gleichung wird numerisch gelöst und dient als Referenz für eine dichtefunktionaltheoretische Behandlung des Problems. Die Dichtefunktionale für die Ionisationswahrscheinlichkeiten und die Impulsverteilung des Ions erweisen sich als fundamental wichtig. Wir führen Näherungen der exakten Funktionale ein, die die charakteristische “Kniestruktur” in der Doppelionisationswahrscheinlichkeit reproduzieren. Es werden wesentliche Fortschritte bei der Entwicklung eines korrelierten Funktionals für die Impulsverteilung des Ions erzielt. Mit Hilfe der Lösung der zeitabhängigen Schrödinger-Gleichung entdecken wir nichtsequentielle Doppelrekombination: Zwei Elektronen kehren zum Ion zurück und senden, bedingt durch ihre Wechselwirkung, ein einziges Photon aus. Dieser Effekt wird auch mit zeitabhängiger Dichtefunktionaltheorie untersucht und liefert eine wertvolle Referenz für genaue Austausch-Korrelations-Potentiale.

Density Functional Treatment of Atomic Strong-Field Ionization Processes

Time-dependent density functional theory can in principle describe a time-dependent electronic system exactly via the computationally advantageous Kohn-Sham scheme of one-electron equations. However, in the case of non-sequential ionization of atoms in strong laser fields this approach was found to face fundamental challenges. To address these we investigate a one-dimensional model Helium atom in linearly polarized few-cycle laser pulses. The time-dependent Schrödinger equation is solved numerically and serves as a reference for a time-dependent density functional treatment. The functional of the density for the ionization probabilities and the momentum distribution of the ion is found to be of central importance. We introduce approximations of the exact functionals which reproduce the characteristic “knee structure” in the double ionization probability. Significant progress towards a correlated functional for the momentum distribution of the ion is made. With the solution of the Schrödinger equation non-sequential double recombination is discovered: Two electrons return to the ion and, through interaction, emit a single photon upon recombination. This effect is also investigated using time-dependent density functional theory serving as a sensitive benchmark for accurate exchange-correlation potentials.

Contents

1	Introduction	1
2	Time-Dependent Density Functional Theory	5
2.1	The Runge-Gross Theorem	5
2.2	Time-Dependent Kohn-Sham Equations	7
3	Model System	11
3.1	Laser Pulses	11
3.2	Model Helium Atom	13
3.3	Time-Dependent Schrödinger Equation	13
3.4	TDDFT Approach	14
3.5	The exact Kohn-Sham orbital	16
3.6	Model He ⁺ Ion	17
3.7	Single-Active Electron Approach	17
4	Ionization Probabilities	19
4.1	Calculation of Ionization Probabilities	19
4.2	Ionization Probabilities from the TDSE	21
4.3	Ionization Probabilities from TDDFT	23
4.3.1	Uncorrelated Functionals	24
4.3.2	Comparison of Correlation Potentials	25
4.3.3	Correlated Functionals	27
4.3.4	Exact Correlation Integral	29
4.3.5	Approximation of the Correlation Integral	31
4.3.6	Becke Approximation	32
4.3.7	Adiabatic Approximation	34
4.3.8	Fit Function Approximation	39
5	Momentum Distributions	43
5.1	Calculation of the Momentum Pair Density	43
5.2	Calculation of the Ion Momentum Density	44
5.3	Classical Picture of Double Ionization	45
5.4	Momentum Distributions from the TDSE	46

5.4.1	Momentum Pair Density	46
5.4.2	Ion Momentum Density	46
5.5	Momentum Distributions from TDDFT	48
5.5.1	Uncorrelated Functionals	49
5.5.2	Comparison of Correlation Potentials	51
5.5.3	Towards Correlated Functionals	53
5.5.4	Product Phase Approximation	54
6	Non-Sequential Double Recombination	59
6.1	Classical Model	59
6.2	Calculation of High-Order Harmonic Spectra	61
6.3	High-Order Harmonic Spectra from the TDSE	63
6.4	High-Order Harmonic Spectra from TDDFT	67
7	Summary	71
A	Numerical Implementation	73
A.1	Time-Dependent Schrödinger Equation	73
A.2	Time-Dependent Kohn-Sham Equation	74
A.3	Discretization of the TDSE	74
A.4	Discretization of the TDKSE	76
A.5	Time-Propagation of the TDSE Wavefunction	76
A.5.1	Short-Time Propagator	76
A.5.2	Approximation of the Short-Time Propagator	77
A.5.3	Short-Time Propagator Splitting	77
A.5.4	Discretization of the Split Short-Time Propagator	79
A.5.5	Comparison of Different Splittings	80
A.6	Time-Propagation of the TDKSE Orbital	83
A.7	Groundstate Calculation	84
A.8	Absorbing Boundary Conditions	85
A.9	Parameters of Calculations	85

Chapter 1

Introduction

The last twenty years have seen a rapid progress in laser technology. Intensities in the focus of the laser of up to $I = 10^{22}$ W/cm² can be reached and laser fields of the strength of $I = 10^{17}$ W/cm² are produced routinely with table-top laser equipment. The range of wavelengths for which these intensities are achieved has expanded to $\lambda = 248$ nm-1 μ m (see Ref. [1] and references therein).

Furthermore, it has been possible to produce laser pulses of merely a few optical cycles [1], i.e., of femtosecond durations. Control over the temporal evolution of the electric field has been gained, allowing laser pulses to be described by a carrier wave and an envelope function. The phase between the envelope and the carrier wave can be measured and controlled [2,3]. With few-cycle driving pulses, it is now also possible to generate short attosecond ultraviolet pulses [4,5].

The electric field of the nucleus in an atom corresponds to intensities of just 10^{16} W/cm². With strong few-cycle laser pulses it is therefore possible to initiate (and to a certain extent control) various electronic processes.

A complementary development has been the advent of cold target recoil ion momentum spectroscopy [6] which allows to measure the momenta of the reaction products in laser-matter interactions, greatly enhancing the understanding of the underlying processes.

Among the vast range of phenomena resulting from the interaction of laser pulses and atoms (see Refs. [1, 5, 7, 8] for an introduction) we will study non-sequential double ionization and high-order harmonic generation in Helium in this work.

In measurements of the ionization yields of noble gas atoms interacting with intense laser fields, an enhanced production of doubly charged ions was observed. As a function of the intensity of the laser pulse, this process manifests itself in a “knee structure” of the double ionization yield [9,10] as depicted in the left part of Fig. 1.1. For intensities $I < 3 \times 10^{15}$ W/cm² the He²⁺ signal is orders of magnitudes higher than expected from a sequential mechanism where the electrons leave the atom one after another. Hence, strong interaction between the electrons has to be responsible for non-sequential double ionization (NSDI).

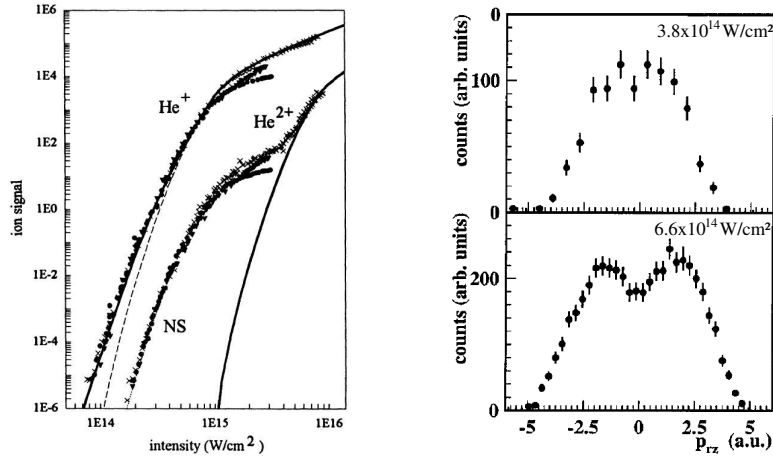


Figure 1.1: The left figure shows the ionization yield of Helium after interaction with a laser pulse (taken from Ref. [10]). The distribution of the momentum of He^{2+} ions (from Ref. [11]) is depicted on the right.

The momentum distribution of the He^{2+} ions shows distinct maxima at non-zero momenta [11] (right hand side of Fig. 1.1). Due to momentum conservation this is a clear indication that the rescattering of an electron with its parent ion collisionally frees (or excites) the second electron. The contribution of different double ionization processes to characteristic ion momentum distributions in noble gas atoms has been studied [12]. For few-cycle laser pulses an asymmetry depending on the carrier-envelope phase was measured [13].

In addition to ionization, it is also observed that atoms subjected to laser pulses emit coherent radiation (for reviews see Refs. [5,14]). The frequency consists of odd multiples of the laser frequency. The efficiency of high-order harmonic generation (HOHG) is constant over many harmonic orders. This leads to a plateau in the frequency spectrum up to a cutoff-energy [15].

Describing the phenomena of laser-atom interactions theoretically, a wide range of approaches has been used. Due to the high intensities of the laser fields perturbative methods are not applicable.

In the nonrelativistic regime, the natural starting point is the time-dependent Schrödinger equation (TDSE). However, analytical solutions for the interaction with an intense laser field do not exist. Numerical implementations face the problem that the computational time scales exponentially with the number of electrons N , the well-known “exponential wall” [16]. Solution of the Schrödinger equation in full dimensionality is therefore limited to two active electrons (see Ref. [17] for double ionization of Helium). Due to this fundamental limitation the prospects to expand its application to systems with more electrons do not seem promising.

A semi-analytical approach is the strong field approximation [18–20] with the inclusion of rescattering. This theory has been successful in addressing both the probability as well as the mechanism of non-sequential ionization (see, e.g., Refs.

[21, 22] and references therein). Apart from inherent challenges such as the choice of the gauge, the strong-field approximation becomes analytically unduly involved with more than two electrons in the continuum.

While purely classical methods [23, 24] have also succeeded in analyzing non-sequential ionization, the limited nature of these models is evident as all quantum-mechanical effects have to be included “by hand”.

Methods based on first principles are R-Matrix Floquet theory [25] and multi-configurational time-dependent Hartree-Fock [26]. Neither the first [27] nor the latter [28, 29] have, however, reproduced the NSDI “knee structure” to date. In addition, they are of limited appeal for the description of large systems. R-Matrix Floquet theory becomes as computationally demanding as the time-dependent Schrödinger equation with multiple free electrons. Multi-configurational time-dependent Hartree-Fock suffers from the non-local exchange potential which requires the calculation of large numbers of overlap integrals each time-step.

Time-dependent density functional theory (TDDFT) [30] in contrast offers the possibility to treat the strong-field dynamics of atomic (and molecular) systems from first principles in a numerically tractable way. It assures that in principle all observables can be calculated exactly from the solution of N one-electron time-dependent Kohn-Sham equations (TDKSE) with effective potentials. This means that in sharp contrast to the time-dependent Schrödinger equation, computational time increases almost linearly with N , offering the possibility to investigate also very complex systems.

Excitation energies and response properties in quantum chemistry (see overviews in Refs. [31–33]) have been calculated successfully using time-dependent density functional theory. In the domain of laser-atom interactions, high-order harmonic spectra were studied using TDDFT [34, 35].

An attempt to calculate photoionization energy spectra from time-dependent density functional theory was not successful though [36]. Previous investigations failed to reproduce the characteristic “knee structure” of the double ionization probability [37–40]. Indeed, this is seen as one of the most dramatic failures of time-dependent density functional theory [41].

In this work we investigate this failure and discuss possible solutions. In Chapter 2 we review the fundamental considerations which allow us to describe an atom in a laser field using time-dependent density functional theory. A model Helium atom and its theoretical description are introduced (Chapter 3). As a reference, the time-dependent Schrödinger equation is solved for this atom and compared to approaches using time-dependent density functional theory. The problem of double ionization probabilities is addressed in Chapter 4, where we introduce two functionals which reproduce a “knee structure” in the double ionization probability. In the following Chapter 5 we analyze the momentum distributions after the ionization process and propose a route towards obtaining ion momentum distributions in time-dependent density functional theory. We report the discovery of non-sequential double recombination in high-order harmonic spectra (Chapter 6)

and discuss challenges in treating it in density-functional theory. Details of the numerical implementation can be found in Appendix A.

Atomic units are used throughout this work, i.e., we set $\hbar = m_e = |e| = 4\pi\epsilon_0 = 1$ (cf. Ref. [42] for an introduction) unless otherwise noted.

Chapter 2

Time-Dependent Density Functional Theory

We present the foundations of time-dependent density functional theory which are necessary to describe the system of interest in this work, an atom in a strong laser field. The Runge-Gross theorem is proven, which establishes a one-to-one mapping between the density and the potential of a system of electrons, thereby assuring that all observables can be expressed as functionals of the density (Sec. 2.1). For a numerical implementation the non-interacting time-dependent Kohn-Sham equations are essential which in principle yield the exact density of the respective system (Sec. 2.2).

An introduction to groundstate density functional theory and other important concepts in time-dependent density functional theory which are not of direct relevance to this work are found elsewhere (for excellent overviews see Refs. [31–33] and references therein). Among the latter are time-dependent spin density functional theory, linear response theory, the calculation of excitation energies as well as the adiabatic local density and time-dependent optimized effective potential approximations of the exchange-correlation potential.

2.1 The Runge-Gross Theorem

We investigate a system of N electrons in time-dependent external single-electron potentials $V(\mathbf{r}, t)$ which are spin-independent. The electrons are assumed to be non-relativistic and to interact through the Coulomb repulsion $W(|\mathbf{r} - \mathbf{r}'|)$. Suppressing spin-indices, the wavefunction of the system is then $\psi(\mathbf{r}_1, \dots, \mathbf{r}_2, t)$. An initial state at t_0 is assumed to be given by $\psi_0 = \psi(\mathbf{r}_1, \dots, \mathbf{r}_2, t_0)$. In this Chapter quantities taken at $t = t_0$ are subscripted by zero.

Let $V(\mathbf{r}, t) \neq V'(\mathbf{r}, t) + C(t)$ be two external potentials which can be expanded into a Taylor series around t_0 and which differ by more than a purely

time-dependent function. Then there exists an integer k for which

$$\partial_t^k [V(\mathbf{r}, t) - V'(\mathbf{r}, t)]|_{t=t_0} \neq \text{const}. \quad (2.1)$$

We first consider the current

$$\mathbf{j}(\mathbf{r}, t) = \langle \psi(\mathbf{r}_1, \dots, \mathbf{r}_2, t) | \hat{\mathbf{j}}(\mathbf{r}) | \psi(\mathbf{r}_1, \dots, \mathbf{r}_2, t) \rangle \quad (2.2)$$

with the usual current density operator given by $\hat{\mathbf{j}}(\mathbf{r}) = \frac{1}{2i} \sum_{i=1}^N [\nabla_i \delta(\mathbf{r} - \mathbf{r}_i) + \delta(\mathbf{r} - \mathbf{r}_i) \nabla_i]$. The current density operator does not depend explicitly on the time. Hence, the equation of motion for the difference of the current densities produced by the two potentials is

$$\begin{aligned} \partial_t [\mathbf{j}(\mathbf{r}, t) - \mathbf{j}'(\mathbf{r}, t)]|_{t=t_0} &= i \langle \psi_0 | [H_0(\mathbf{r}) - H'_0(\mathbf{r}), \hat{\mathbf{j}}(\mathbf{r})] | \psi_0 \rangle \\ &= n_0(\mathbf{r}) \nabla [V_0(\mathbf{r}) - V'_0(\mathbf{r})]. \end{aligned} \quad (2.3)$$

This result is a consequence of the Hamiltonians H_0 and H'_0 of the two systems being identical except for the external potentials V and V' . Making use of the equation of motion k -times yields

$$\partial_t^{k+1} [\mathbf{j}(\mathbf{r}, t) - \mathbf{j}'(\mathbf{r}, t)]|_{t=t_0} = n_0(\mathbf{r}) \nabla \partial_t^k [V(\mathbf{r}, t) - V'(\mathbf{r}, t)]|_{t=t_0} \neq 0, \quad (2.4)$$

where we have assumed that the spatial derivatives of the potentials exist which are necessary to evaluate the commutators. The last result follows from Eq. (2.1) if the initial density $n_0(x)$ does not vanish in exactly those regions where the left hand expression in Eq. (2.1) is not constant. This means that the density currents for the external potentials V and V' will start to be different infinitesimally after t_0 . In order to relate this result to the densities we use the continuity equation for the difference of the densities

$$\partial_t [n(\mathbf{r}, t) - n'(\mathbf{r}, t)]|_{t=t_0} = -\nabla \cdot [\mathbf{j}(\mathbf{r}, t) - \mathbf{j}'(\mathbf{r}, t)]. \quad (2.5)$$

Calculating the $(k+1)$ th time derivate of Eq. (2.5) and making use of Eq. (2.4) we obtain

$$\partial_t^{k+2} [n(\mathbf{r}, t) - n'(\mathbf{r}, t)]|_{t=t_0} = -\nabla \cdot [n_0(\mathbf{r}) \nabla u_k(\mathbf{r})], \quad (2.6)$$

where $u_k(\mathbf{r}) = \partial_t^k [V(\mathbf{r}, t) - V'(\mathbf{r}, t)]|_{t=t_0}$. If we assume that the right hand side vanishes, i.e., that $\nabla \cdot [n_0(\mathbf{r}) \nabla u_k(\mathbf{r})] = 0$ holds, then

$$\begin{aligned} 0 &= \int d^3r u_k(\mathbf{r}) \nabla \cdot [n_0(\mathbf{r}) \nabla u_k(\mathbf{r})] \\ &= \oint d\mathbf{f} \cdot u_k(\mathbf{r}) n_0(\mathbf{r}) \nabla u_k(\mathbf{r}) - \int d^3r n_0(\mathbf{r}) (\nabla u_k(\mathbf{r}))^2. \end{aligned} \quad (2.7)$$

Green's first theorem was used to obtain the surface integral which will vanish for initial densities and u_k falling off fast enough. Then the second integral on the right

has to be zero. As $n_0 \geq 0$, this is a contradiction to Eq. (2.4), where we concluded that $n_0 \nabla u_k \neq 0$. We have thus shown that the right hand side of Eq. (2.6) will not vanish in all relevant cases occurring in atomic physics. The densities of the two potentials will be different infinitesimally later than t_0 , and we can state the Runge-Gross theorem [30]:

An initial state $\psi(\mathbf{r}_1, \dots, \mathbf{r}_2, t_0)$ of an N -electron system in the external single-electron potentials $V(\mathbf{r}, t)$ and $V'(\mathbf{r}, t)$, which differ by more than a purely time-dependent function and are Taylor expandable around $t = t_0$, evolves into densities $n(\mathbf{r}, t)$ and $n'(\mathbf{r}, t)$ which will be different for all times $t > t_0$.

Solution of the time-dependent Schrödinger equations with different external potentials $V(\mathbf{r}, t)$ but a fixed initial state ψ_0 establishes a map $V(\mathbf{r}, t) \rightarrow n(\mathbf{r}, t)$ via the wavefunction ψ . The Runge-Gross theorem then establishes the invertibility of this map $n(\mathbf{r}, t) \rightarrow V(\mathbf{r}, t)$. Hence, a one-to-one mapping exists between the single-electron potential and the density of the system for a given initial state. The density can then be seen as determining the potential (up to a time-dependent function) which in turn determines the wavefunction (up to a time-dependent phase factor).

For our purposes the initial state will be the non-degenerate groundstate of the system. We then know from groundstate density functional theory that the groundstate density determines the groundstate wavefunction, i.e., the initial state $\psi_0[n_0]$ [43]. We can therefore write the time-dependent wavefunction as a functional of the density alone $\psi[n]$. Hence, all observables are determined by the density alone as $O[n] = \langle \psi[n] | \hat{O} | \psi[n] \rangle$, the phasefactor of the wavefunction canceling.

2.2 Time-Dependent Kohn-Sham Equations

We regard a (fictitious) system of N non-interacting electrons which has the same density as the interacting system. The electrons are moving in an effective Kohn-Sham potential v_{KS} which implicitly includes the interactions with the other electrons. This allows us to formulate a time-dependent nonlinear Schrödinger equation for each electron

$$i \partial_t \phi_i(\mathbf{r}, t) = \left(-\frac{1}{2} \Delta + v_{\text{KS}}[n](\mathbf{r}, t) \right) \phi_i(\mathbf{r}, t), \quad (2.8)$$

under the constraint that the Kohn-Sham orbitals $\phi_i(\mathbf{r}, t)$ reproduce the exact density of the physical system

$$n(\mathbf{r}, t) = \sum_{i=1}^N |\phi_i(\mathbf{r}, t)|^2. \quad (2.9)$$

The proof of the Runge-Gross theorem in Sec. 2.1 can now be repeated for this system, the wavefunction being given by the Slater determinant of the orbitals.

This establishes a one-to-one mapping between the density and the Kohn-Sham potential $n(\mathbf{r}, t) \leftrightarrow v_{\text{KS}}[n](\mathbf{r}, t)$. Thus the Runge-Gross theorem states that if v_{KS} exists, it is uniquely determined by the density n which in turn is by construction equal to the true density of the system. We have again assumed the system to be initially in its groundstate and appealed to groundstate density functional theory. Therefore we write the Kohn-Sham potential as a functional of the density.

It can be shown that if the Hamiltonian of the interacting system is stationary for $t < t_0$ an initial non-interacting state with the exact density and the exact time-derivative of the density can be constructed. This in turn assures the existence of the time-dependent Kohn-Sham potential v_{KS} [44]. For the model Helium atom studied in this work, the existence of v_{KS} can be shown explicitly by inversion of the Kohn-Sham equation [45].

From the construction it is clear that one has to be careful to identify the electrons in the physical system (as described by the time-dependent Schrödinger equation) with the fictitious, non-interacting “electrons” of the Kohn-Sham equations. As illustrated by the results in Chapters 4 and 5 the Slater determinant of the Kohn-Sham orbitals does not represent the correlated wavefunction ψ if electron-electron interactions are strong.

For actual calculations we define an exchange-correlation potential by writing

$$v_{\text{xc}}[n](\mathbf{r}, t) = v_{\text{KS}}[n](\mathbf{r}, t) - V(\mathbf{r}, t) - v_{\text{h}}[n](\mathbf{r}, t), \quad (2.10)$$

with the external single-electron potential V from the physical system and the Hartree potential

$$v_{\text{h}}[n](\mathbf{r}, t) = \int d^3r' n(\mathbf{r}', t) W(|\mathbf{r} - \mathbf{r}'|), \quad (2.11)$$

where $W(|\mathbf{r} - \mathbf{r}'|)$ is the electron-electron interaction potential. Equations (2.8)-(2.11) show the great computational advantage of the Kohn-Sham scheme as it requires only the solution of N single-electron equations (in contrast to the time-dependent Schrödinger equation) the potentials of which are local, i.e., multiplicative (in contrast to the time-dependent Hartree-Fock equations).

Being able to derive the Kohn-Sham equations from a stationary action principle $\delta A/\delta n = 0$ would give additional justification to the time-dependent Kohn-Sham scheme. The standard quantum mechanical action has a stationary point at the solution of the time-dependent Schrödinger equation for a given initial wavefunction ψ_0 . A straightforward choice is to extend this action as [30] $\mathcal{A}[n, \psi_0] = \int_{t_0}^{t_1} dt \langle \psi[n, \psi_0](t) | i\partial_t - \hat{H}(t) | \psi[n, \psi_0](t) \rangle$. The wavefunction ψ is written as a functional of the density and the initial state due to the Runge-Gross theorem (cf. Sec. 2.1). However, this definition leads to several paradoxes [31, 41, 44, 46, 47]. It is nevertheless possible to define a functional, the Keldysh action \mathcal{A}^{K} , from which the Kohn-Sham equations can be derived and which leads to the relation $v_{\text{xc}}(\mathbf{r}, t) = \delta \mathcal{A}_{\text{xc}}^{\text{K}} / \delta n(\mathbf{r}, \tau)|_{n=n(\mathbf{r}, t)}$, with τ a pseudotime parameterizing the real time t [44, 46]. In contrast to groundstate density functional theory though this relation does not offer a straightforward way to find approximations of v_{xc} .

We thus know that the time-dependent Kohn-Sham scheme can in principle reproduce the exact density. From Sec. 2.1 we also know that all observables can in principle be expressed as functionals of the density of the system alone. The practical challenge is therefore twofold. One has to approximate v_{xc} in order to gain densities as close as possible to the physical density. In addition, if an expression for the observable as a functional of the density is not known, one has to approximate the functional as well.

Chapter 3

Model System

Our goal is to improve the description of atomic ionization processes using time-dependent density functional theory. Therefore, we investigate the ionization process of Helium exposed to a linearly polarized laser field in order to be able to compare time-dependent density functional calculations to the exact solution of the time-dependent Schrödinger equation. We introduce the different laser pulses used in this work (Sec. 3.1). The linear polarization and the dipole approximation allow us to make use of a one-dimensional model Helium atom (Sec. 3.2). The time-evolution of the system can then be described by the time-dependent Schrödinger equation (Sec. 3.3) or by time-dependent density functional theory (Sec. 3.4). From the Schrödinger equation one can construct an exact Kohn-Sham orbital (EKSO) as a reference for Kohn-Sham orbitals (Sec. 3.5). To describe sequential ionization the corresponding He^+ model (Sec. 3.6) and the single active electron approach (Sec. 3.7) are introduced.

The implementation of the equations presented in this Chapter on a numerical grid is described in detail in Appendix A.

3.1 Laser Pulses

In order to keep computational times manageable when solving the time-dependent Schrödinger equation for the model Helium atom (cf. Appendix A) we use linearly polarized few-cycle laser pulses with N cycles and a \sin^2 -pulse envelope. The length of a pulse with frequency ω is then $T = 2N\pi/\omega$ and the vector potential

$$\mathbf{A}(t) = \hat{A} \mathbf{e}_x \sin^2\left(\frac{\omega}{2N} t\right) \sin(\omega t) \quad (3.1)$$

for $0 \leq t \leq T$ and zero otherwise. We use the dipole approximation, i.e., the spatial dependence of the laser field is neglected. This is reasonable as the wavelengths λ of the laser pulses we study are large compared to the (classical) excursion length of the electrons. Since $\mathbf{A}(\mathbf{r}, t) = \mathbf{A}(t)$ and thus $\mathbf{B}(\mathbf{r}, t) = \nabla \times \mathbf{A}(t) = 0$, magnetic effects are neglected in the dipole approximation. This assumption will only be

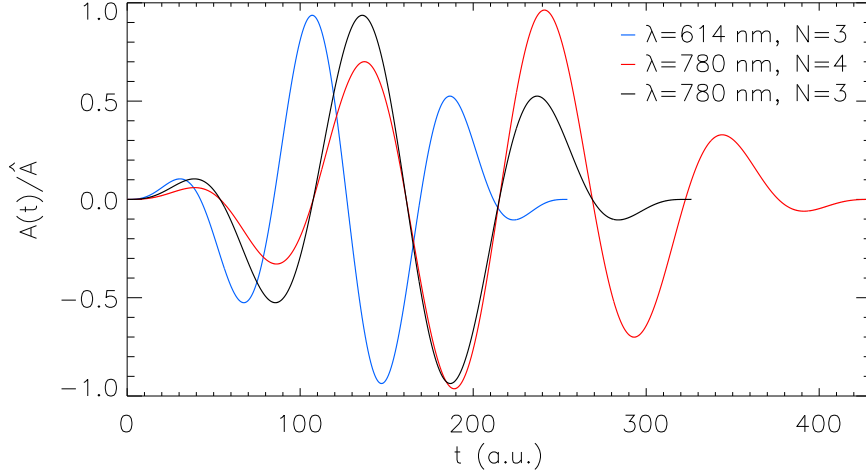


Figure 3.1: Vector potential as a function of time for three of the laser pulses used in this work.

valid as long as $v/c \ll 1$, which is however fulfilled for the intensities used in this work. Classically, the Lorentz force is then $\mathbf{F}_L(\mathbf{r}, t) = -\mathbf{E}(\mathbf{r}, t)$. This shows that for electrons with vanishing initial lateral momentum the motion is restricted to the polarization direction of the laser field as $\mathbf{E}(\mathbf{r}, t) = \mathbf{E}(t) = -\partial_t \mathbf{A}(t)$.

We make use of five different laser pulses which are characterized in Tab. 3.1. Three pulses with $\lambda = 614$ nm and $\lambda = 780$ nm are also depicted in Fig. 3.1 as a function of time. As the effects we investigate depend strongly on the intensity $I = I(\hat{A})$, we perform calculations for different values of \hat{A} for each of the laser pulses. From Fig. 3.1 we see that for few-cycle laser pulses the effective peak amplitude \hat{A}_{eff} may not be equal to \hat{A} . In this work we will always use \hat{A}_{eff} to determine intensities.

Table 3.1: Parameters of the five different laser pulses, the Chapters were results obtained with the respective laser pulse are presented and the corresponding laser system.

λ (nm)	ω (a.u.)	N	Chapter	Laser
248 nm	0.18373	3	4	KrF
614 nm	0.07421	3	4	Dye
780 nm	0.05842	3	4, 5	Ti:Sa
780 nm	0.05842	4	4	Ti:Sa
780 nm	0.05842	6	6	Ti:Sa

3.2 Model Helium Atom

As explained in the previous Sec. 3.1 we use the dipole approximation for the linearly polarized laser pulses interacting with the Helium atom. The dynamics after ionization are dominated by the laser pulse and thus oriented along the laser polarization direction. Therefore it is reasonable to describe the interaction with the laser pulses by a one-dimensional model Helium atom with the spatial dimension along the polarization direction. The electron-electron and electron-nucleus Coulomb interactions $V \propto 1/\sqrt{x^2}$ will thus lead to singularities in the Hamiltonian for $x \rightarrow 0$. This means the electrons cannot pass by each other or by the nucleus. To avert this unphysical behavior we use soft-core potentials $V \propto 1/\sqrt{x^2 + \epsilon}$ for the Coulomb interactions. It is known that all essential features of the ionization process are described well by this model [37, 38, 45, 48–50].

The electrons occupy a spin-singlet state in the groundstate of Helium and the laser pulse in dipole approximation leads to $\mathbf{B}(t) = 0$, so that the electrons will stay in this state for all times $0 \leq t \leq T$. Thus, it is sufficient to study the spatial wavefunction which has to be symmetric under exchange of the electrons.

3.3 Time-Dependent Schrödinger Equation

For the model Helium atom the Hamiltonian in velocity gauge of the one-dimensional time-dependent Schrödinger equation $\partial_t \psi(x_1, x_2, t) = \hat{H}(x_1, x_2, t) \psi(x_1, x_2, t)$ thus is

$$\hat{H} = \sum_{i=1,2} \left(\frac{1}{2} \left[-i \partial_{x_i} + A(t) \right]^2 + V(x) \right) + W(|x_1 - x_2|), \quad (3.2)$$

with $\hat{H} = \hat{H}(x_1, x_2, t)$. The electron-nucleus interaction potential

$$V(x) = -\frac{2}{\sqrt{x^2 + \epsilon_{en}}} \quad (3.3)$$

and the electron-electron interaction potential

$$W(x) = \frac{1}{\sqrt{x^2 + \epsilon_{ee}}} \quad (3.4)$$

are used. A gauge-transformation with $\Lambda(t) = \int^t dt' [A(t')]^2 / 2$ introduces a scalar potential which cancels the A^2 term and adds a purely time-dependent phase-factor to the wavefunction $\psi(x_1, x_2, t) \rightarrow e^{i\Lambda(t)} \psi(x_1, x_2, t)$. The resulting Hamiltonian used in actual calculations thus is

$$\hat{H}(x_1, x_2, t) = \sum_{i=1,2} \left(-\frac{1}{2} \partial_{x_i}^2 + V(x_i, t) \right) + W(|x_1 - x_2|), \quad (3.5)$$

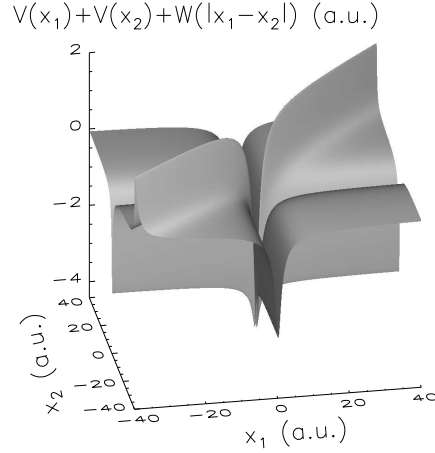


Figure 3.2: Sum of the Coulomb potentials of the electron-nucleus and electron-electron interactions in the two-electron space.

with the external potential

$$V(x, t) = -i A(t) \partial_x + V(x). \quad (3.6)$$

The soft-core parameters of the electron-nucleus (ϵ_{en}) and electron-electron (ϵ_{ee}) interactions are chosen to yield the correct ionization potentials. Reproducing the ionization potential of He^+ , $I_{\text{p}}^{(2)} = 2.0$ fixes $\epsilon_{\text{en}} = 0.5$ (cf. Sec. 3.6). The groundstate energy of the model Helium atom is obtained using imaginary time-propagation (Sec. A.7). The choice $\epsilon_{\text{ee}} = 0.329$ yields the ionization potential of Helium $I_{\text{p}}^{(1)} = -E_0 = -0.904$. In this way we assure consistency with the full-dimensional Helium atom. All results presented in this work are qualitatively insensitive to the exact values of the soft-core parameters.

Figure 3.2 shows the unperturbed potential of the model atom which consists of the sum of the attractive electron-nucleus interactions $V(x_i)$ and the repulsive electron-electron interaction $W(|x_1 - x_2|)$.

3.4 TDDFT Approach

The two electrons constitute a spin-singlet state for all times (cf. discussion in Sec. 3.2). They can thus be described by the same Kohn-Sham orbital. Therefore we have only one Kohn-Sham equation $i \partial_t \phi(x, t) = \hat{H}^{\text{KS}}(x, t) \phi(x, t)$ (cf. Eq. 2.8) with the Hamiltonian

$$\hat{H}^{\text{KS}}(x, t) = -\frac{1}{2} \partial_x^2 + V(x, t) + v_{\text{hx}}(x, t) + v_{\text{c}}(x, t). \quad (3.7)$$

The external potential V is given by Eq. (3.6). The Hartree-exchange potential $v_{\text{hx}}(x, t) = v_{\text{h}}(x, t) + v_{\text{x}}(x, t)$ follows as

$$v_{\text{hx}}(x, t) = \frac{1}{2} \int dx' \frac{n(x', t)}{\sqrt{(x - x')^2 + \epsilon_{\text{ee}}^{\text{KS}}}}, \quad (3.8)$$

where we have used the exact exchange term for Helium $v_{\text{x}}(x, t) = -v_{\text{h}}(x, t)/2$ which is local as both electrons are described by the same orbital. The unknown correlation potential v_{c} is in principle determined via the Runge-Gross theorem (Sec. 2.1) by the time-dependent density and the groundstate wavefunction. The model Helium atom is in its groundstate at $t_0 = 0$ and from static density functional theory we know that the groundstate wavefunction can then be expressed as a functional of the density [43]. Therefore, v_{c} can be expressed as a functional of the density alone $v_{\text{c}}(x, t) = v_{\text{c}}[n](x, t)$, with the density of the system (2.9) given by

$$n(x, t) = 2 |\phi(x, t)|^2. \quad (3.9)$$

However, the functional dependence is not known and it is therefore necessary to approximate v_{c} .

From Eq. (3.7) we see that in the special case of the Helium atom (due to the locality of v_{x}) the time-dependent Hartree-Fock (TDHF) treatment of the problem yields an identical description as a time-dependent density functional approach with the correlation potential set to zero. In this work we will therefore refer to the approximation $v_{\text{c}} = 0$ as ‘‘TDHF’’.

Studying ionization processes using the exact time-dependent Schrödinger solution of a one-dimensional model Helium atom it was found that the correlation potential changes discontinuously when the number of bound electrons

$$N(t) = \int_{-a}^{+a} dx n(x, t), \quad (3.10)$$

passes an integer [45]. This feature is well-known from groundstate density functional theory using fractional occupation numbers [51] and in the time-dependent case carries over to v_{xc} in more complex atoms [52]. The parameter $a = 6$ a.u. is chosen to encompass the bound states (cf. Sec. 4.1). A model potential taking this behavior into account is the LK05 potential [45]

$$v_{\text{c}}^{\text{LK05}}(x, t) = \left[\frac{N_0/N(t)}{1 + \exp[C(N_0/N(t) - 2)]} - 1 \right] v_{\text{hx}}(x, t). \quad (3.11)$$

C is an arbitrary but large constant (we choose $C = 50$). We have $N_0 = N(t_0) = 2$ in the model Helium atom, as $t_0 = 0$ is the time when the system is in its groundstate before interaction with the laser pulse. With decreasing $N(t)$ the correlation potential compensates the decreasing value of $v_{\text{hx}}(x, t)$ so that the ionization potential is held (approximately) constant. When the first electron is removed ($N(t) < 1$) from the atom $v_{\text{hxc}}^{\text{LK05}}(x, t) \rightarrow 0$, i.e., a hydrogen-like ion is left.

The same behavior is modeled by the BW05 potential

$$v_c^{\text{BW05}}(x, t) = v_{\text{hx}}(x, t_0) \Theta(N(t) - 1) - v_{\text{hx}}(x, t). \quad (3.12)$$

The groundstate Hartree-exchange potential describes the electron-electron interaction until the first electron is removed, leaving a one-electron system with $v_{\text{hxc}}^{\text{BW05}}(x, t) = 0$.

From Eqs. (3.11) and (3.12) we have $v_c(x, t_0) = 0$, i.e., the groundstate is identical for the TDHF, LK05 and BW05 approximations of v_c . Via the ionization potential of He^+ , $\epsilon_{\text{en}} = 0.5$ is already fixed (cf. Sec. 3.6). As described for the time-dependent Schrödinger equation in Sec. 3.3, we choose $\epsilon_{\text{en}}^{\text{KS}} = 0.343$ to acquire $I_{\text{p}}^{(1)} = 0.904$ for the model Helium atom.

3.5 The exact Kohn-Sham orbital

Along the lines of Ref. [45] we will construct from the solution of the time-dependent Schrödinger equation an exact Kohn-Sham orbital (EKSO). The Schrödinger solution gives the exact density of our model Helium atom

$$n(x, t) = 2 \int dx_2 |\psi(x, x_2, t)|^2 = 2 \int dx_1 |\psi(x_1, x, t)|^2. \quad (3.13)$$

A time-dependent density functional calculation with the exact correlation potential v_c would, via the time-dependent Kohn-Sham scheme, give the same density

$$n(x, t) = 2 |\phi(x, t)|^2. \quad (3.14)$$

Similarly, the Schrödinger solution yields the exact probability current of the system $j(x, t) = -i (\partial_x - \partial_{x'}) \gamma(x, x', t)|_{x=x'}/2$ with the one-electron reduced density matrix $\gamma(x, x', t) = 2 \int dx_2 \psi^*(x', x_2, t) \psi(x, x_2, t)$ as

$$\begin{aligned} j(x, t) &= 2 \text{Im} \int dx_2 \psi^*(x, x_2, t) \partial_x \psi(x, x_2, t) \\ &= 2 \text{Im} \int dx_1 \psi^*(x_1, x, t) \partial_x \psi(x_1, x, t). \end{aligned} \quad (3.15)$$

The second expression follows from the symmetry of $\psi(x_1, x_2, t)$ in the electron coordinates by integrating out x_1 in the expression for $\gamma(x, x', t)$. The current of the Kohn-Sham system is

$$j(x, t) = 2 \text{Im} \phi^*(x, t) \partial_x \phi(x, t). \quad (3.16)$$

For a one-dimensional system the exact current and the Kohn-Sham current are equal, since from the continuity equation $-\partial_x j(x, t) = \partial_t n(x, t)$ we have $j(x, t) = -\int_{-\infty}^x dx' \partial_t n(x', t)$ which determines the current uniquely if the current vanishes at infinity [41]. As we know that the densities of the exact and the Kohn-Sham systems are equal the currents have to be equal too.

The Kohn-Sham orbital $\phi(x, t) = |\phi(x, t)| e^{i\vartheta(x, t)}$ can now be determined. Equating Eqs. (3.13) and (3.14) as well as Eqs. (3.15) and (3.16), we have for each point in space and time two equations for the absolute value and the phase of the orbital

$$\begin{aligned} |\phi(x, t)| &= \sqrt{n(x, t)/2}, \\ \vartheta(x, t) &= \int_{-\infty}^x dx' \frac{j(x', t)}{n(x', t)} + \alpha(t). \end{aligned} \quad (3.17)$$

The unknown purely time-dependent phase factor $\alpha(t)$ does not affect the results presented in this work and is therefore set to zero.

With Eqs. (3.17) we can thus construct the Kohn-Sham orbital which a time-dependent Kohn-Sham equation with the exact v_c would yield from the solution of the time-dependent Schrödinger equation. This exact Kohn-Sham orbital allows to separate the tasks of finding a suitable approximation of v_c (where it serves as a reference for the resulting orbital) and appropriate functionals for observables (where it is the exact input).

3.6 Model He⁺ Ion

In Sec. 3.3 we discussed the time-dependent Schrödinger equation of the model Helium atom. The Hamiltonian in velocity gauge of the time-dependent Schrödinger equation of the corresponding model He⁺ ion $i\partial_t \psi^{\text{He}^+}(x, t) = \hat{H}^{\text{He}^+}(x, t) \psi^{\text{He}^+}(x, t)$ is deduced as

$$\hat{H}^{\text{He}^+}(x, t) = -\frac{1}{2} \partial_x^2 + V(x, t), \quad (3.18)$$

with the external potential $V(x, t)$ (3.6). The A^2 term has been transformed away (cf. Sec. 3.3).

Using imaginary time-propagation to determine the groundstate of He⁺ (Sec. A.7), we choose the soft-core parameter of the electron-nucleus interaction $\epsilon_{\text{en}} = 0.5$ to yield the ionization potential $I_p = 2.0$ of He⁺, which is identical to $I_p^{(2)}$ of He. To guarantee consistency in the ionization process, $\epsilon_{\text{en}} = 0.5$ is used in the time-dependent Schrödinger equation for the model Helium atom and in the Kohn-Sham equations (as the Kohn-Sham equation for He⁺ is identical to Eq. 3.18).

3.7 Single-Active Electron Approach

In the single-active electron approach one electron is treated as being bound for all times while the other electron interacts with the laser field. Therefore the two electrons are described by different wavefunctions. Hence, the total wavefunction of the atom is not symmetric under electron exchange if it is written as a product of the single-electron wavefunctions, i.e., the electrons are assumed to be distinguishable.

The time-dependent Schrödinger equation for the active (first) electron then is $i \partial_t \phi_{(1)}^{\text{SAE}}(x, t) = \hat{H}_{(1)}^{\text{SAE}}(x, t) \phi_{(1)}^{\text{SAE}}(x, t)$ with the Hamiltonian

$$\hat{H}_{(1)}^{\text{SAE}}(x, t) = -\frac{1}{2} \partial_x^2 + V(x, t) + v_{\text{hx}}(x, t_0). \quad (3.19)$$

The external potential $V(x, t)$ is given by Eq. (3.6) and the groundstate Hartree-exchange potential $v_{\text{hx}}(x, t_0)$ (3.8) is used. The second electron is described by the wavefunction $\phi_{(2)}^{\text{SAE}}(x, t) = \phi_{(1)}^{\text{SAE}}(x, t_0)$, i.e., it stays in the groundstate for all times.

Chapter 4

Ionization Probabilities

In the first Sec. 4.1 of this chapter we will explain how single and double ionization probabilities are calculated in the model Helium atom. The results of the solution of the time-dependent Schrödinger equation for different laser pulses are presented (Sec. 4.2), reproducing the “knee structure” typical of non-sequential double ionization. We then turn to the calculation of ionization probabilities from time-dependent density functional calculations. The deficiencies of uncorrelated ionization probability functionals are shown (Sec. 4.3.1). We make use of them to evaluate the quality of approximations of the correlation potential in Sec. 4.3.2. Functionals including correlation are constructed (Sec. 4.3.3) and the resulting correlation integral is examined for exact inputs (Sec. 4.3.4). The results underline the importance of the number of bound electrons. General considerations regarding the approximation of the correlation integral are made in Sec. 4.3.5. The Becke approximation from groundstate density functional theory is found to be insufficient to improve the results of the uncorrelated functionals (Sec. 4.3.6). We introduce the adiabatic (Sec. 4.3.7) and the fit function approximations (Sec. 4.3.8), which are able to reproduce the “knee structure” in the double ionization probability.

4.1 Calculation of Ionization Probabilities

Given the groundstate wavefunction of our model Helium atom $\psi_0 = \psi(x_1, x_2, t_0)$ and the wavefunction $\psi(t) = \psi(x_1, x_2, t)$ during or after the interaction with the laser field our goal is to calculate the ionization probability.

The integral over the probability density not bound to the atom is the probability for ionization. With \hat{H}_0 the Hamiltonian of the unperturbed model Helium atom with bound eigenstates ψ_n , $n = 0, 1, \dots$ we define the projection operator $\hat{\mathcal{P}}_0 = \sum_n |\psi_n\rangle\langle\psi_n|$. Thus, projecting out the bound states yields the “part” of the wavefunction ψ associated with ionization $|\psi_i(t)\rangle = |\psi(t)\rangle - \hat{\mathcal{P}}_0 |\psi(t)\rangle$. Hence,

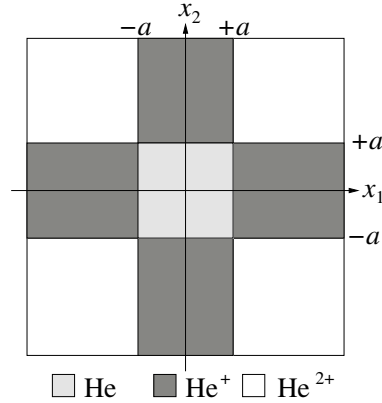


Figure 4.1: Schematic illustration of the areas \mathcal{A} used for calculating ionization probabilities of the model Helium atom. Note that $a = 6$ a.u. and the size of the grid $|x_i| \leq 300 - 1300$ a.u., $i \in \{1, 2\}$ (for details cf. Sec. A.9) are not drawn to scale.

the ionization probability is given as

$$P(t) = \langle \psi_i(t) | \psi_i(t) \rangle. \quad (4.1)$$

This approach however has the disadvantage that one needs to know all bound states of our model atom. Calculating them numerically involves considerable effort (even the groundstate is not known analytically, cf. Sec. A.7). In addition, Eq. (4.1) alone does not yield information about single and double ionization probabilities, only of their sum P .

Therefore, we calculate ionization probabilities by partitioning the two-electron space. We interpret single ionization as the situation when only one electron is farther than a distance a away from the Helium nucleus (situated at the origin). Then, the atom is doubly ionized if both electrons are further than a away from the origin. Accordingly, when both electrons are in the vicinity of the nucleus the atom is not ionized. Since the absolute square of the wavefunction at a point in the Hilbert space gives the probability to find the two electrons at the respective coordinates, we define the areas

$$\begin{aligned} \mathcal{A}(\text{He}) &= \{(x_1, x_2) \mid |x_1| \leq a, |x_2| \leq a\}, \\ \mathcal{A}(\text{He}^+) &= \{(x_1, x_2) \mid |x_i| > a, |x_{j \neq i}| \leq a \forall i, j \in \{1, 2\}\}, \\ \mathcal{A}(\text{He}^{2+}) &= \{(x_1, x_2) \mid |x_1| > a, |x_2| > a\}. \end{aligned} \quad (4.2)$$

Integrating the probability density, i.e., the absolute square of the wavefunction $\psi(x_1, x_2, t)$ over the areas \mathcal{A} (which are indicated in Fig. 4.1) then yields the respective ionization probabilities

$$P^0(t) = \iint_{\mathcal{A}(\text{He})} dx_1 dx_2 |\psi(x_1, x_2, t)|^2,$$

$$\begin{aligned}
P^+(t) &= \iint_{\mathcal{A}(\text{He}^+)} dx_1 dx_2 |\psi(x_1, x_2, t)|^2, \\
P^{2+}(t) &= \iint_{\mathcal{A}(\text{He}^{2+})} dx_1 dx_2 |\psi(x_1, x_2, t)|^2.
\end{aligned} \tag{4.3}$$

In order to encompass all bound states the parameter a is chosen as $a = 6$ a.u. throughout this work, results being insensitive to the exact value of a . This scheme to determine ionization probabilities has been successfully used in numerous similar calculations [37, 38, 49]. The integrations in Eqs. (4.3) are approximated by a Riemann sum. We replace infinite integral limits by the boundaries of the numerical grid, which is chosen large enough to minimize norm loss (cf. Secs. A.8 and A.9).

In the special case of an uncorrelated two-electron atom, i.e., $\hat{H}(x_1, x_2, t) = \hat{h}^{(1)}(x_1, t) + \hat{h}^{(2)}(x_2, t)$ with identical Hamiltonians for the two electrons $\hat{h}^{(1)} = \hat{h}^{(2)}$, the wavefunction can be written as a product of two identical one-electron wavefunctions $\psi(x_1, x_2, t) = \phi(x_1, t) \phi(x_2, t)$. Inserting this into Eqs. (4.3) and using that $\int dx |\phi(x, t)|^2 = 1$ the ionization probabilities simplify to

$$\begin{aligned}
P^0(t) &= [p(t)]^2, \\
P^+(t) &= 2p(t)[1 - p(t)], \\
P^{2+}(t) &= [1 - p(t)]^2, \\
p(t) &= \int_{-a}^{+a} dx |\phi(x, t)|^2.
\end{aligned} \tag{4.4}$$

In this case, the ionization probabilities can be calculated simply from the single-electron wavefunction $\phi(x, t)$ in the vicinity of the Helium nucleus $|x| \leq a$, i.e., from the probabilities for the respective electron to be free ($1 - p$) and to be bound (p).

4.2 Ionization Probabilities from the TDSE

The time-dependent Schrödinger equation is solved for different intensities of four few-cycle laser pulses (cf. Sec. 3.1). Single and double ionization probabilities are calculated from the wavefunction $\psi(x_1, x_2, T)$ after the laser pulse using Eqs. (4.3).

Figure 4.2 shows ionization probabilities for the $N = 3$ -cycle laser pulses with different wavelengths. The single ionization probabilities increase with increasing intensity of the laser field, show a maximum around $I \approx 3 \times 10^{15} \text{ W/cm}^2$ and decrease again for larger intensities for all three laser pulses. The small deviations from the smooth increase for $\lambda = 248 \text{ nm}$ are due to the resonant excitation of bound states in the model atom.

The double ionization probabilities show a “knee structure”, i.e., a change of sign in the curvature for intensities $I \leq 3 \times 10^{15} \text{ W/cm}^2$ due to non-sequential double ionization, as will be discussed below. With decreasing wavelengths, i.e., increasing frequencies the “knee structure” becomes less pronounced. This is due to multiphoton ionization becoming dominant for larger frequencies compared to ionization by tunneling.

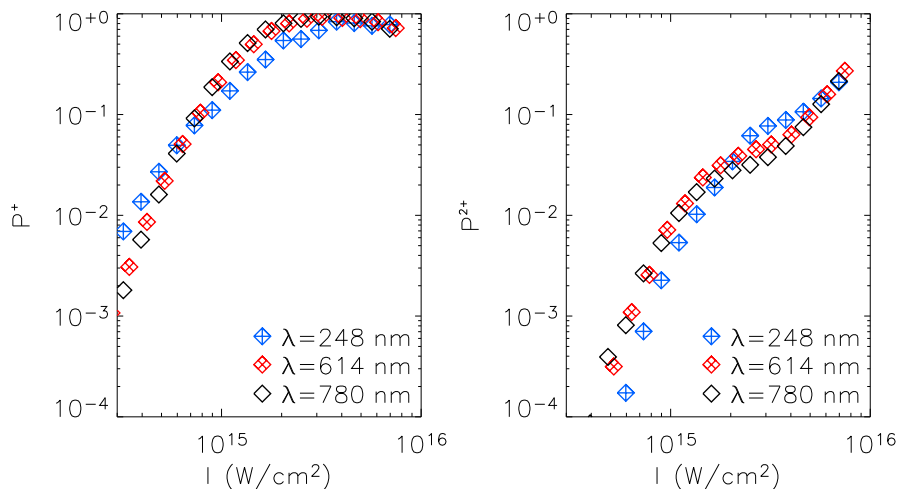


Figure 4.2: Single and double ionization probabilities as a function of the effective peak intensity calculated from the solution of the time-dependent Schrödinger equation. $N = 3$ -cycle laser pulses with different wavelengths λ were used.

Comparison of Fig. 4.2 with experimental ionization yields (e.g., left hand side of Fig. 1.1) shows good qualitative agreement. While we calculate ionization probabilities for a single atom, in experiments the numbers of singly and doubly ionized atoms are measured. Due to an increase of the focal volume of the laser with increasing intensity the number of singly ionized Helium atoms continues to increase in experiments for large intensities.

To further elucidate the double ionization process we compare the results from the time-dependent Schrödinger equation to double ionization probabilities for a (modeled) sequential ionization process where both electrons are dislodged after one another without mutual interaction. The first electron has to be removed from a Helium atom in its groundstate. Therefore we describe the first electron by the solution ϕ_1 of a single-active electron model (cf. Sec. 3.7).

In this sequential model, after ionization of the first electron a He^+ system in its groundstate is left. The one-electron Schrödinger equation yields ϕ_2 (cf. Sec. 3.6). The probability for the k -th electron to be still bound follows then from Eqs. (4.4) as $p_k(t) = \int_{-a}^{+a} dx |\phi_k(x, t)|^2$. The sequential double ionization probability is interpreted as the product of the probabilities that both electrons are free

$$P_{\text{SEQ}}^{2+}(t) = [1 - p_1(t)] [1 - p_2(t)] . \quad (4.5)$$

This sequential double ionization process yields ionization probabilities at the end of the laser pulse which are several orders of magnitude too small for intensities $I < 3 \times 10^{15} \text{ W/cm}^2$ compared to the Schrödinger solution, as evidenced by Fig. 4.3 for the $\lambda = 780 \text{ nm}$, $N = 3$ -cycle pulse. This is a clear indication that the increase by several orders of magnitude in the double ionization probability compared to a

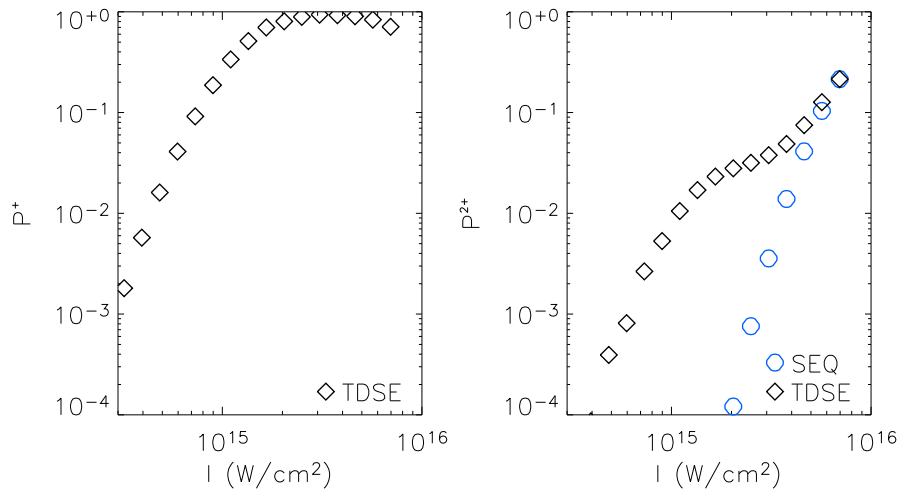


Figure 4.3: Ionization probabilities as a function of the effective peak intensity of the $\lambda = 780$ nm, $N = 3$ -cycle laser pulse. Probabilities calculated from the time-dependent Schrödinger equation (TDSE) are compared to the probabilities for sequential double ionization (SEQ).

sequential scenario is due to a non-sequential processes, caused by electron-electron interactions.

However, the numerical complexity of solving the N -electron time-dependent Schrödinger equation for more complex atoms than Helium makes it desirable to calculate the ionization probabilities from a numerically less demanding approach for N -electron systems. As explained above time-dependent density functional theory offers such a description. The ionization probabilities of the Schrödinger solution will therefore serve as a reference for the calculation of ionization probabilities from time-dependent density functional calculations.

4.3 Ionization Probabilities from TDDFT

As pointed out in Sec. 3.4 a time-dependent density functional calculation for the model Helium atom consists of solving a single time-dependent Kohn-Sham equation which yields an orbital $\phi(x, t)$. Obtaining ionization probabilities from time-dependent density functional theory faces two challenges (cf. Sec. 2.2), (a) reproducing the exact densities from the Schrödinger solution and (b) finding the correct functionals of the density for the calculation of the ionization probabilities.

We will first address (a) in Secs. 4.3.1 and 4.3.2 using a preliminary solution for (b) and compare different approximations of the correlation potential v_c , the only unknown term in the Kohn-Sham Hamiltonian for our model Helium atom. This will be followed by a derivation of correct correlated functionals for the ionization probabilities (Secs. 4.3.3 and 4.3.4) and approximations of these (Secs. 4.3.5 – 4.3.8).

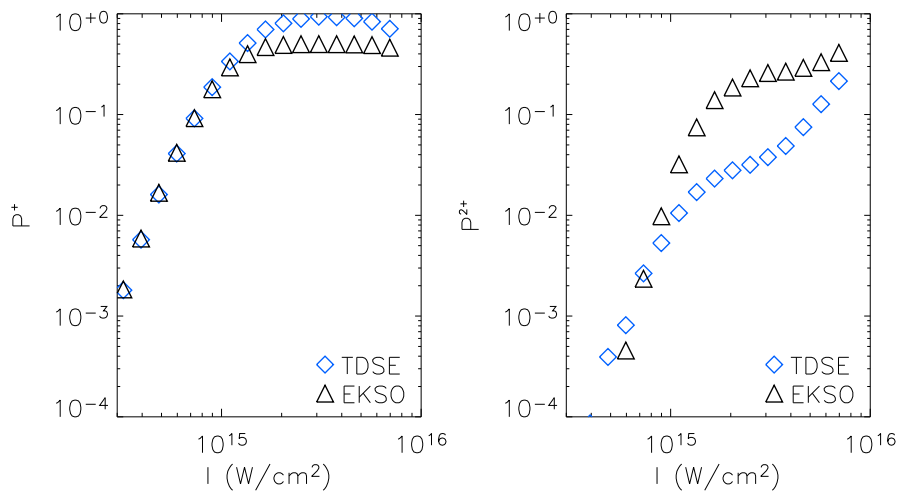


Figure 4.4: Ionization probabilities calculated from the uncorrelated functionals using the exact Kohn-Sham orbital (EKSO) compared to results obtained from the Schrödinger solution (TDSE). Probabilities are shown as a function of the effective peak intensity of the $\lambda=780$ nm, $N=3$ -cycle laser pulse.

4.3.1 Uncorrelated Functionals

A straightforward solution to the problem of finding functionals for the ionization probabilities is to interpret the two identical Kohn-Sham orbitals as orbitals of the real electrons, i.e., writing the wavefunction as a product $\psi(x_1, x_2, t) = \phi(x_1, t)\phi(x_2, t)$. As pointed out above, this immediately yields uncorrelated functionals for the ionization probabilities, namely Eqs. (4.4). This approach has been widely used [37,38,40,45] although it does neglect electron correlations. However, as pointed out in Sec. 4.2 electron-electron interactions are of fundamental importance for non-sequential double ionization. Therefore one cannot expect this approach to be sufficient. This limitation becomes clear immediately when using the exact Kohn-Sham orbital $\phi^{\text{EKSO}}(x)$ constructed from the solution of the Schrödinger equation $\psi(x_1, x_2, t)$ (cf. Sec. 3.5) in Eqs. (4.4). This orbital gives the exact density $n(x) = n^{\text{EKSO}}(x)$.

The probability for single ionization after interaction with the $\lambda = 780$ nm, $N = 3$ -cycle laser pulse is markedly lower in the middle of the intensity regime shown in Fig. 4.4 than for the fully correlated TDSE solution. For low and high intensities probabilities match better. In the case of double ionization, this behavior is reversed: The probability in the regime of the “knee structure” is too high by several orders of magnitude. A “knee structure”, i.e., a change of sign in the curvature as a function of the intensity in the double ionization probabilities is present but does not reproduce the fully correlated result. This confirms that even for orbitals which would be obtained if the exact v_c was known, the functionals Eqs. (4.4) and thus a product wavefunction approach are insufficient to describe

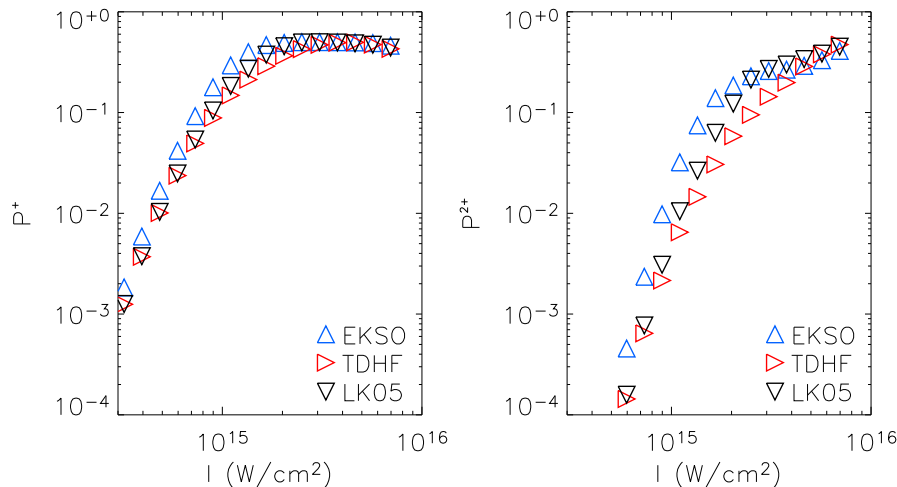


Figure 4.5: Ionization probabilities after interaction with the $\lambda=780$ nm, $N=3$ -cycle laser pulse calculated using the uncorrelated functionals. Probabilities obtained from the orbitals of calculations with $v_c = 0$ (TDHF) and v_c^{LK05} are compared to the results for the exact Kohn-Sham orbital (EKS0).

non-sequential double ionization. Nevertheless the functionals Eqs. (4.4) are a valuable tool for evaluating the quality of approximations of the correlation potential v_c in the Kohn-Sham equation. Since these functionals include only integrals over the absolute square of the orbital, the results for the exact Kohn-Sham orbital serve as a sensitive benchmark for orbitals obtained from calculations with approximate correlation potentials v_c .

4.3.2 Comparison of Correlation Potentials

The uncorrelated ionization probability functionals are evaluated for time-dependent density functional calculations with the TDHF, LK05 and BW05 approximations of v_c (cf. Sec. 3.4). The probabilities are compared to the results for the exact Kohn-Sham orbital (Sec. 4.3.1) which is identical to the orbital, a calculation with the correct correlation potential v_c would yield.

In Fig. 4.5 the improvement of the LK05 approximation as compared to a TDHF approach ($v_c = 0$) is clearly discernible. The ionization probabilities calculated from the uncorrelated functionals (4.4) reproduce the probabilities from the EKS0 solution better than the TDHF probabilities. Since the EKS0 solution gives the orbitals which one would acquire with the exact v_c this is an indication that the densities (since $n(x) = 2|\phi(x)|^2$ in our case) resemble the exact densities better than the choice $v_c = 0$. This is especially evident in the appearance of a “knee structure” in the double ionization probabilities which is absent in the TDHF probabilities. The LK05 potential thus improves at least the integrals of the density over bound and free states as compared to the TDHF approach. However, for low intensities

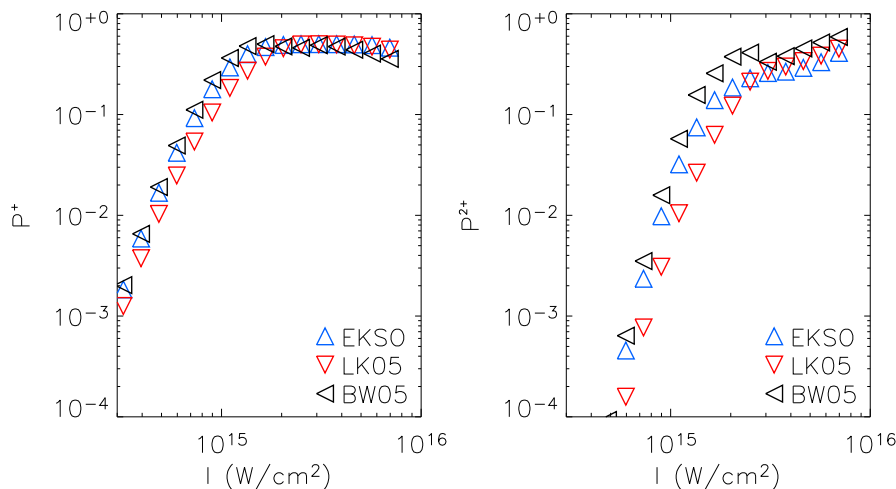


Figure 4.6: Single and double ionization probabilities calculated from the uncorrelated ionization probability functionals. Results for the orbitals obtained with v_c^{BW05} and v_c^{LK05} are compared to the results a calculation with the exact v_c would yield (EKS0). Probabilities are shown as a function of the effective peak intensity of the $\lambda=780$ nm, $N=3$ -cycle laser pulse.

$I \leq 1 \times 10^{15}$ W/cm² the ionization probabilities are systematically too low for both approaches (and indeed are similar since $v_c^{\text{LK05}} \approx 0$ in this intensity regime).

In addition, we found that in v_c^{LK05} the exact form of the prefactor of v_{hxc} , which increases with a decreasing number of bound electrons, has only a negligible influence on the ionization probabilities. The same is true when the Fermi function is replaced by a stepfunction at $N(t) = 1$.

Ionization probabilities of the uncorrelated functionals for the v_c^{BW05} and v_c^{LK05} calculations are compared in Fig. 4.6. Correcting the change in the ionization potential with decreasing number of bound electrons by leaving v_{hxc} constant overcompensates the effect, leading to double ionization probabilities larger than the results for the exact Kohn-Sham orbital. Since probabilities agree well for intensities with $N(T) \leq 1$ the densities acquired from the v_c^{BW05} calculation confirm the importance of the discontinuity in v_c at $N(T) = 1$. However, double ionization probabilities show an (over-)pronounced change in the sign of the curvature. We attribute the last effect to the sudden drop in v_{hxc} for $N(T) \approx 1$. From the integral over bound and free states we thus conclude that v_c^{BW05} is a slightly less accurate approximation than v_c^{LK05} .

In summary, we have thus confirmed that the LK05 and (to a lesser extent) the BW05 approximations for v_c yield (via the orbitals) densities which give results for the uncorrelated ionization probability functionals in good agreement with the results one would acquire for the exact v_c .

4.3.3 Correlated Functionals

In Sec. 4.3.1 it was shown that the uncorrelated functionals of Eq. (4.4) are insufficient to obtain agreement with the ionization probabilities from the solution of the Schrödinger equation. This holds true even if the exact v_c potential in a time-dependent density functional calculation was known, as evidenced by the results acquired with the exact Kohn-Sham orbital.

For a general three-dimensional time-dependent system of N electrons we introduce the diagonal of the reduced two-electron density matrix

$$\rho(\mathbf{r}_1, \mathbf{r}_2, t) = N(N-1) \int d^3r_3 \cdots \int d^3r_N |\psi(\mathbf{r}_1, \mathbf{r}_2, \mathbf{r}_3, \cdots, \mathbf{r}_N, t)|^2 \quad (4.6)$$

and the time-dependent exchange-correlation function [40]

$$g_{xc}(\mathbf{r}_1, \mathbf{r}_2, t) = \frac{\rho(\mathbf{r}_1, \mathbf{r}_2, t)}{n(\mathbf{r}_1, t)n(\mathbf{r}_2, t)}, \quad (4.7)$$

where we have suppressed spin-indices.

For the one-dimensional two-electron model Helium atom, these expressions reduce to

$$\rho(x_1, x_2, t) = 2|\psi(x_1, x_2, t)|^2 \quad (4.8)$$

and

$$g_{xc}[n](x_1, x_2, t) = \frac{\rho(x_1, x_2, t)}{n(x_1, t)n(x_2, t)}, \quad (4.9)$$

where $\psi(x_1, x_2, t)$ is the solution of the time-dependent Schrödinger equation. The density $n(x, t) dx$ gives the probability to find one of the electrons at time t at x in dx . The joint probability to find an electron at time t at x_1 in dx_1 and an electron at x_2 in dx_2 is $\rho(x_1, x_2, t) dx_1 dx_2$. We will therefore refer to ρ as the pair density of the system. Hence, $n(x_2, t) g_{xc}(x_1, x_2, t) dx_2$ gives the conditional probability to find at time t an electron at x_2 in dx_2 , if there is an electron at x_1 . This interpretation of the correlation function as a probability, which is an observable, assures by virtue of the Runge-Gross theorem (Sec. 2.1) that the correlation function can in principle be expressed exactly as a functional of the density [40] as indicated in Eq. (4.9). For notational ease we will not explicitly write out the functional dependence on the density in the following sections though.

The density of our model atom is related to the pair density by

$$n(x, t) = \int dx_2 \rho(x, x_2, t) = \int dx_1 \rho(x_1, x, t) \quad (4.10)$$

but can in principle also be obtained exactly from the orbital ϕ of a time-dependent density functional calculation (cf. Sec. 3.4) with the exact v_c :

$$n(x, t) = 2|\phi(x, t)|^2. \quad (4.11)$$

With $P^0 + P^+ + P^{2+} = 1$, Eqs. (4.10) and (4.9) can be used to express the ionization probabilities given by Eqs. (4.3) for $\psi(x_1, x_2, t)$ in terms of the density and the exchange-correlation function [40]. Then the correlated ionization probability functionals are

$$\begin{aligned}
P^0(t) &= \frac{1}{2} \int_{-a}^{+a} dx_1 \int_{-a}^{+a} dx_2 g_{xc}(x_1, x_2, t) n(x_1, t) n(x_2, t), \\
P^+(t) &= \int_{-a}^{+a} dx n(x, t) \\
&\quad - \int_{-a}^{+a} dx_1 \int_{-a}^{+a} dx_2 g_{xc}(x_1, x_2, t) n(x_1, t) n(x_2, t), \\
P^{2+}(t) &= 1 - \int_{-a}^{+a} dx n(x, t) \\
&\quad + \frac{1}{2} \int_{-a}^{+a} dx_1 \int_{-a}^{+a} dx_2 g_{xc}(x_1, x_2, t) n(x_1, t) n(x_2, t). \quad (4.12)
\end{aligned}$$

We write Eq. (4.9) as a sum of the exchange function g_x and the correlation function g_c . For a system with a two-electron wavefunction that can be expressed exactly as a product wavefunction one has

$$g_{xc}(x_1, x_2, t) = g_x(x_1, x_2, t) = \frac{1}{2}. \quad (4.13)$$

This assumption is made in time-dependent Hartree-Fock calculations (which for the model Helium atom correspond to density functional calculations with $v_c = 0$, cf. Sec. 3.4) and leads to the uncorrelated ionization probability functionals of Eqs. (4.4). These functionals follow directly from Eqs. (4.12) by setting $g_{xc} = g_x = \frac{1}{2}$. With Eq. (4.13) the correlation function g_c is given by

$$g_c(x_1, x_2, t) = \frac{\rho(x_1, x_2, t)}{n(x_1, t) n(x_2, t)} - \frac{1}{2}. \quad (4.14)$$

For use in the following sections we note that due to Eq. (4.10) the correlation function fulfills the integration constraints

$$\int dx_1 n(x_1, t) g_c(x_1, x_2, t) = \int dx_2 n(x_2, t) g_c(x_1, x_2, t) = 0. \quad (4.15)$$

We define the correlation integral

$$I_c(t) = \int_{-a}^{+a} dx_1 \int_{-a}^{+a} dx_2 n(x_1, t) n(x_2, t) g_c(x_1, x_2, t), \quad (4.16)$$

which is a functional of the density since $g_c[n] = g_{xc}[n] - 1/2$ is a functional of the density. The correlated ionization probability functionals (4.12) can then be

written as the sum of the uncorrelated functionals (4.4) and a correction term (4.16) solely depending on the correlation integral:

$$\begin{aligned}
 P^0(t) &= [p(t)]^2 + \frac{1}{2} I_c(t), \\
 P^+(t) &= 2p(t)[1 - p(t)] - I_c(t), \\
 P^{2+}(t) &= [1 - p(t)]^2 + \frac{1}{2} I_c(t), \\
 p(t) &= \int_{-a}^{+a} dx |\phi(x, t)|^2 = \frac{1}{2} \int_{-a}^{+a} dx n(x, t). \quad (4.17)
 \end{aligned}$$

It is important to note that with Eqs. (4.17) the information required to calculate the exact ionization probabilities is reduced to the knowledge of (a) the exact density in the range $-a \leq x \leq +a$ and (b) the exact correlation function g_c in $\mathcal{A}(\text{He})$ (4.2). Thus, only information about the system close to the Helium nucleus is needed. This result is remarkable and counterintuitive, at least at first sight. An explanation is provided by the observation that the density of the system (4.10) in the range $-a \leq x \leq +a$, through the integration over one electron coordinate, implicitly includes information about the probability for single ionization as calculated from the absolute square of the (correlated) wavefunction ψ in Eqs. (4.3).

The exact functional dependence of g_c on n is not known and the calculation of the pair density $\rho(x_1, x_2, t)$ at time $t = T$ is computationally demanding even for the one-dimensional model Helium atom. Therefore, it is necessary to find a suitable approximation for g_c (or actually I_c) after the laser pulse in $\mathcal{A}(\text{He})$ in order to express the ionization probabilities in terms of quantities that can be calculated easily numerically and therefore allow the approach to be carried over to more complex systems than Helium.

4.3.4 Exact Correlation Integral

For the one-dimensional model Helium atom we solve the Schrödinger equation numerically (cf. Sec. 4.2) and obtain the exact two-electron pair density via Eq. (4.8). As a reference for the quality of approximations we calculate the exact g_c (4.14) and I_c (4.16) from this solution.

Figure 4.7 shows the contour plots of the integrand of the exact I_c at time $t=T$ after interaction with the $\lambda=780$ nm, $N=3$ -cycle laser pulse for different effective peak intensities of the laser field. The structure of the integrand in the two-electron space is remarkably simple. From Eq. (4.16) it is clear that this is caused by the multiplication of the correlation function by the density, which has a maximum at the origin. For higher intensities the integrand approaches a product of a constant factor and the density at x_1 and x_2 . The integrands for the three other $N=3$ - and $N=4$ -cycle laser pulses (see Sec. 3.1) reveal a qualitatively similar structures for the respective intensities.

The values of I_c for the laser pulses with $\lambda = 614$ nm ($N = 3$) and $\lambda = 780$ nm ($N = 3, 4$) are depicted in Fig. 4.8. The qualitative dependence on the effective peak

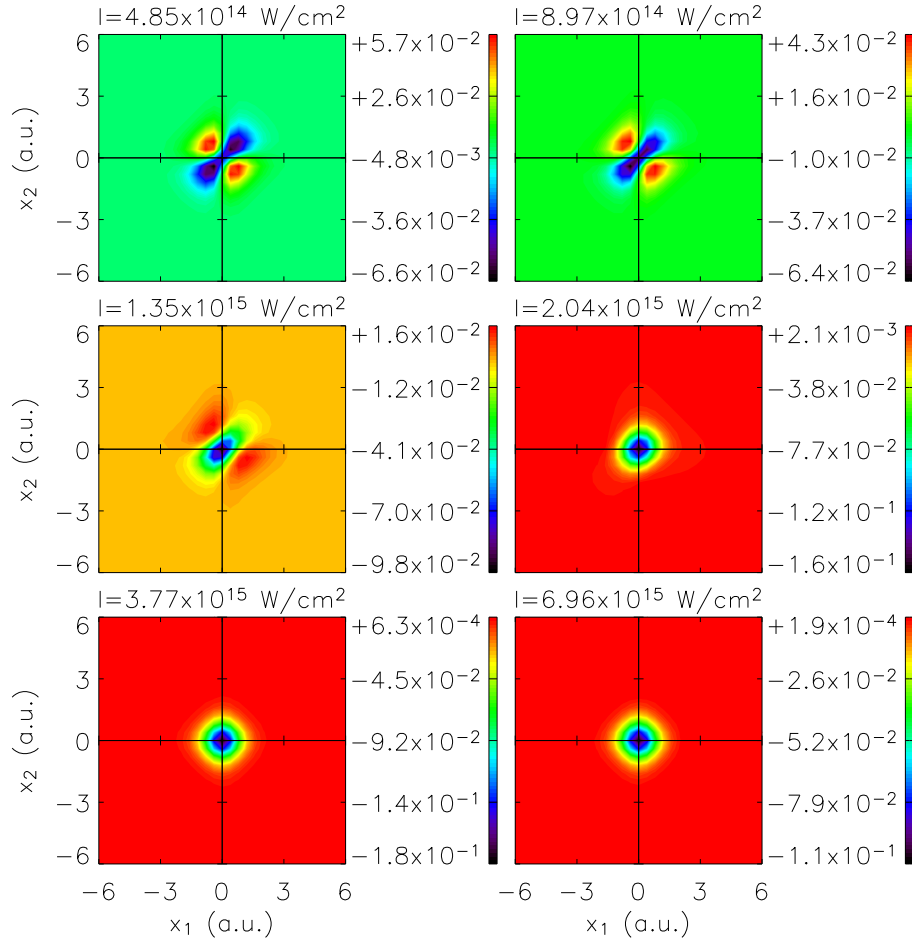


Figure 4.7: Contour plots of the exact integrand of $I_c(T)$ for different effective peak intensities of the $\lambda=780$ nm, $N=3$ -cycle laser pulse.

intensity of the laser field is similar for all three laser pulses. For the groundstate and low intensities we observe $|I_c(T)| \leq 10^{-4}$. A distinct, single minimum is found at $I \approx 3 \times 10^{-15}$ W/cm². This is the intensity regime of the onset of the “knee structure” in the double ionization probability. For larger intensities, the absolute value of I_c decreases again. The slightly deviating behavior at high intensities for the $N = 4$ laser pulse may be related to the fact that a non-negligible amount of probability density has left the grid, i.e., has been absorbed by the absorbing boundary described in Sec. A.8.

The number of bound electrons after the laser pulse is given by Eq. (3.10) as

$$N(T) = \int_{-a}^{+a} dx n(x, T). \quad (4.18)$$

The value of the correlation integral shows nearly the same quantitative dependence

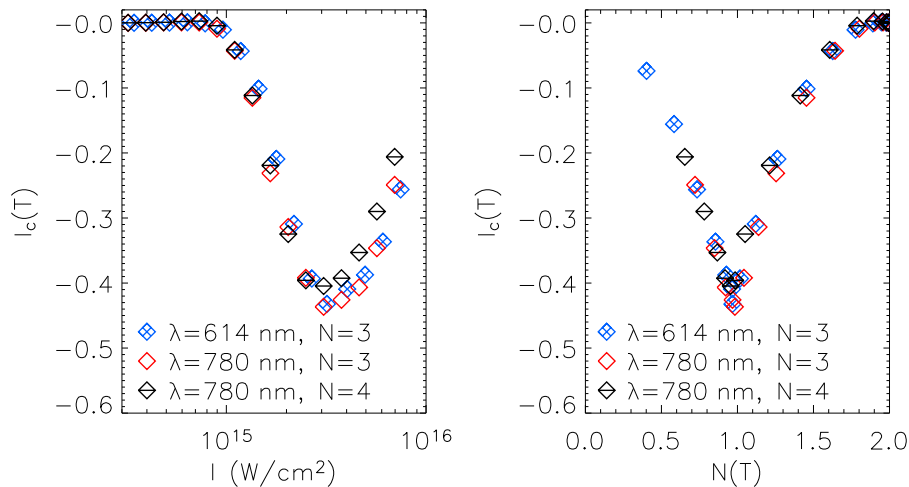


Figure 4.8: Values of $I_c(T)$ for different N -cycle laser pulses of wavelength λ as a function of the effective peak intensity (left) and the number of bound electrons after the laser pulse (right).

on $N(T)$ for all three laser pulses: A minimum of $I_c \approx -0.4$ at $N(T)=1$ and $I_c \approx 0$ at $N(T)=2$. This result might point to a more fundamental relation between I_c and $N(T)$ and thus underlines the importance of the number of bound electrons for the value of I_c . It is interesting to note that $N(t)$ is also crucial for approximating v_c in ionization processes [45,50]. Furthermore, our calculations seem to imply that $I_c[N=1-\epsilon] \neq I_c[N=1+\epsilon]$ holds, i.e., that the value of the correlation integral changes discontinuously when an integer number of bound electrons is passed. For the $\lambda=248 \text{ nm}$ laser pulse, the high frequency leads to resonant excitations of the atom for high intensities (cf. Sec. 4.2). For these intensities the dependence of I_c on both the effective peak intensity I as well as on the number of bound electrons $N(T)$ deviates to some extent from the relation found for the other laser pulses.

Using Eqs. (4.17), the values of I_c for intensities $I \leq 3 \times 10^{-15} \text{ W/cm}^2$ lead to corrections of the uncorrelated double ionization probabilities by a term of comparable size as the uncorrelated probabilities themselves. Therefore, any approximation of I_c has to be very accurate in order to yield double ionization probabilities close to the exact values.

4.3.5 Approximation of the Correlation Integral

As pointed out in Sec. 4.3.3 an approximation of $g_c(x_1, x_2, T)$ and thus of $I_c(T)$ is essential in order to make use of the correlated ionization probability functionals (4.17) for other systems than the model Helium atom. Since these functionals assure that knowledge of g_c is only needed in the immediate vicinity of the Helium nucleus after interaction with the laser pulse, approximations using groundstate properties of the model Helium atom seem promising.

It was argued [53] that approximations of the groundstate correlation function are not applicable for the description of ionization processes because they include the assumption that $g_c \rightarrow 0$ as the inter-electron distance becomes large. Thus only short-range correlations are modeled. After ionization of an atom by a laser pulse, electrons will be separated by distances large compared to inner-atomic distances in the groundstate of an atom. Therefore long-range correlations are of significant importance. However, due to Eqs. (4.17), which can be generalized to three dimensions, only the correlation function in the vicinity of the Helium nucleus is relevant to calculate ionization probabilities. Hence, to approximate I_c only correlations on the lengthscale of the groundstate correlations need to be modeled.

When trying to approximate g_c only in $\mathcal{A}(\text{He})$, it is essential to realize that the integration constraints (4.15) cannot be fulfilled anymore. This can be seen by the following argument. The integration $\int dx_i n(x_i, t) g_c(x_i, x_{j \neq i}, t) = 0$ with $i, j \in \{1, 2\}$ is carried out over the whole space for one coordinate. In the groundstate $n(|x| > a) \approx 0$ because the electrons are bound to the nucleus. Then, in order to fulfill the constraints, g_c only needs to be known for $|x_i| \leq a$. After ionization at $t = T$ however, $n(|x| > a) \neq 0$ and the constraints can be fulfilled only if g_c is also approximated for $|x_i| > a$. This is in contradiction to our assumption that we approximate g_c only in $\mathcal{A}(\text{He})$.

We will present three different approaches to the approximation of the correlation integral I_c . First, we use densities after the interaction with the laser pulse in a groundstate correlation function (Sec. 4.3.6). Then we will show in Sec. 4.3.7 how results can be significantly improved by introducing an adiabatic approximation of g_c . Finally it is shown that using a fit function to describe $I_c(N)$ offers an additional promising route to approximate the correlated ionization probability functionals (Sec. 4.3.8).

4.3.6 Becke Approximation

One possibility to approximate g_c is to make use of well-established correlation functions for stationary states from groundstate density functional theory and incorporate a time-dependence by using the density at the respective time t [40]:

$$g_c[n](x_1, x_2, t) \approx g_c[n(t)](x_1, x_2). \quad (4.19)$$

This approach was applied [40] for two different approximations of the groundstate correlation function [54, 55] to calculate I_c for Helium after interaction with a laser field. Using densities from a three-dimensional time-dependent density functional calculation yielded values for I_c which were significantly too low to correct the uncorrelated ionization probabilities [40].

For our one-dimensional system, one of these groundstate correlation functions, the Becke correlation function [40, 54], is given by

$$g_c^{\text{B}}(x_1, x_2, t) = \frac{(|x_1 - x_2| - z(x_1))}{2(1 + z(x_1))} \frac{n(x_1, t)}{n(x_2, t)} F(\gamma |x_1 - x_2|), \quad (4.20)$$

with z and γ functions of the time t . The ‘‘correlation length’’ $z(x_1, t)$ gives the inter-electron distance at which the correlation function g_c changes its sign. In the groundstate case the correlation length is written as $z(x) = 2cR_F(x)$. The ‘‘Fermi hole radius’’ $R_F(x)$ is deduced from a functional for the exchange energy $E_x = -\frac{1}{2} \int dx n(x) (R_F(x))^{-1}$. Using the local density approximation (LDA) functional the proportionality constant c was found to be $c = 0.62$ by comparison with an established parameterization of the functional [54]. For the Helium atom the Hartree-Fock exchange energy functional $E_x = -\frac{1}{2} \int dx n(x) (v_h(x)/2)$ is the exact exchange energy functional, yielding $R_F(x) = 2/v_h(x)$. We therefore have $z(x, t) = 2.48/v_h(x, t)$ [40].

For the damping function $F(x)$ several choices were suggested [54] which all exhibit quadratic behavior for small x , ensuring the validity of the short-range expansion of the pair density employed to derive Eq. (4.20). Since results are found to be insensitive to the choice of the damping function we only make use of

$$F(x) = (1 + x) e^{-x}. \quad (4.21)$$

The parameter $\gamma = \gamma(x_1, t)$ in Eq. (4.20) is chosen to fulfill the integration constraint (4.15) with respect to x_2

$$\int dx_2 n(x_2, t) g_c^B(x_1, x_2, t) = 0. \quad (4.22)$$

Since z depends only on x_1 this yields with $u = \gamma|x_1 - x_2|$ the explicit equation for the one-dimensional case

$$\gamma(x_1, t) = \frac{1}{z(x_1, t)} \frac{\int_0^\infty du u F(u)}{\int_0^\infty du F(u)}. \quad (4.23)$$

For the damping function (4.21) employed here this gives $\gamma(x_1, t) = 3/[2z(x_1, t)]$.

The exact g_c is symmetric in the electron coordinates x_1, x_2 . In contrast, the Becke correlation function uses x_1 as a ‘‘reference variable’’ around which an expansion of the pair density is carried out. It should be noted however, that the correlation integral I_c^B which follows as

$$\begin{aligned} I_c^B &= \int_{-a}^{+a} dx_1 \int_{-a}^{+a} dx_2 n(x_1) n(x_2) g_c^B(x_1, x_2, t) \\ &= \int_{-a}^{+a} dx_1 \int_{-a}^{+a} dx_2 [n(x_1)]^2 \frac{(|x_1 - x_2| - z)}{2(1+z)} F(\gamma|x_1 - x_2|), \end{aligned} \quad (4.24)$$

with I_c^B and n functions of time t and $z = z(x_1, t)$, $\gamma = \gamma(x_1, t)$, yields the same value for the Becke construction with respect to x_2 . This can be seen by interchanging indices in Eq. (4.24).

From Fig. 4.9 we infer that in our case Eq. (4.20) yields values for the correlation integral $I_c^B(T)$ which are far from the exact results even when the densities of the exact Kohn-Sham orbital are used. In addition, it does not reproduce the marked

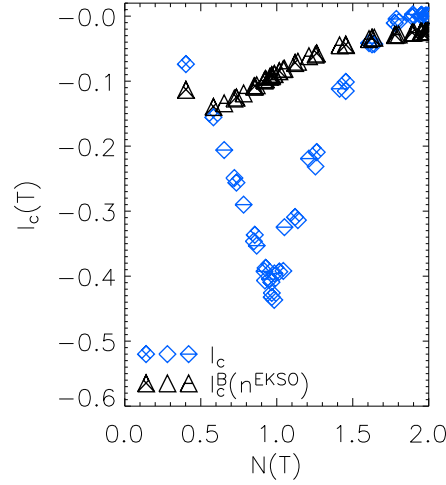


Figure 4.9: Value of the Becke approximation $I_c^B(T)$ of the correlation integral as a function of the number of bound electrons $N(T)$ compared to the exact values $I_c(T)$. The exact densities (n^{EKS0}) were used as inputs for $I_c^B(T)$. Results for three different laser pulses are shown with different symbols (cf. Fig. 4.8).

minimum at $N(T) = 0$. In contrast to earlier work [40] the order of magnitude of I_c^B is, however, correct.

The derivation of Eq. 4.20 is based on an expansion of the pair density for short inter-electron distances, which in turn is related to the expansion of a two-electron wavefunction around $|\mathbf{r}_1 - \mathbf{r}_2| = 0$ [56, 57]. In the latter case, the prefactors for the first terms of the expansion are derived by ensuring that the three-dimensional Schrödinger equation is fulfilled for the expanded wavefunction for $|\mathbf{r}_1 - \mathbf{r}_2| \rightarrow 0$. A similar approach employing the one-dimensional Schrödinger equation of the model Helium atom with soft-core potentials does not yield the same results. This is a possible reason why even for the groundstate at $t_0 = 0$ the Becke correlation function in the form of Eq. (4.20) does not give a sensible result for I_c^B .

The Becke model yields $g_c^B = 0$ for large inter-electron distances due to the damping function $F(\gamma|x_1 - x_2|)$. The damping factor γ is constructed in a way that the integration constraint (4.22) is always fulfilled. As pointed out in Sec. 4.3.5 an approximation of g_c which is valid only in the vicinity of the Helium nucleus will not fulfill the integration constraints at time $t = T$ because the density has non-negligible values for $|x_i| > a$. Hence, the damping function forces the Becke correlation function to give incorrect values, although, as our adiabatic approximation shows, an approximation of g_c from groundstate properties can be successful.

4.3.7 Adiabatic Approximation

In order to find an approximation for the exchange-correlation function (4.9) we approximate numerator and denominator separately using groundstate (pair) den-

sities. The relation $g_c = g_{xc} - \frac{1}{2}$ then allows us to calculate g_c and thus via I_c the correlated ionization probability functionals (4.17).

In this section we will refer to groundstate densities of an i -electron system by n_i and to groundstate pair densities of an i -electron system by ρ_i .

Adiabatic Density

The density of our model Helium atom close to the Helium nucleus is assumed to be a linear combination of the groundstate densities of two-, one- and zero-electron systems [45, 50],

$$n^A(x, t) = \begin{cases} [1 - N(t)] n_0(x) + N(t) n_1(x) & 0 \leq N(t) \leq 1 \\ [2 - N(t)] n_1(x) + [N(t) - 1] n_2(x) & 1 \leq N(t) \leq 2 \end{cases}, \quad (4.25)$$

weighted by factors related to the fractional number of bound electrons (3.10)

$$N(t) = \int_{-a}^{+a} dx n(x, t). \quad (4.26)$$

The coefficients determine the relative contribution of the integer-electron groundstate densities to the system with fractional electron number $N(t)$. Since $n(x) dx$ is the probability to find an electron at x in dx , the groundstate density for the zero-electron system has to vanish: $n_0 = 0$. For our system, $n_1(x)$ is the groundstate density of He^+ , which is calculated from the solution of the respective one-dimensional stationary Schrödinger equation (cf. Sec. 3.6). Consistently we use $n_2(x) = n(x, t = 0)$ where n denotes the density utilized to calculate $N(t)$ in Eq. (4.26).

Construction of a normalized Kohn-Sham orbital from $n^A(x, t)$ allows the calculation of the respective groundstate correlation potential v_c using the stationary Kohn-Sham equation [45]. It was recently shown that calculating this v_c for each time t and using it in a time-dependent Kohn-Sham calculation of the ionization process of Helium yields orbitals with uncorrelated ionization probabilities (4.4) in good agreement with the probabilities for the exact Kohn-Sham orbital [50]. This corroborates further the assumption that the form of Eq. (4.25) is a good approximation of the density of the system close to the nucleus.

Adiabatic Pair Density

Since an adiabatic approximation of the density of the system has proven successful for the calculation of v_c (cf. comments in the previous section) and due to the central role of $N(t)$ for the value of I_c indicated by the results of Sec. 4.3.4 we approximate the pair density analogously to the density of the system.

Assuming the same adiabatic dependence of $\rho^A(t)$ on $N(t)$ as for the density yields

$$\rho^A(x_1, x_2, t) = \begin{cases} [1 - N(t)] \rho_0 + N(t) \rho_1 & 0 \leq N(t) \leq 1 \\ [2 - N(t)] \rho_1 + [N(t) - 1] \rho_2 & 1 \leq N(t) \leq 2 \end{cases}. \quad (4.27)$$

where $\rho_i = \rho_i(x_1, x_2)$. From Eq. (4.8) we know

$$\rho_2(x_1, x_2) = 2 |\psi(x_1, x_2, t_0)|^2. \quad (4.28)$$

In Sec. 4.3.3 we pointed out that the pair density is proportional to the joint probability to find an electron at x_1 in dx_1 and an electron at x_2 in dx_2 . From this interpretation follows

$$\rho_0(x_1, x_2) = 0, \quad \rho_1(x_1, x_2) = 0. \quad (4.29)$$

Rewriting Eq. (4.27) by using Eq. (4.29), the adiabatic approximation of the pair density is

$$\rho^A(x_1, x_2, t) = \begin{cases} 0 & 0 \leq N(t) \leq 1 \\ [N(t) - 1] \rho_2(x_1, x_2) & 1 \leq N(t) \leq 2 \end{cases}. \quad (4.30)$$

This result means that for $N(t) \leq 1$ all correlation effects vanish, i.e., only a one-electron system is left containing no information about the fact that one electron belonging to the original system has been detached from the atom. This might suggest the necessity to include memory effects in a refined approximation of the pair density.

Adiabatic Correlation Integral

With the adiabatic approximations n^A (4.25) and ρ^A (4.30) we use Eq. (4.14) to arrive at an adiabatic approximation of the correlation function

$$g_c^A(x_1, x_2, t) = \begin{cases} -\frac{1}{2} & 0 \leq N(t) \leq 1 \\ \frac{\rho^A(x_1, x_2, t)}{n^A(x_1, t) n^A(x_2, t)} - \frac{1}{2} & 1 \leq N(t) \leq 2 \end{cases}. \quad (4.31)$$

It should be noted that in this form, the approximation returns the exact correlation function for the groundstate at $t_0 = 0$. Due to its relation to groundstate properties our adiabatic approximation can only be valid in the immediate vicinity of the Helium nucleus. Therefore it does not fulfill the integration constraints (4.15) as explained in Sec. 4.3.5.

The correlation integral I_c^A can now be calculated from Eq. (4.16) using the same densities as in $N(t)$ (4.26). To compute I_c^A the following inputs are needed: The density of the system for all times, the groundstate density of He^+ and the groundstate pair density. The density can in principle be obtained by a time-dependent density functional calculation with the correct choice for v_c . The groundstate inputs are accessible numerically also for more complex atomic systems than Helium. Furthermore, the groundstate pair density in full dimensionality can be calculated approximately via one of the approximations for the groundstate correlation function discussed in Sec. 4.3.6. Then only densities are needed as inputs.

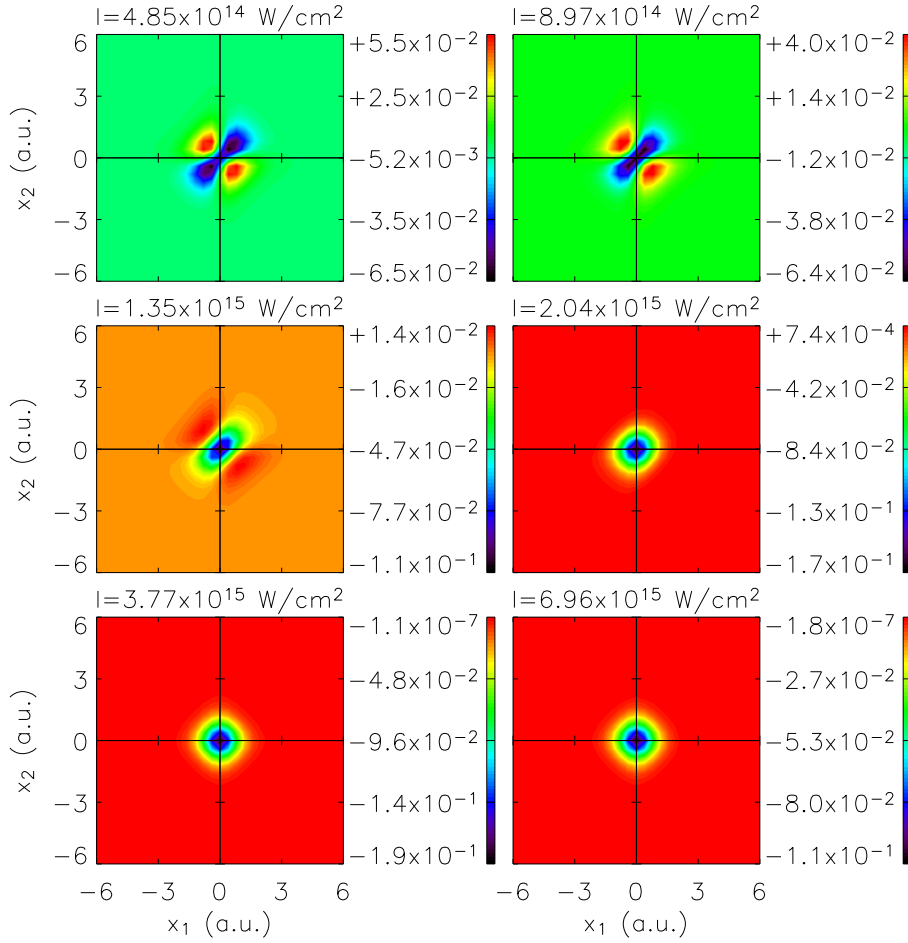


Figure 4.10: Contour plots of the integrand of the adiabatic approximation $I_c^A(T)$ using the densities of the exact Kohn-Sham orbital for different effective peak intensities of the $\lambda=780$ nm, $N=3$ -cycle laser pulse.

Figure 4.10 shows the integrand of the adiabatic correlation integral $I_c^A(T)$ using the densities of the exact Kohn-Sham orbital for the $\lambda = 780$ nm, $N = 3$ -cycle laser pulse. The qualitative agreement with the exact integrand shown in Fig. 4.7 is generally good. Furthermore, the maximum and minimum values of the integrand are close to the exact values. This is a strong indication that the adiabatic approximation of g_c captures the essential features which contribute to I_c . For the other laser pulses the agreement is similarly good, except for the $\lambda = 248$ nm pulse. In this case (as explained in Sec. 4.3.4) resonant excitations of the model Helium atom are present, a situation not included in our approximation which assumes the bound density to be in the groundstate.

In Sec. 4.3.4 we described that I_c depends on $N(T)$ in a similar way for the $\lambda = 614$ nm ($N = 3$) and $\lambda = 780$ nm ($N = 3, 4$) laser pulses. The value of $I_c^A(T)$ as

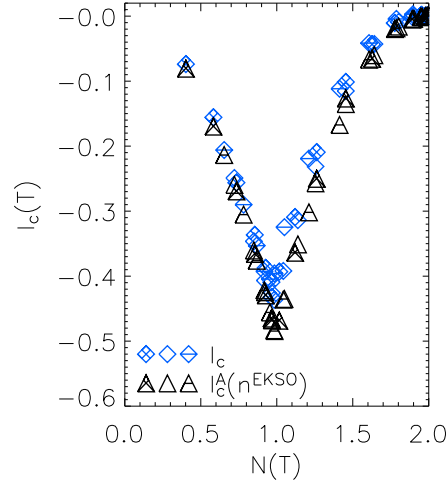


Figure 4.11: Adiabatic approximation of the correlation integral $I_c^A(T)$ calculated using densities of the exact Kohn-Sham orbital (n^{EKS0}) compared to the exact values $I_c(T)$ as a function of the number of bound electrons $N(T)$. Results for three different laser pulses are shown with different symbols (cf. Fig. 4.8).

calculated from the exact densities n^{EKS0} is compared to the exact value (4.16) in Fig. 4.11. The adiabatic approximation exhibits qualitatively the same dependence on the number of bound electrons as the exact values. However, for $N(T) \approx 1.0$ the value differs significantly from the exact result and is $I_c^A = -1/2$ for $N(T) = 1$.

With $I_c^A(T)$ and Eqs. (4.14) we have thus found an approximation of the correlated ionization probability functionals. For $N(T) = 1$, $I_c^A = -1/2$ yields the unphysical value $P^{2+}(T) = 0$. However, good results are already acquired for $N(T)$ only slightly smaller or larger than one, as is shown below. Figure 4.12 depicts ionization probabilities calculated from EKS0 and LK05 densities for the $\lambda = 780$ nm, $N = 3$ cycle laser pulse. Comparing these results to the results from the uncorrelated functionals (4.4) in Figs. 4.4 and 4.5 evidences a significant improvement. The systematically too low values for the single ionization probability in the range $I \approx 1 - 8 \times 10^{15}$ W/cm² are corrected, while for lower intensities the LK05 probabilities remain too low. Double ionization probabilities show a good agreement for high intensities. For low intensities the double ionization probabilities (and I_c^A) are so small that already small deviations of I_c^A from the exact I_c lead to relatively large deviations in the logarithmic plot of the ionization probabilities and to minima and maxima in the double ionization probability. Since $I_c^A = -1/2$ at $N(T) = 1$, i.e., $P^{2+} = 0$ the adiabatically corrected probabilities show a minimum at intensities when the curvature of the exact probabilities changes its sign at the onset of the “knee-structure”.

An alternative approach to an adiabatic approximation of I_c exists. With Eqs. (4.16) and (4.14) the densities in the first term cancel and only an adiabatic approximation of $\rho(x_1, x_2, t)$ is necessary. However, this yields $P^{2+}(T) = 0$ for all

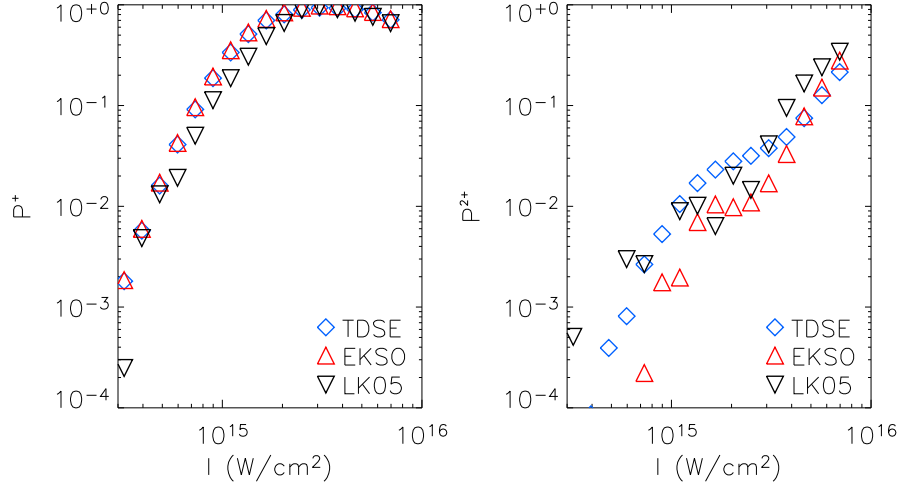


Figure 4.12: Ionization probabilities as a function of the effective peak intensity calculated using the adiabatic approximation $I_c^A(T)$ in the correlated ionization probability functionals. Results obtained with the exact densities (EKSO) and LK05 densities are compared to the Schrödinger solution (TDSE) for the $N=3$ cycle laser pulse with $\lambda=780$ nm.

$N(T) \leq 1$. In addition, the agreement of the contour plots of the integrand with the exact integrand is not as good as in our approximation. This indicates that the approach described above is superior because it approximates the correlation function as a whole and thus relates pair densities and densities computed using the same approximation.

With the adiabatic approach we have thus identified an approximation of the correlation function g_c close to the Helium nucleus and hence of the correlated ionization probability functionals which significantly improves the results for ionization probabilities compared to the uncorrelated functionals [58].

4.3.8 Fit Function Approximation

In Sec. 4.3.4 we found that the value of the correlation integral $I_c(T)$ depends on the number of bound electrons $N(T)$ in a quantitatively similar way for the $\lambda=614$ nm ($N=3$) and $\lambda=780$ nm ($N=3, 4$) laser pulses. Therefore we approximate I_c by using a parameter-dependent fit function $I_c^F[N(t)]$ and determine the parameters by fitting to the results from the exact I_c for all three pulses.

Based on the results for $N(T)$ depicted in Fig. 4.8 we choose the general dependence on the number of bound electrons as

$$I_c^F(t) = \begin{cases} a |N(t) - 1| e^{-|N(t)-1|} + b & 0 \leq N(t) \leq 1 \\ a |N(t) - 1| e^{-|N(t)-1|} + c & 1 \leq N(t) \leq 2 \end{cases} . \quad (4.32)$$

Since the exact values I_c from our calculations imply that $I_c[N=1-\epsilon] \neq I_c[N=1+\epsilon]$

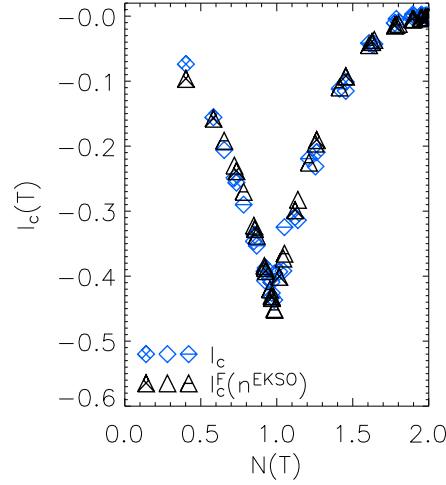


Figure 4.13: Comparison of the fit function approximation of the correlation integral $I_c^F(T)$ calculated using the exact densities n^{EKS0} with the exact values of $I_c(T)$ as a function of $N(T)$. Results for three different laser pulses are shown with different symbols (cf. Fig. 4.8).

as described in Sec. 4.3.4 we choose b and c differently depending on whether the number of bound electrons is above or below one.

One should note that I_c^F is a functional of the density because $N(t)$ is an integral over the density (cf. Eq. (4.26)). Using the results $N(T)$ and the values $I_c[N(T)]$ from the time-dependent Schrödinger equation for the different effective peak intensities of the three laser pulses, a least squares fit yields $a = 1.1335$, $b = -0.4694$ and $c = -0.4196$. The value of the root-mean-square error

$$\left\langle \left[I_c^F(N) - I_c(N) \right]^2 \right\rangle^{1/2} = 1.48 \times 10^{-2} \quad (4.33)$$

shows that this approach yields a generally good agreement with the exact I_c . This is confirmed by Fig. 4.13 which compares the values of $I_c^F(T)$, where $N(T)$ is calculated from the densities of the exact Kohn-Sham orbital n^{EKS0} , to the exact values $I_c(T)$.

Using $I_c^F(T)$ in the correlated ionization probability functionals (4.16) yields functionals which depend only on the density. Calculations with the exact (n^{EKS0}) and LK05 densities (n^{LK05}) are shown in Fig. 4.14 for the $\lambda = 780$ nm, $N = 3$ -cycle laser pulse. In both cases the “knee structure” is clearly reproduced and overall agreement with the ionization probabilities from the Schrödinger solution is good for intensities $I \geq 1 \times 10^{15}$ W/cm². For lower intensities probabilities are systematically too low (the probabilities are of the order of the root-mean-square error in this intensity regime).

Using the fit function approximation I_c^F of course requires the dependence of I_c on $N(T)$ to be independent of the laser pulse used. The results for the three pulses in Sec. 4.3.4 show that this seems to be a reasonable assumption. As discussed

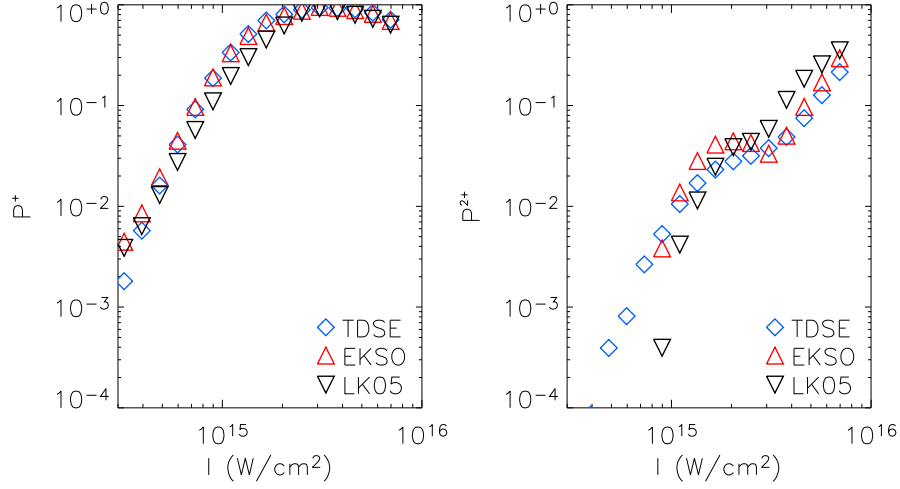


Figure 4.14: Single and double ionization probabilities for exact (EKSO) and LK05 densities using the fit function approximation of the correlated ionization probability functionals compared to the results from the time-dependent Schrödinger equation (TDSE). Probabilities are shown as a function of the effective peak intensity of the $N=3$ cycle laser pulse with $\lambda=780$ nm.

in Sec. 4.3.4 this does hold true only partly when resonant excitations in the atom take place as in the case of the $\lambda = 248$ nm laser pulse. Nevertheless the fit function approximation still yields a reasonable correction to ionization probabilities in this case, while the adiabatic approximation I_c^A presented in Sec. 4.3.7 fails to provide a good approximation because of it being based on the assumption that the density remaining bound is in the groundstate.

In addition to the general adiabatic approximation of the correlation function g_c we have thus identified a simpler approach to obtain approximations for the correlated ionization probability functionals (4.17), as the groundstate pair density is not required as an input.

Chapter 5

Momentum Distributions

As explained in Chapter 4 in a Helium atom interacting with a few-cycle laser pulse double ionization proceeds non-sequentially in a certain intensity regime. By analyzing the distribution of electron and ion momenta after the double ionization further details of how this process works can be obtained. We introduce the momentum pair density of the free electrons (Sec. 5.1) and the ion momentum density (Sec. 5.2). A classical picture of the possible non-sequential double ionization processes is presented (Sec. 5.3) and shown to be in agreement with results from the time-dependent Schrödinger equation for our model Helium atom (Sec. 5.4). Calculation of momentum distributions from a time-dependent density functional treatment by using uncorrelated functionals is shown to be insufficient (Sec. 5.5.1) while providing a further measure of the quality of approximations of the correlation potential v_c (Sec. 5.5.2). A promising route to correlated functionals for momentum distributions is presented (Sec. 5.5.3).

It should be noted that at times $t < T$ during the laser pulse the velocity of the electrons is actually given by $d_t x_i(t) = k_i(t) + A(t)$, i.e., the sum of the canonical momentum k_i and the value of the vector potential at the respective time. The results and equations presented in this chapter refer to canonical momenta k only because the drift momentum of the electrons at time $t = T$ after the laser pulse is identical to the canonical momentum at that time as $A(T) = 0$.

As we are interested in identifying approaches to reproduce results of the time-dependent Schrödinger equation using time-dependent density functional theory we will restrict ourselves to the $\lambda = 780$ nm, $N = 3$ -cycle laser pulse. We stress however that the general conclusions drawn hold also for the $\lambda = 614$ nm, $N = 3$ and $\lambda = 780$ nm, $N = 4$ laser pulses.

5.1 Calculation of the Momentum Pair Density

After interaction with a laser pulse the correlated two-electron wavefunction of the model Helium atom is given by $\psi(x_1, x_2, T)$. As we know from basic quantum mechanics [59] the wavefunction can be described equivalently in momentum space

by Fourier transforming it

$$\psi(k_1, k_2, t) = (2\pi)^{-1} \int dx_1 \int dx_2 \psi(x_1, x_2, t) e^{-i(k_1 x_1 + k_2 x_2)}. \quad (5.1)$$

Since $\int dk_1 \int dk_2 |\psi(k_1, k_2, t)|^2 = 1$ the pair density in momentum space is given by $\rho(k_1, k_2, t) = 2 |\psi(k_1, k_2, t)|^2$.

We are interested mainly in the double ionization process and thus Fourier transform only the wavefunction in the area $\mathcal{A}(\text{He}^{2+})$ (4.2) associated with double ionization. The resulting sharp step at the boundary of $\mathcal{A}(\text{He}^{2+})$ at $|x_i| = a$, $|x_{j \neq i}| \geq a$ with $i, j \in \{1, 2\}$ is a potential source of artifacts when Fourier transformed. Hence, a “smoothing” function

$$f(x_1, x_2) = \frac{1}{\sqrt{1 + e^{-c|x_1 - a|}}} \frac{1}{\sqrt{1 + e^{-c|x_2 - a|}}} \quad (5.2)$$

is introduced. The factor c has to be of the order of one, in this work we choose $c = 1.25$ while $a = 6$ a.u. (as explained in Sec. 4.1). The smoothing function is constructed so that $\iint dx_1 dx_2 f^2(x_1, x_2) b = \iint_{\mathcal{A}(\text{He}^{2+})} dx_1 dx_2 b$ for a constant b . This condition ensures that the wavefunction $\psi^{(2+)}(x_1, x_2, t) = f(x_1, x_2) \psi(x_1, x_2, t)$ gives to a good approximation the same double ionization probability as the original wavefunction, i.e., that $\int dx_1 \int dx_2 f^2(x_1, x_2) |\psi(x_1, x_2, t)|^2 \simeq P^{2+}$.

After double ionization of the model Helium atom the correlated wavefunction of the electrons freed in double ionization in momentum space is thus calculated as

$$\psi^{(2+)}(k_1, k_2, t) = (2\pi)^{-1} \int dx_1 \int dx_2 \psi^{(2+)}(x_1, x_2, t) e^{-i(k_1 x_1 + k_2 x_2)}. \quad (5.3)$$

This approach is equivalent to projecting out the states corresponding to single and no ionization and is known to lead to valuable momentum distributions [48]. From the wavefunction we construct the momentum pair density of the electrons freed in double ionization

$$\rho^{(2+)}(k_1, k_2, t) = 2 |\psi^{(2+)}(k_1, k_2, t)|^2. \quad (5.4)$$

The probability to find at time t an electron freed in double ionization with momentum k_1 in dk_1 and an electron with k_2 in dk_2 is then $\rho^{(2+)}(k_1, k_2, t) dk_1 dk_2$.

5.2 Calculation of the Ion Momentum Density

In experiments, it is easier to measure the momentum of the He^{2+} ion k_{Ion} after double ionization instead of individual electron momenta. As the photon momenta are negligibly small in the intensity regime of interest, this provides information about the sum of the electron momenta via momentum conservation

$$k_1 + k_2 = -k_{\text{Ion}}. \quad (5.5)$$

From the wavefunction of the electrons freed in double ionization in momentum space (5.3) the ion momentum density follows with Eq. (5.5) as

$$\begin{aligned} n_{\text{ion}}^{(2+)}(k_{\text{Ion}}, t) &= \frac{1}{2} \int dk \rho^{(2+)}(-k_{\text{Ion}} - k, k, t) \\ &= \frac{1}{2} \int dk \rho^{(2+)}(k, -k_{\text{Ion}} - k, t), \end{aligned} \quad (5.6)$$

due to the symmetry of the electron momentum pair density. The factor $1/2$ ensures the correct normalization, since the system consists of only one ion but two electrons. The ion momentum density $n_{\text{ion}}^{(2+)}(k_{\text{Ion}}, t) dk_{\text{Ion}}$ gives the probability to find at time t the He^{2+} ion with momentum k_{Ion} in dk_{Ion} .

5.3 Classical Picture of Double Ionization

The different double ionization processes and the resulting ion momentum density are highlighted by a classical description of the ionization process. For the $\lambda = 780$ nm, $N = 3$ -cycle laser pulse and the intensities studied in this work the system is in the tunneling regime. Therefore, the first electron is preferentially emitted when the electric field $E(t) = -\partial_t A(t)$ has a maximum, i.e., when the vector potential goes through zero $A(t_1^e) = 0$. Classically, we have for the kinetic momentum of the electron $p(t) = A(t) - A(t_1^e)$. Hence, the first electron leaves the atom by tunneling with zero initial momentum. The same holds true for sequential ionization of a second electron without interaction with the first electron. Then, after the laser pulse, because $A(T) = 0$ and with Eq. (5.5) an ion momentum density centered around a maximum at zero momentum is expected. However, the first electron can return to the He^+ ion. This may happen at $A(t) \neq 0$. The momentum of the recolliding first electron may be shared with the bound electron, which in turn may be dislodged as well. If recollision occurs at $|A(t)| \approx \hat{A}_{\text{eff}}$, i.e., close to the maximum of the vector potential, the absolute value of the final sum momentum of the two electrons will be at most $2\hat{A}_{\text{eff}} = 4\sqrt{U_p}$ with the ponderomotive potential $U_p = \hat{A}_{\text{eff}}^2/4$. Since the sum of the electron momenta is via momentum conservation (5.5) equal to the negative ion momentum this recollision process results in an ion momentum distribution with distinct maxima at non-zero momenta. In case the first electron returns to the ion, it can also excite the second electron which is freed during a later laser cycle at $A(t_2^e) = 0$ [12]. Then, the resulting ion momentum is the negative of the remaining momentum of the first electron, which in general will be small. This entails an ion momentum density with a maximum at zero momentum, which is broadened compared to the density for sequential ionization.

5.4 Momentum Distributions from the TDSE

From our numerical solution of the time-dependent Schrödinger equation we obtain $\psi(x_1, x_2, t)$ in the two-electron real space as a matrix on the numerical grid (cf. Sec. A.3). To implement the equations of Secs. 5.1 and 5.2, we use a fast Fourier transformation algorithm. Integrals are approximated by a Riemann sum while infinite integral limits are replaced by the boundaries of the numerical grid.

5.4.1 Momentum Pair Density

The analysis of the momentum pair density of the electrons freed in double ionization reveals a wealth of information about the double ionization process. In Fig. 5.1 the pair density at the end of the laser pulse at time $t = T$ as calculated from the solution of the time-dependent Schrödinger equation and Eq. (5.4) is shown. For all but the highest intensity depicted, electrons have the highest probability to move at different velocities $|k_1| \neq |k_2|$ ($d_t x_i(T) = k_i(T)$ since $A(T) = 0$) but in the same direction ($\text{sgn}(k_1) = \text{sgn}(k_2)$). Depending on the intensity of the laser pulse the probability for the double ionization process is highest at different half-cycles of the laser pulse, i.e., different signs of the vector potential. Therefore, the favored direction in which the electrons leave the atom varies with intensity. As explained in Sec. 5.3 non-sequential double ionization can be understood by a recollision mechanism where one electron returns to the He^+ ion and frees the second electron. The results of the time-dependent Schrödinger equation then imply that both electrons leave the atom in the same direction but due to Coulomb repulsion their velocities differ. The “butterfly” shape of the momentum pair density as in Fig. 5.1 is evidence that the momentum pair density is highly correlated as it cannot be reproduced by multiplying two orbitals for the respective electrons.

For $I = 6.96 \times 10^{15} \text{ W/cm}^2$ both electrons have the highest probability to leave the atom in the same direction with similar velocities $k_1 \approx k_2$. As pointed out above, this can only be the case when the Coulomb repulsion between the electrons is weak, i.e., when they are removed sequentially, resulting in a large spatial separation. The fact that double ionization proceeds sequentially at this intensity is corroborated by Fig. 4.3 which shows that the double ionization probability can be reproduced by a sequential ionization model. The final non-vanishing velocities are due to the high intensity of the laser pulse which ionizes the atom so rapidly that $A(t_1^e) \neq 0$. The grid-like structure typical for a product wavefunction is seen, the electron correlation being weak.

5.4.2 Ion Momentum Density

From the momentum pair density $\rho^{(2+)}(k_1, k_2, T)$ of the electrons freed in double ionization which is obtained from the solution of the time-dependent Schrödinger equation we calculate the ion momentum density $n_{\text{ion}}^{(2+)}(k_1, k_2, T)$ (5.6). For different effective peak intensities the density of the ion momentum is depicted in Fig. 5.2.

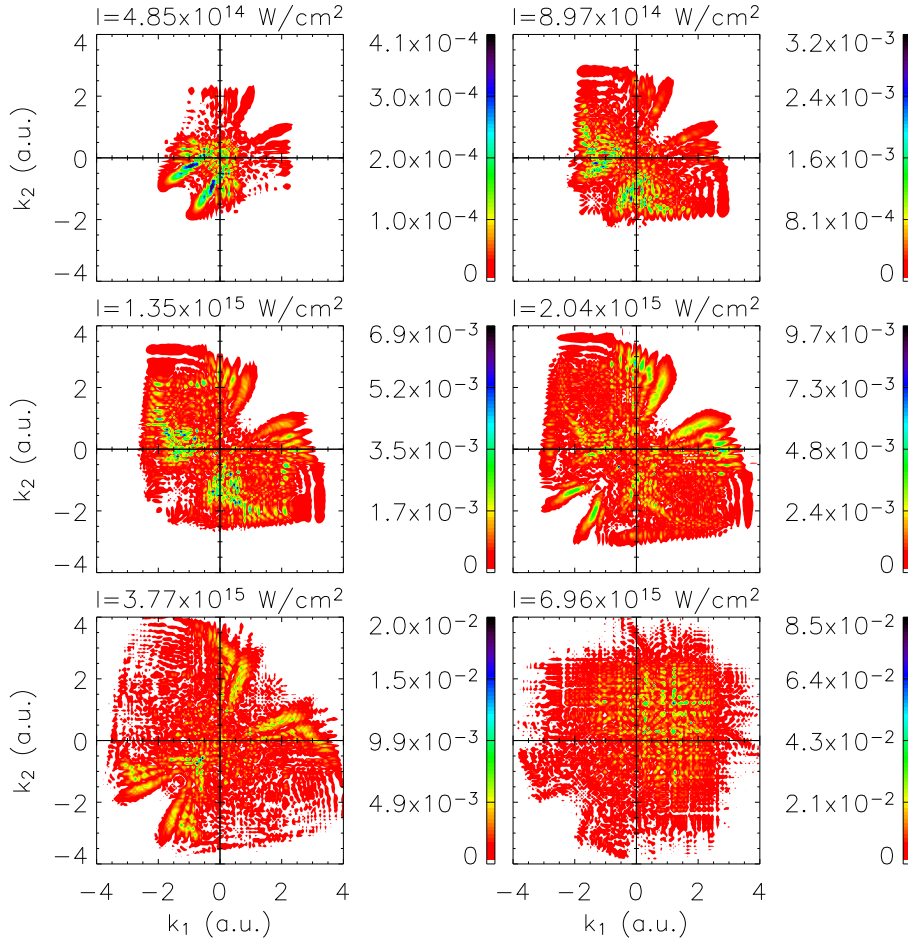


Figure 5.1: Contour plots of the momentum pair density $\rho^{2+}(k_1, k_2, T)$ of the electrons freed in double ionization. Results calculated from the time-dependent Schrödinger equation are shown for different effective peak intensities of the $\lambda=780$ nm, $N=3$ -cycle laser pulse.

It exhibits peaks at non-zero momenta which are typical for recollision processes (cf. Sec. 5.3). For an infinitely long laser pulse of cycle-length T/N , $\hat{H}(t + T/N) = \hat{H}(t)$ holds. This symmetry is broken in the case of few-cycle laser pulses, i.e., $\hat{H}(t + T/N) \neq \hat{H}(t)$. Hence, with respect to the dislodged electrons there is no spatial inversion symmetry, leading to asymmetric ion momentum distributions [13, 60]. This effect is clearly seen in Fig. 5.2. For the three lowest intensities a process with $k_{\text{Ion}} \geq 0$ dominates while with increasing intensities processes with $k_{\text{Ion}} \leq 0$ become more likely. In addition, a central peak gets more and more pronounced, showing that the relative probability of sequential double ionization increases. The fact that the peak is not centered around $k_{\text{Ion}} = 0$ for $I = 6.96 \times 10^{15}$ W/cm² is due to the high intensity of the laser pulse as explained in Sec. 5.4.1.

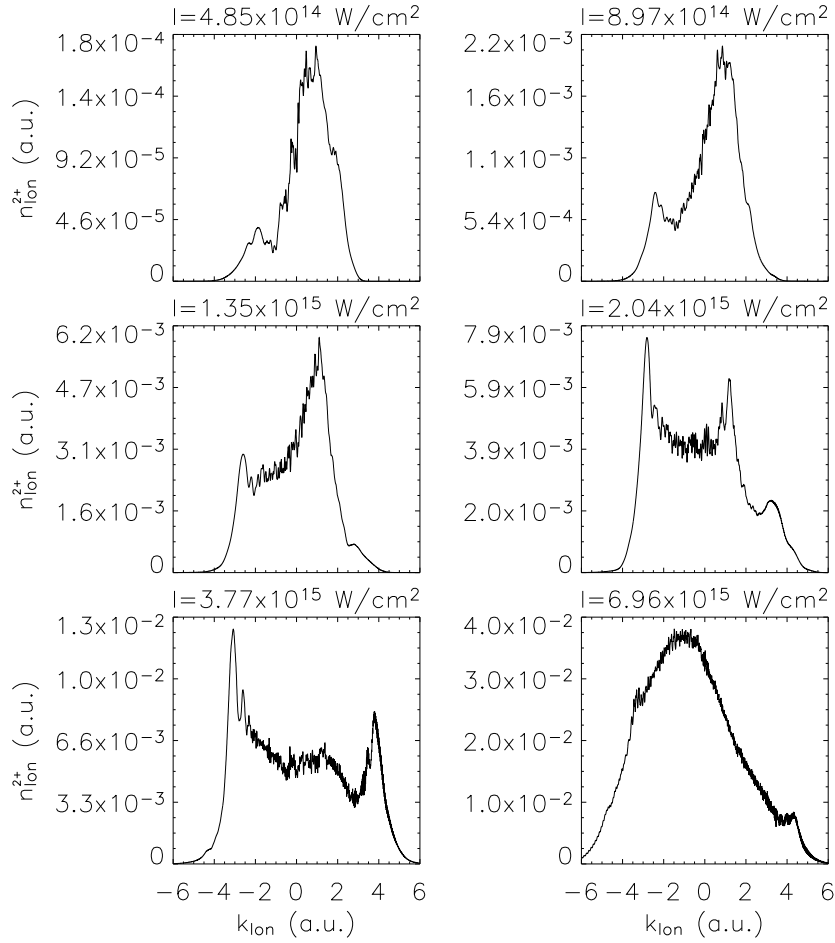


Figure 5.2: Ion momentum density of the model He^{2+} at time $t = T$ for different effective peak intensities of the $\lambda = 780$ nm, $N = 3$ -cycle laser pulse.

5.5 Momentum Distributions from TDDFT

Determining momentum pair densities and ion momentum densities from a time-dependent density functional approach faces two challenges, just the calculation of ionization probabilities from the Kohn-Sham orbitals in Sec. 4.3. The first is to find an approximation of the correlation-potential v_c to reproduce the exact density $n(x, t)$ while the second is to assign a suitable functional of the density to the respective observable. As both the ion momentum density and the momentum pair density (via their probability interpretations, cf. Secs. 5.1 and 5.2) are observables, the Runge-Gross theorem again assures that functionals of the density alone exist (Sec. 2.1).

As pointed out in Chapter 3, a time-dependent density functional calculation for the model Helium atom yields identical Kohn-Sham orbitals $\phi(x, t)$ for the two

electrons. The momentum pair density of the electrons freed in double ionization $\rho^{(2+)}(k_1, k_2, t)$ (5.4) is the Fourier transform of the correlated wavefunction $\psi(x_1, x_2, t)$. Furthermore, the ion momentum density (5.6) can be calculated from the momentum pair density by an integration in momentum space. It is therefore straightforward to approximate the correlated wavefunction $\psi(x_1, x_2, t)$ using the Kohn-Sham orbitals and to calculate the momentum distributions as for the Schrödinger solution.

5.5.1 Uncorrelated Functionals

Treating the Kohn-Sham orbitals as if they were one-electron wavefunctions yields a product wavefunction $\phi(x_1, t)\phi(x_2, t)$. This is the same assumption made to derive the uncorrelated ionization probability functionals (4.4).

The Fourier transformed Kohn-Sham orbital for $|x| > a$, i.e., with the bound states projected out (see Sec. 5.1) is

$$\phi^{(+)}(k, t) = (2\pi)^{-1/2} \int dx f(x) \phi(x, t) e^{-ikx}, \quad (5.7)$$

with $f(x) = (1 + e^{-c|x-a|})^{-1/2}$ the one-dimensional “smoothing” function equivalent to Eq. (5.2). Using the product wavefunction to calculate the momentum pair density (5.4) and the ion momentum density (5.6) gives the uncorrelated functional for the momentum pair density of the electrons freed in double ionization

$$\rho^{(2+)}(k_1, k_2, t) = 2 |\phi^{(+)}(k_1, t)\phi^{(+)}(k_2, t)|^2 \quad (5.8)$$

and the uncorrelated functional for the ion momentum density of He^{2+}

$$n_{\text{ion}}^{(2+)}(k_{\text{ion}}, t) = \int dk |\phi^{(+)}(-k_{\text{ion}} - k, t)\phi^{(+)}(k, t)|^2. \quad (5.9)$$

Equations (5.8) and (5.9) are not functionals of the density alone but due to the Fourier transformation of the Kohn-Sham orbital they are dependent on the density and on the phase of the Kohn-Sham orbital. This is in contrast to the uncorrelated ionization probability functionals (4.4) derived using the same (product wavefunction) assumption which are functionals only of the density.

The momentum pair density at $t = T$ as calculated from the uncorrelated functional (5.8) using the exact Kohn-Sham orbital is depicted in Fig. 5.3 for different intensities of the $\lambda = 780$ nm, $N = 3$ -cycle laser pulse. Comparison with Fig. 5.1, the momentum pair density calculated from the correlated Schrödinger wavefunction $\psi(x_1, x_2, T)$ using Eq. (5.4), confirms that only for the highest intensity a product wavefunction approach is feasible. For lower intensities the uncorrelated functional for the momentum pair density does not exhibit the typical “butterfly”-shaped correlation structures of the Schrödinger solution but instead the grid-like structure typical for a product wavefunction.

For the same system we calculate from Eq. (5.9) the ion momentum density using the exact Kohn-Sham orbital. In Fig. 5.4 the He^{2+} ion momentum density is

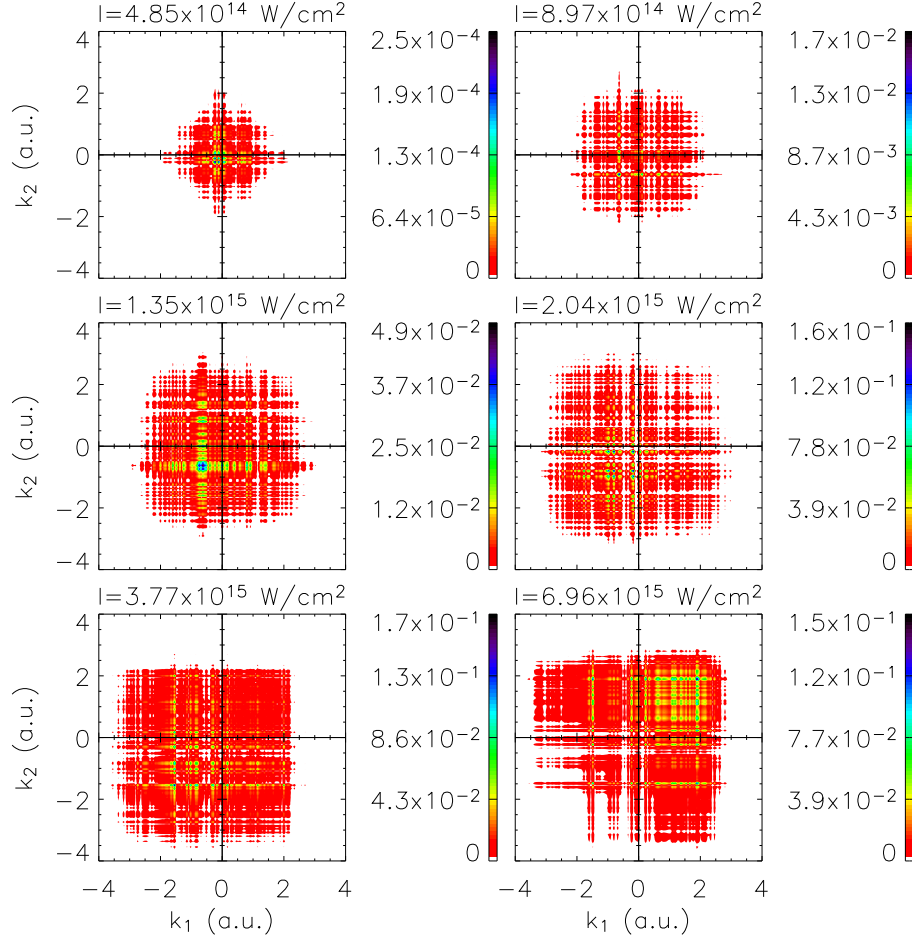


Figure 5.3: Contour plots of the momentum pair density of the electrons freed in double ionization at time $t = T$ as calculated from the uncorrelated functional (5.8) using the exact Kohn-Sham orbital. Results for different effective peak intensities of the $\lambda = 780$ nm, $N = 3$ -cycle laser pulse are shown.

compared to the results from the Schrödinger equation, which are scaled to enable the comparison of qualitative features. The different values of the integrals over the ion momentum density are due to the different double ionization probabilities as can be seen from $\int dk_{\text{Ion}} n_{\text{Ion}}^{(2+)}(k_{\text{Ion}}, t) \simeq P^{2+}$ (cf. Eq. (5.3)) which were discussed for the product wavefunction approach in Sec. 4.3.1. Apart from the highest intensity the density is centered around a central peak at $k_{\text{Ion}} \approx 0$, exhibiting only slightly positive values. This is evidence that correlations, which are not included in the uncorrelated functionals, are responsible for the distinct peaks of the ion momentum density at non-zero momenta. This result is consistent with the classical consideration (Sec. 5.3) and the analysis of the results of the time-dependent Schrödinger equation (Sec. 5.4.2) which attribute the peaks at $k_{\text{Ion}} \neq 0$ to electron rescatter-

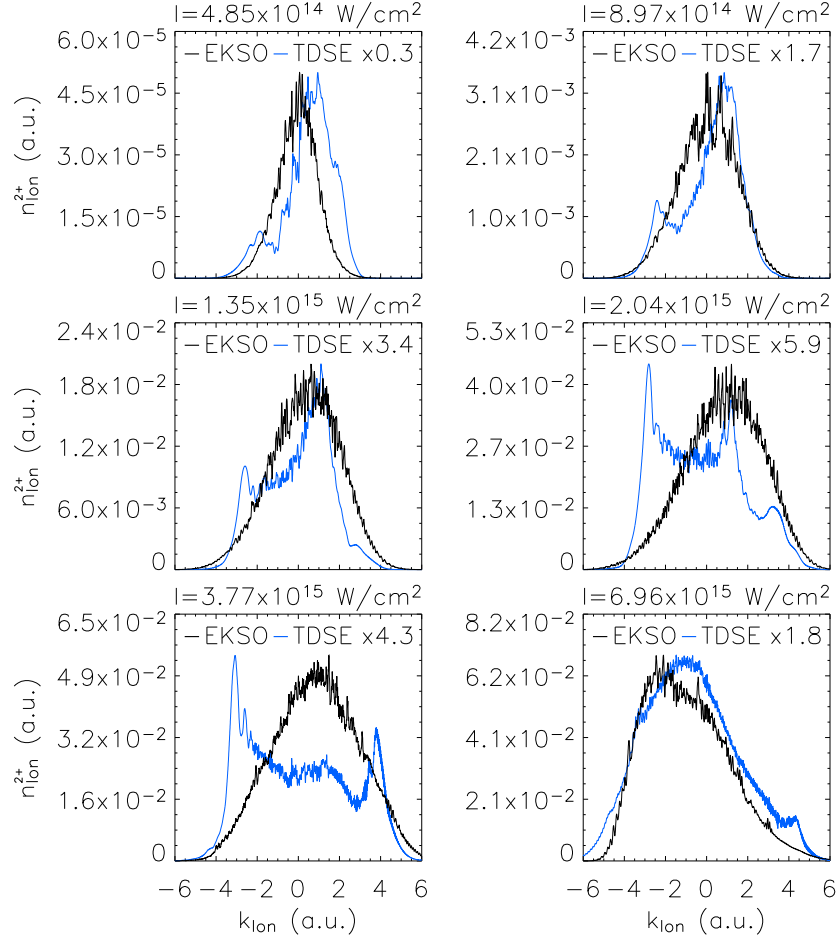


Figure 5.4: Ion momentum density of the model He^{2+} after interaction with the $\lambda = 780 \text{ nm}$, $N = 3$ -cycle laser pulse for different effective peak intensities. The density calculated using the exact Kohn-Sham orbital in the uncorrelated functional (EKS0) is compared to results from the Schrödinger solution (TDSE).

ing, i.e., to an interaction between the electrons. For the highest intensity shown in Fig. 5.4 sequential double ionization becomes dominant (cf. Sec. 5.4.2), so that the description using the exact Kohn-Sham orbital in the uncorrelated functional reproduces the ion momentum density well.

5.5.2 Comparison of Correlation Potentials

The uncorrelated functionals can be used as a measure for the quality of different approximations of the correlation potential v_c in the time-dependent Kohn-Sham equations, just as in the corresponding Sec. 4.3.2 for the ionization probability functionals. As it depends only on the orbitals and can be compared straightforwardly

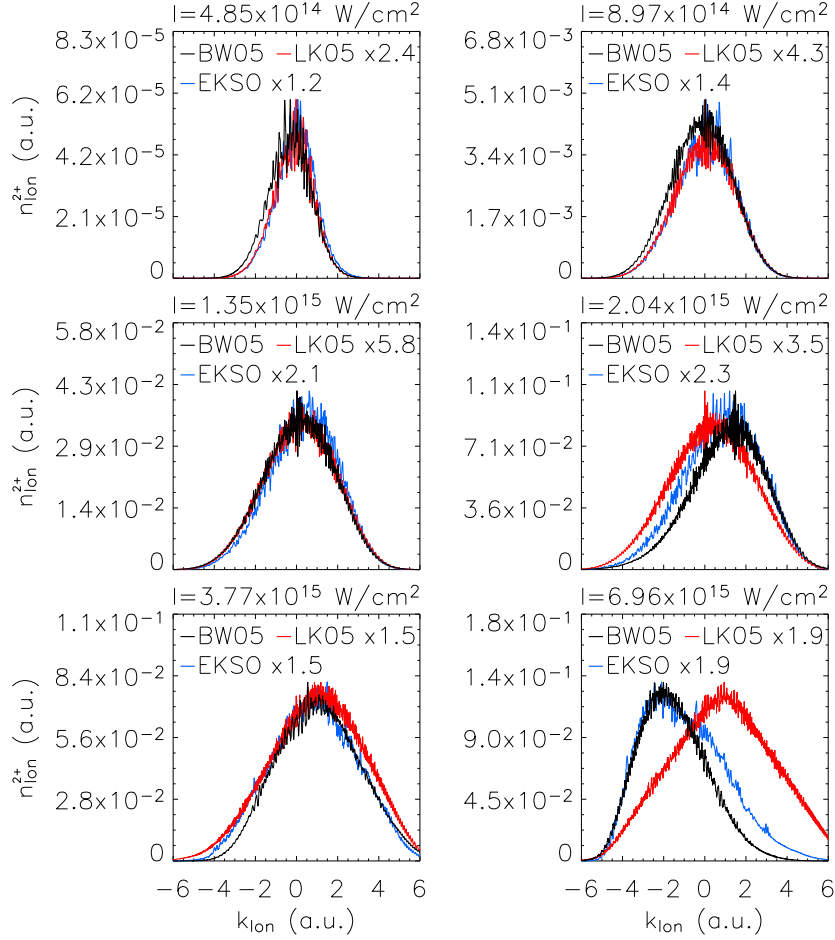


Figure 5.5: Ion momentum densities of He^{2+} at $t = T$ as calculated using BW05 and LK05 orbitals in the uncorrelated functional compared to results using the exact Kohn-Sham orbital (EKS0). Results for different effective peak intensities of the $\lambda = 780$ nm, $N = 3$ -cycle laser pulse are shown.

we evaluate the uncorrelated functional for the ion momentum density (5.9). In contrast to the functionals for the ionization probabilities (4.4) it depends on the phase of the orbital as well.

As discussed in Sec. 5.5.1 the integral over the ion momentum density will differ for different orbitals according to the double ionization probabilities for the respective intensity of the laser pulse (cf. Sec. 4.3.2). We will therefore restrict ourselves to the qualitative differences in the ion momentum distributions which (as shown in Sec. 5.4.2) reveal the process responsible for double ionization. The ion momentum densities after interaction with the $\lambda = 780$ nm, $N = 3$ -cycle laser pulse calculated according to Eqs. (5.9) are depicted in Fig. 5.5. In addition to the results obtained from the exact Kohn-Sham orbital (which is identical to the or-

bital a time-dependent Kohn-Sham equation with the exact v_c would yield) the ion momentum densities acquired from calculations with v_c^{LK05} (3.11) and v_c^{BW05} (3.12) are shown.

The results for $v_c = 0$ (TDHF) are not depicted as they are similar to the LK05 results, agreeing only slightly better with the EKSO results at the medium intensities shown in Fig. 5.5. Indeed, apart from the highest intensity all approximations of v_c yield uncorrelated ion momentum densities which are close the EKSO results (for the general deficiencies of the uncorrelated functional see the previous Sec. 5.5.1). Only at the highest intensity the BW05 approximation yields a considerably better agreement than the LK05 result which exhibits a single peak at $k_{\text{Ion}} \geq 0$ and not as the EKSO and BW05 solutions at $k_{\text{Ion}} \leq 0$. We attribute this to the fact that the BW05 potential, which uses $v_{\text{hxc}}(t) = v_{\text{hx}}(t_0) \Theta(N(t) - 1)$ should be better suited to describe purely sequential ionization, as the electron-electron interaction changes from the groundstate interaction to zero when the first electron leaves the atom. In addition, it does not include the nonlinear “feedback” of the density to v_{hx} inherent in the time-dependent $v_{\text{hx}}(t)$ used in the LK05 approximation. These results are thus in agreement with the findings of Sec. 5.4.2 that at $I = 6.96 \times 10^{15}$ W/cm² sequential double ionization dominates.

Therefore we can conclude that (except for sequential processes) the approximations of v_c are of comparable quality with respect to the ion momentum densities they yield. Due to the qualitative agreement with results for the exact Kohn-Sham orbital, there is no conclusive evidence that essential physical processes are not included in these approximations.

5.5.3 Towards Correlated Functionals

The uncorrelated functionals of Sec. 5.5.1 were shown to be insufficient to reproduce the results for the momentum pair density of the electrons freed in double ionization and for the ion momentum density of the solution of the time-dependent Schrödinger equation. Therefore we follow a route similar to the one employed to obtain the correlated ionization probability functionals in Sec. 4.3.3 in order to develop correlated functionals for the momentum distributions.

In polar representation the solution of the time-dependent Schrödinger equation is written as

$$\psi(x_1, x_2, t) = \sqrt{\rho(x_1, x_2, t)/2} e^{i\varphi(x_1, x_2, t)} \quad (5.10)$$

and the Kohn-Sham orbital as

$$\phi(x, t) = \sqrt{n(x, t)/2} e^{i\vartheta(x, t)}. \quad (5.11)$$

We then define a time-dependent complex exchange-correlation function

$$\begin{aligned} \kappa(x_1, x_2, t) &= \frac{\psi(x_1, x_2, t)}{\sqrt{2} \phi(x_1, t) \phi(x_2, t)} \\ &= \sqrt{g_{\text{xc}}(x_1, x_2, t)} e^{i[\varphi(x_1, x_2, t) - \vartheta(x_1, t) - \vartheta(x_2, t)]}. \end{aligned} \quad (5.12)$$

The exchange-correlation function is given by (cf. Sec.4.3.3) $g_{xc}(x_1, x_2, t) = \rho(x_1, x_2, t) / n(x_1, t) n(x_2, t)$ and thus $|\kappa(x_1, x_2, t)|^2 = g_{xc}(x_1, x_2, t)$. Note that while g_{xc} is an observable and thus a functional only of the density exists, κ is not an observable. Using Eq. (5.12) to express the correlated wavefunction $\psi(x_1, x_2, t)$ in terms of the Kohn-Sham orbitals and the complex exchange-correlation function, Eq. (5.4) gives the correlated functional for the momentum pair density of the electrons freed in double ionization

$$\rho^{(2+)}(k_1, k_2, t) = \pi^{-2} \left| \int dx_1 \int dx_2 \phi^{(+)}(x_1, t) \phi^{(+)}(x_2, t) \times \kappa(x_1, x_2, t) e^{-i(k_1 x_1 + k_2 x_2)} \right|^2, \quad (5.13)$$

with $\phi^{(+)}(x, t) = f(x) \phi(x, t)$. The correlated ion momentum density is calculated by using the correlated momentum pair density in Eq. (5.6). We thus have exact momentum distribution functionals which depend only on the complex exchange-correlation function κ and the Kohn-Sham orbital.

The complex exchange-correlation function κ in turn depends on the pair density and the phase of the Schrödinger solution $\psi(x_1, x_2, t)$. In order to derive momentum space properties for more complex atoms than Helium from the Kohn-Sham orbitals directly through expressions like Eq. (5.13) it is therefore inevitable to approximate κ . However this is challenging since unlike for the ionization probabilities (cf. Sec.4.3.3) due to the integrals from the Fourier transformation in Eq. (5.13) the complex exchange-correlation function has to be approximated for all points in $\mathcal{A}(\text{He}^{2+})$ and not just for the bound electrons in $\mathcal{A}(\text{He})$ (cf. Sec.4.1).

5.5.4 Product Phase Approximation

The necessary approximation of the complex exchange-correlation function κ (5.12) consists of approximating $g_{xc}(x_1, x_2, t)$ and the phase-difference $\varphi(x_1, x_2, t) - \vartheta(x_1, t) - \vartheta(x_2, t)$.

Addressing the second part, the easiest approximation is to assume that the difference of the sum of the phases of the Kohn-Sham orbitals and the phase of the correlated wavefunction can be neglected when calculating momentum distributions, i.e., we set

$$\varphi(x_1, x_2, t) = \vartheta(x_1, t) + \vartheta(x_2, t). \quad (5.14)$$

Since the phase $\vartheta(x, t)$ can be constructed from $\psi(x_1, x_2, t)$ as the phase of the exact Kohn-Sham orbital (cf. Eqs. (3.17)) we denote this approach as the “product phase” approximation (PP), which yields

$$\kappa^{\text{PP}}(x_1, x_2, t) \simeq \sqrt{g_{xc}(x_1, x_2, t)}. \quad (5.15)$$

It is noteworthy that with the knowledge of the exact κ^{PP} it is possible to calculate the exact double ionization probabilities from the exact Kohn-Sham orbital (cf. Sec.4.3.3).

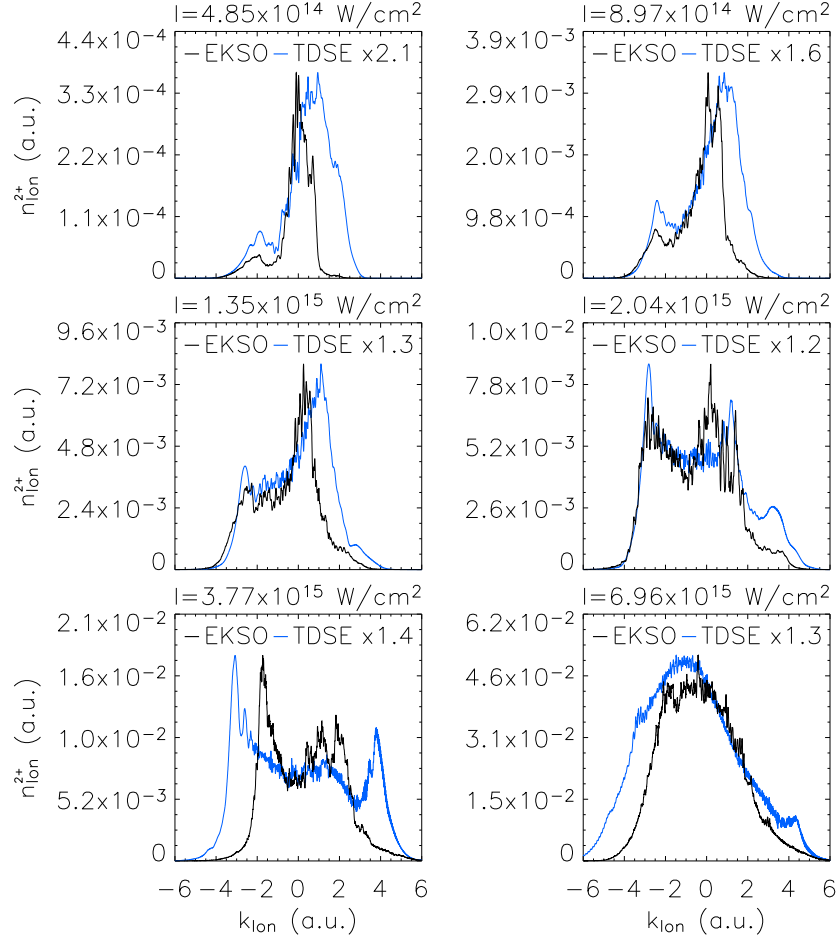


Figure 5.6: Ion momentum density of He^{2+} calculated from the correlated functionals in the product phase approximation using the exact Kohn-Sham orbital (EKSO). Results for different effective peak intensities of the $\lambda = 780$ nm, $N = 3$ -cycle laser pulse are compared to results obtained from the time-dependent Schrödinger equation.

We calculate the ion momentum density using Eq. (5.15) in Eq. (5.13) and in Eq. (5.6). Employing the exact Kohn-Sham orbital, the ion momentum densities shown in Fig. 5.6 for different intensities of the $\lambda = 780$ nm, $N = 3$ -cycle laser pulse are obtained. For comparison of the qualitative features the results from the Schrödinger solution are scaled, although the integrals over the ion momentum densities are equal in both cases (cf. discussion in Sec. 5.5.1) since the product phase approximation returns the exact double ionization probabilities. A generally good qualitative agreement with the Schrödinger solution is acquired. The asymmetric structure and the distinct peaks are reproduced. For intensities where non-sequential double ionization is strongest the quantitative agreement is least

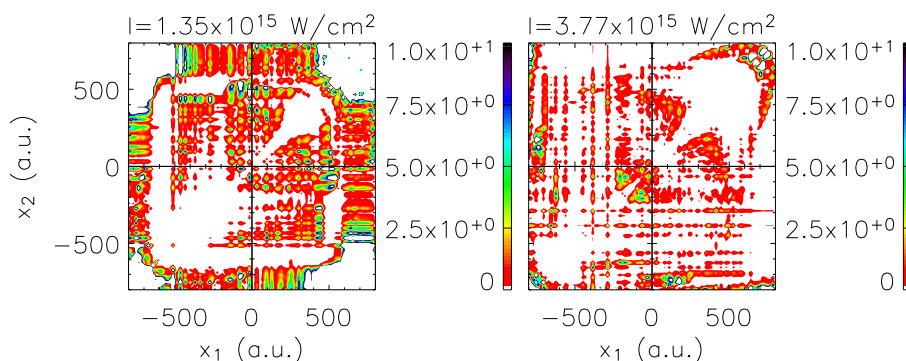


Figure 5.7: Contour plots of the exchange-correlation function $g_{xc}(x_1, x_2, t)$ for two effective peak intensities of the $\lambda = 780$ nm, $N = 3$ -cycle laser pulse as acquired from the solution of the time-dependent Schrödinger equation. For clarity values larger than 10 are shown as 10.

convincing. Although the product phase approximation does not reproduce the exact k_{ion} values of the peaks it modifies the uncorrelated functionals in a way which allows to deduce information about the underlying double ionization processes at the different intensities. We can therefore conclude that the difference between the phase of the correlated wavefunction and a product wavefunction is not as important for reproducing the structure of the ion momentum density as is the correlation given by $g_{xc}(x_1, x_2, t)$. This conclusion is verified by setting $g_{xc} = 1$ in Eq. (5.12) and using the exact phases in Eq. (5.13), which does not yield the peaks present in the Schrödinger solution. Using LK05 orbitals in the product phase approximation also reproduces distinct peaks while general agreement with the Schrödinger ion momentum density is not as good as for the EKSO orbitals.

The contour plots of the momentum pair density of the electrons freed in double ionization $\rho^{(2+)}(k_1, k_2, t)$ calculated from the correlated functional in the product phase approximation using the exact Kohn-Sham orbital show a correlated structure. However, they clearly differ from the momentum pair densities acquired from the Schrödinger solution (Fig. 5.1).

Using the product phase approximation we obtain momentum distributions which yield insight into the double ionization processes. However, this still requires knowledge of the exact $g_{xc}(x_1, x_2, t)$ at time $t = T$ after the laser pulse, i.e., of the exact pair density in real space. As pointed out above, approximating $g_{xc}(x_1, x_2, t)$ is a formidable task, as can also be seen from the highly correlated structure in Fig. 5.7, where contour plots of the exchange-correlation function $g_{xc}(x_1, x_2, T)$ are shown for intensities where non-sequential double ionization dominates. An adiabatic approximation (cf. Sec. 4.3.7) using the groundstate pair density is not feasible as effectively only the exchange-correlation function in $\mathcal{A}(\text{He}^{2+})$ is used in Eq. (5.13). An expansion for small inter-electron distances (cf. Sec. 4.3.6) will not include the correlations for large $|x_1 - x_2|$, which are clearly present in Fig. 5.7. Multiplying the complex exchange-correlation function by a damping

function $F(|x_1 - x_2|)$ with $F \rightarrow 0$ for large $|x_1 - x_2|$, we verified that short-range correlations in the final wavefunction alone will not reveal the characteristic peaks in the ion momentum density.

It will therefore be of central importance to devise either a new way of approximating $g_{xc}(x_1, x_2, t)$ or of treating correlations in momentum space, i.e., defining $g_{xc}^{(2+)}(k_1, k_2, t) = \rho^{(2+)}(k_1, k_2, t) / n^{(2+)}(k_1, t) n^{(2+)}(k_2, t)$. Comparing Figs. 5.1 and 5.8 however, it is reasonable to assume that this approach will be facing the same problems as the approximation of the exchange-correlation function in real space. Hence, it seems worth studying the feasibility of approaches including memory effects.

Chapter 6

Non-Sequential Double Recombination

An atom interacting with a laser field can be ionized (cf. Chapters 4 and 5 for the different ionization processes). As explained in the introduction (Chapter 1) the dislodged electron can return to the ion at a later instant in time and recombine into a bound state. In high-order harmonic generation (HOHG) it emits a single photon of frequency Ω which is a multiple of the frequency of the laser field ω . We discovered a related process, non-sequential double recombination (NSDR) [61]: Two electrons are freed sequentially and recombine at the same time, emitting a single photon. Using a classical model the cutoff-law of high-order harmonic generation is reproduced and a new cutoff-law for non-sequential double recombination is found (Sec. 6.1). In Sec. 6.2 the calculation of high-order harmonic spectra is introduced. The solution of the time-dependent Schrödinger equation reveals a second plateau in the harmonic spectra due to non-sequential double recombination. The results corroborate the underlying process as derived from the classical model (Sec. 6.3). As the functional of the density for high-order harmonic spectra is known, the existence of the second plateau provides a crucial test for the quality of densities from time-dependent density functional calculations. We find that the approximations of v_c used in this work produce a second plateau. However, the plateau is too high as compared to the first plateau, and it does not exhibit the cutoff associated with non-sequential double recombination (Sec. 6.4).

6.1 Classical Model

Non-sequential double recombination is introduced using a classical model which facilitates the interpretation of results from the time-dependent Schrödinger equation. The model is, due to its simplicity, also known as the “simple man’s theory” (cf. the review Ref. [62]) and was also used as the basis for the classical considerations concerning the ion momentum density in Sec. 5.3.

We are interested in the dynamics of an electron in a linearly polarized laser field $A(t) = \hat{A} A_E(t) \sin(\omega t)$ with a period of one laser cycle $T_{\text{cyc}} = 2\pi/\omega$ and an envelope function $A_E(t)$. Describing the laser field in dipole approximation the classical electron dynamics are confined to the direction of the polarization of the laser field (cf. Secs. 3.1 and 3.2). An electron leaves the atom with zero initial velocity at time t^e in the electric field $E(t) = -\partial_t A(t)$. Subsequently the electron is assumed to move freely in the laser field with the momentum

$$p(t) = A(t) - A(t^e). \quad (6.1)$$

The position is then found by integration as

$$x(t) = \alpha(t) - \alpha(t^e) - A(t^e)(t - t^e), \quad (6.2)$$

with $\alpha(t) = \int^t dt' A(t')$ the excursion of the free electron in the field. From Eq. (6.1) the kinetic energy of the electron at time t follows as $p^2(t)/2$.

If $x(t^r) = 0$ for some time $t^r > t^e$ the free electron revisits the ion and recombination ensuing the generation of high-order harmonic radiation is possible. The energy of the emitted photon Ω is given by the sum of the kinetic energy of the electron and the ionization potential

$$\Omega = \frac{1}{2} p^2(t^r) + I_p^{(1)}. \quad (6.3)$$

The maximum photon energy is then found from $\max_{t^r} \{p^2(t^r)/2 + I_p^{(1)} \mid x(t^r) = 0\}$ and yields the well-known cutoff-law for the generation of high-order harmonics in an infinitely long laser pulse ($A_E(t) = 1$) [15]

$$\Omega_{\text{max}(1)} = 3.17 U_p + I_p^{(1)} \quad (6.4)$$

with the ponderomotive potential $U_p = \hat{A}^2/4$.

In the lower part of Fig. 6.1 photon energies Ω as multiples of the laser frequency ω are shown for an infinitely long laser pulse with $\hat{A} = 3.359$ interacting with a one-dimensional Helium atom. It is found that the maximum energy (6.4) is emitted if the electron recombines in the half-cycle of the laser pulse following its emission.

We extend this model by regarding two electrons moving freely and without interaction (i.e., double ionization is considered to be sequential, cf. Sec. 5.3). They are dislodged at times t_1^e and t_2^e with $t_1^e < t_2^e$. The emission of the two electrons has to take place in different half-cycles of the laser pulse. Otherwise the electrons would follow similar classical trajectories, a scenario which due to Coulomb repulsion makes recombination at the same time extremely unlikely. Due to the same reasoning the second electron may not be freed exactly one half-cycle after the first. Allowing for multiple returns, the condition for non-sequential double recombination, i.e., simultaneous recombination of the electrons is $x_1(t^r) = 0$ and $x_2(t^r) = 0$ with the corresponding energy of the single photon being emitted

$$\Omega = \frac{1}{2} p_1^2(t^r) + \frac{1}{2} p_2^2(t^r) + I_p^{(1)} + I_p^{(2)}. \quad (6.5)$$

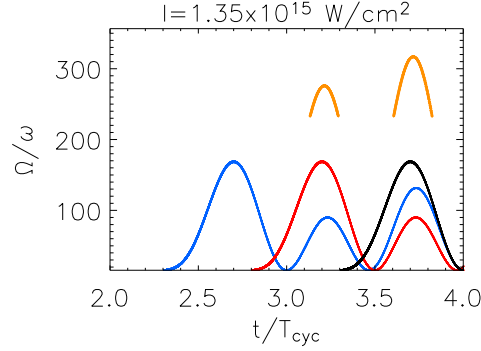


Figure 6.1: Energies of emitted photons in multiples of the laser frequency for a selected time-interval of an infinitely long sin-pulse interacting with a one-dimensional Helium atom. Only electrons emitted for $2 \leq t^e/T_{\text{cyc}} < 2.5$ (blue), $2.5 \leq t^e/T_{\text{cyc}} < 3.0$ (red) and $3.0 \leq t^e/T_{\text{cyc}} < 3.5$ (black) are shown. The highest energies of photons emitted in non-sequential double recombination are depicted in orange, where the left peak follows from the sum of the blue and red curves (electrons emitted in subsequent half-cycles) and the right peak of the blue and black curves (electrons emitted with one half-cycle difference).

Searching again for the maximum photon energy we find

$$\Omega_{\text{max}(2)} = 5.55 U_p + I_p^{(1)} + I_p^{(2)}, \quad (6.6)$$

a new cutoff-law for non-sequential double recombination. This is the highest energy possible when electrons are freed in next but one half cycles. If the electrons leave the atom in subsequent half-cycles the maximum energy is only $\Omega_{\text{max}(2')} = 4.70 U_p + I_p^{(1)} + I_p^{(2)}$. The cutoffs correspond to the maximum values of the peaks in the upper part of Fig. 6.1 for the infinitely long laser pulse.

For few-cycle pulses the cutoff laws (6.4), (6.6) yield different numerical prefactors as the peak value of $A(t)$ is not equal to \hat{A} and differs throughout the pulse due to the influence of the envelope function $A_E(t)$ (Sec. 3.1).

6.2 Calculation of High-Order Harmonic Spectra

It is known that the single atom-response is a basic ingredient for comparison with experimental high-order harmonic spectra [63]. We will therefore consider only the radiation emitted by a single atom. Classically, the power of the radiation emitted by a dipole is proportional to the square of the acceleration $P(t) \propto |d_t^2 x(t)|^2$. In a semi-classical approach we replace x by the dipole operator and write $\langle a(t) \rangle = d_t^2 \langle \sum_{i=1}^2 x_i \rangle = \sum_{i=1}^2 d_t^2 \langle x_i \rangle$. A fully quantum mechanical treatment leads in the case of a dilute gas to the same expression and confirms the validity of treating only a single atom [64]. From Ehrenfest's theorem follows with the kinetic momentum

operator $\widehat{p}_i^{\text{kin}} = -i\partial_{x_i} + A(t)$ and the Hamiltonian of the model Helium atom (3.5)

$$\begin{aligned} d_t^2 \langle x_i \rangle &= d_t \langle -i\partial_{x_i} + A(t) \rangle = \langle i[\widehat{H}(x_1, x_2, t), -i\partial_{x_i}] + \partial_t A(t) \rangle \\ &= \langle -\partial_{x_i} [V(x_1) + V(x_2) + W(|x_1 - x_2|)] - E(t) \rangle. \end{aligned} \quad (6.7)$$

In the last step we used $E(t) = -\partial_t A(t)$. With $V(x)$ given by Eq. (3.3) we have $\langle \partial_{x_1} V(x_1) \rangle = \langle \partial_{x_2} V(x_2) \rangle$ and $\partial_{x_1} W(|x_1 - x_2|) = -\partial_{x_2} W(|x_1 - x_2|)$. Hence, $\langle a(t) \rangle = 2 \langle -\partial_x V(x) - E(t) \rangle$ which we can write as [65]

$$\langle a(t) \rangle = \int dx n(x, t) \left[\frac{x}{(x^2 + \epsilon_{\text{en}})^{3/2}} - E(t) \right], \quad (6.8)$$

with the density of the system $n(x, t) = 2 \int dx_2 |\psi(x_1, x_2, t)|^2$ (3.13). The power is then $P(t) \propto |\langle a(t) \rangle|^2$. As we are interested in an analysis of the spectrum of the emitted radiation we introduce the Fourier transform of $\langle a(t) \rangle$, the complex valued acceleration as a function of the frequency of the emitted photons Ω

$$a(\Omega) = \left(\sqrt{2\pi} \right)^{-1} \int dt \langle a(t) \rangle e^{-i\Omega t}. \quad (6.9)$$

From the total emitted energy $E = \int dt P(t) = \int d\Omega \varepsilon(\Omega)$ we see that for the energy emitted into a spectral interval $[\Omega, \Omega + d\Omega]$,

$$\varepsilon(\Omega) d\Omega \propto |a(\Omega)|^2 d\Omega, \quad (6.10)$$

so that $|a(\Omega)|^2$ yields information about the spectral distribution of the emitted radiation. The selection rule for the emission of harmonic radiation for a single atom in an infinite pulse is that only odd multiples of the laser frequency ω are emitted. This follows from the symmetry of the respective matrix element.

Inverse Fourier transformation of the acceleration as a function of the frequency $a(\Omega)$ (6.9) simply reproduces the acceleration as a function of time t . We multiply the acceleration by a window function

$$W(\Omega'; \Omega) = \frac{1}{2} \left[1 + \cos \left(2\pi \frac{\Omega - \Omega'}{w} \right) \Theta \left(\frac{w}{2} - |\Omega - \Omega'| \right) \right], \quad (6.11)$$

which “selects” via the stepfunction a frequency range of total width $w = 40\omega$ centered around Ω . Fourier transforming back to the time-domain yields the emission times for the harmonics of the respective frequency

$$a(\Omega, t) = \left(\sqrt{2\pi} \right)^{-1} \int d\Omega' a(\Omega') W(\Omega', \Omega) e^{i\Omega' t}. \quad (6.12)$$

As the emission times of the harmonic radiation correspond to the recombination times of the electrons, $|a(\Omega, t)|^2$ allows to retrieve the classical return energies as a function of time (the corresponding energies of the emitted photons are shown in Fig. 6.1) from a quantum mechanical calculation.

In actual calculations we implement Eqs. (6.9) and (6.12) by a fast Fourier transformation algorithm using the discrete time-series $\langle a(i \Delta t) \rangle$ with $0 \leq i \Delta t \leq T$ and $i = 0, \dots, N_t$. For the Fourier transformation the data set is multiplied by a Hanning window $W(t) = [1 - \cos(2\pi t/T)]/2$ to reduce aliasing effects. The prefactors in the fast Fourier transformation are chosen to ensure that Parseval's theorem holds with respect to integrations approximated by a Riemann sum.

6.3 High-Order Harmonic Spectra from the TDSE

In order to verify the existence of non-sequential double recombination we solve the time-dependent Schrödinger equation of the model Helium atom (Sec. 3.3) for different effective peak intensities of the $\lambda = 780$ nm, $N = 6$ cycle laser pulse. As described in the previous Sec. 6.2 we determine $|a(\Omega)|^2$ (6.9) and $|a(\Omega, t)|^2$ (6.12).

To complement our analysis, a single-active electron calculation using the model introduced in Sec. 3.7 is performed. As one electron is assumed to remain in the groundstate we consider only the active electron and modify Eq. (6.9) accordingly. As can be seen from Eqs. (3.5) and (3.18) solving the time-dependent Schrödinger equation with the electron-electron interaction set to zero ($W(|x_1 - x_2|) = 0$) corresponds to solving two model He^+ ions. In this section we used this approach to obtain the results for He^+ .

In Fig. 6.2 spectra of the emitted radiation as functions of multiples of the laser frequency are shown for different intensities of the laser pulse. In the results obtained from the time-dependent Schrödinger equation the nearly constant plateau typical of high-order harmonic generation is clearly discernible, including the cutoff at $3.17 U_p + I_p^{(1)}$ which is indicated by arrow 1. The height of the first plateau is $|a(\Omega)|^2 \approx (10^{-3} - 10^{-4})$. In addition, a second plateau at higher multiples of the laser frequency Ω/ω can be readily identified with a height of $(10^{-11} - 10^{-12})$ of the first plateau. An estimate of the efficiency of non-sequential double recombination is given by the product of the heights of the He single-active electron and the He^+ plateaus. From Fig. 6.2 we hence deduce that the Coulomb interaction between the electrons does not reduce the height of the second plateau any further. The cutoff of the second plateau is in excellent agreement with the value expected from the classical model (Sec. 6.1) of $5.55 U_p + I_p^{(1)} + I_p^{(2)}$ (arrow 4). The arrow 3 in Fig. 6.2 indicates the value $4.70 U_p + I_p^{(1)} + I_p^{(2)}$. For values of Ω/ω beyond arrow 3 only two classical (and corresponding quantum) trajectories contribute (cf. Fig. 6.3). This leads to a less jagged spectrum, an effect best seen for the two highest intensities.

The single-active electron results reproduce the first plateau including the cutoff (arrow 1) very precisely. This confirms the well-established view that high-order harmonic generation (for the first plateau) is essentially a single electron effect. Furthermore, the fact that no second plateau is produced furthers the view of non-sequential double recombination as a distinct two-electron process. This is also underlined by the He^+ spectra, where no second plateau is observed. As they were calculated from the time-dependent Schrödinger equation for the model Helium

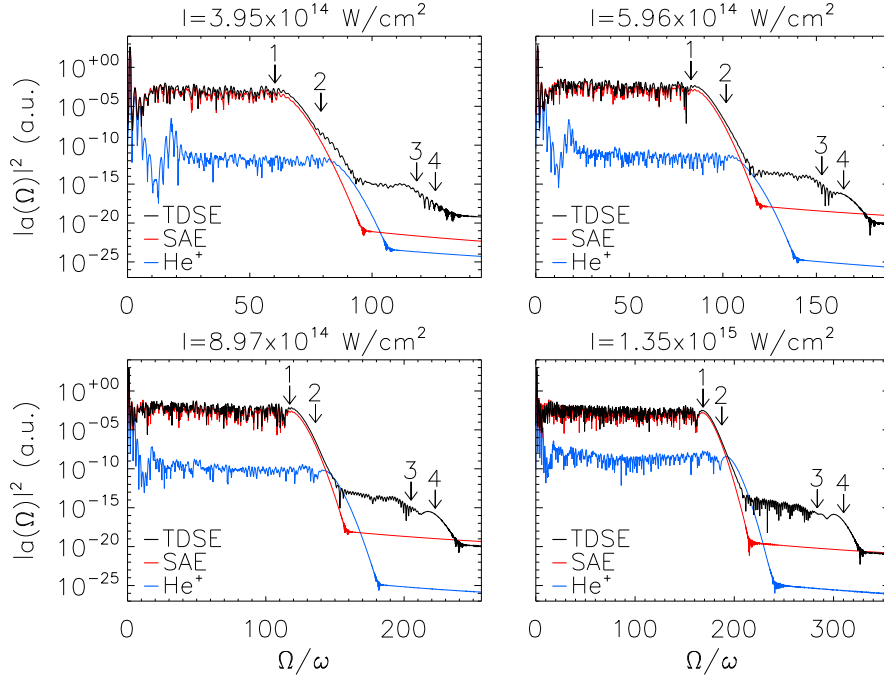


Figure 6.2: High-order harmonic spectra of the model Helium atom calculated from the time-dependent Schrödinger equation (TDSE) compared to the single-active electron (SAE) and the He^+ spectra. The $\lambda = 780$ nm, $N = 6$ -cycle laser pulse was used with different effective peak intensities.

atom with $W(|x_1 - x_2|) = 0$ (cf. above), we have thus confirmed that electron-electron interaction is necessary to produce the second plateau. The first plateau for He^+ is markedly lower than for Helium due to the higher ionization potential. The He^+ cutoff $3.17U_p + I_p^{(2)}$ is indicated by arrow 2. We attribute the enhanced values for $|a(\Omega)|^2$ at $\Omega/\omega \approx 20$ to bound-bound transitions in He^+ .

For the four intensities in Fig. 6.2 the corresponding contour plots of $|a(\Omega, t)|^2$ (6.12) are depicted in Fig. 6.3. In addition, the photon energies of the solutions of the classical model for the $N = 6$ cycle pulse are superimposed as white lines (note that the photon energies depicted in Fig. 6.1 are for an infinitely long pulse). The highest classically possible photon energies of non-sequential double recombination in the time-interval of interest are drawn in black. The agreement with the frequency-time analysis of the time-dependent Schrödinger equation is further evidence that the second plateau is caused by non-sequential double recombination.

The efficiency of high-order harmonic generation in the range of the first plateau has been shown to be overestimated by a one-dimensional as compared to a three-dimensional calculation [66]. The spreading of the wavepacket of the free electrons depends on the dimensionality of the system d . Calculations with the strong-field approximation in full dimensionality confirm that the height of the first plateau scales with ω^d while the second plateau scales with ω^{2d} , where ω is the frequency

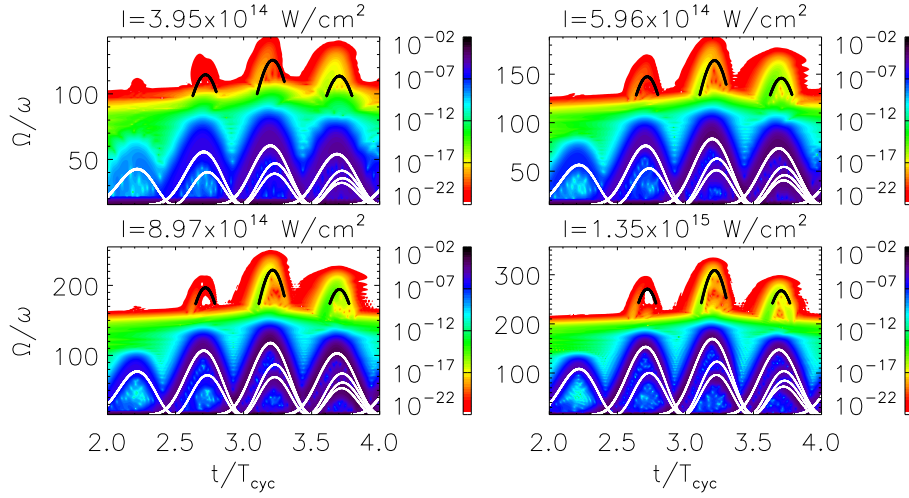


Figure 6.3: Frequency-time analysis of the emission of high-order harmonic radiation as calculated from the solution of the time-dependent Schrödinger equation. Contour plots of $|a(\Omega, t)|^2$ are compared to photon energies from the classical model (cf. Sec. 6.1) which are drawn in white and black for a selected time-interval of the $\lambda = 780$ nm, $N = 6$ -cycle laser pulse. Calculations for different effective peak intensities are shown.

of the laser [61]. The height of the second plateau will therefore be markedly lower in a real three dimensional system. The efficiency of the second plateau as compared to the first plateau thus renders an experimental observation of non-sequential double recombination difficult. From the frequency-time analysis and the classical model we know, however, which ionization times of the electrons will lead to non-sequential double recombination. It is therefore reasonable to assume that controlling the ionization times will enhance the height of the second plateau relative to the height of the first plateau.

Ionization of the atom at specific times is achieved by using laser pulses with ultraviolet wavelengths (see, e.g., Ref. [67]). We use two laser pulses $i \in \{1, 2\}$ centered around the desired ionization time t_i with

$$A_i(t) = \hat{A}_i e^{-\Gamma(t-t_i)^2} \sin(\omega_i(t-t_i)), \quad (6.13)$$

for $0 \leq t \leq T$, where T is the length of the original laser pulse. A Gaussian envelope function is chosen to minimize the influence of the ultraviolet pulses on the Fourier transformation (using a \cos^2 -envelope produces a signal partly masking the second plateau as would markedly shorter pulses). The parameter $\Gamma = 0.4$ ensures that both pulses have a “full width at half maximum” (FWHM) comparable to respective three- and six-cycle \cos^2 -pulses. In order for the electrons to leave the atom with vanishing initial velocity (as in the classical calculations of Sec. 6.1), i.e., zero initial kinetic energy, the frequencies are chosen corresponding to the ionization potentials $\omega_1 = I_p^{(1)} = 0.904$ and $\omega_2 = I_p^{(2)} = 2.0$. As the probability for tunnel ionization

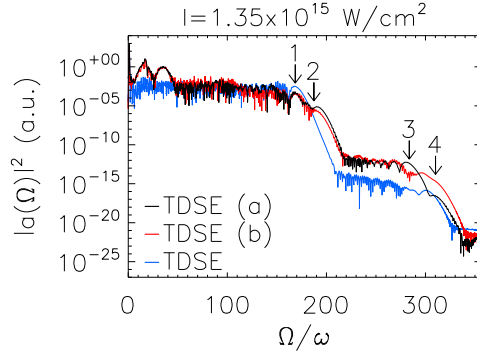


Figure 6.4: High-order harmonic spectrum calculated from the time-dependent Schrödinger equation of the model Helium atom. Results of the interaction with the $\lambda=780$ nm, $N=6$ -cycle laser pulse (TDSE) are compared to additional exposure to combinations of two ultraviolet laser pulses with (a) $t_1 = 2.01 T_{\text{cyc}}$ and (b) $t_1 = 1.52 T_{\text{cyc}}$.

is proportional to the intensity of the laser field which in turn is proportional to \hat{A}_i/ω_i we use $\hat{A}_2 = \omega_1 \hat{A}_1/\omega_2$. For the results presented here we choose $\hat{A}_1 = 0.35$. The ultraviolet pulses are added to the vector potential $A(t)$ of the $\lambda = 780$ nm, $N = 6$ -cycle laser pulse in the expression for the external potential $V(x, t)$ (3.6): $A(t) \rightarrow A(t) + A_1(t) + A_2(t)$.

With $T_{\text{cyc}} = 2\pi/\omega$ we employ two different combinations of two ultraviolet pulses with ionization times of (a) $t_1 = 2.01 T_{\text{cyc}}$ as well as (b) $t_1 = 1.52 T_{\text{cyc}}$ and $t_2 = 2.54 T_{\text{cyc}}$. This initiates “trajectories” contributing to non-sequential double recombination up to the cutoffs indicated by arrows 3 and 4, respectively. Comparing the resulting spectrum for a selected intensity in Fig. 6.4 with the corresponding spectrum without the ultraviolet laser pulses, we observe that the general structure of the first plateau is unchanged. The only marked differences are found at $\omega_1/\omega = 15.5$ and at $\omega_2/\omega = 34.2$ which can thus be identified as absorption of two ultraviolet photons and recombination. Furthermore, the He^+ cutoff is more pronounced as the enhanced ionization by the first ultraviolet pulse increases the probability to produce He^+ which will subsequently contribute to high-order harmonic generation. The second plateau meanwhile is enhanced by a factor of about 10^3 . As expected from the classical prediction the pulse combination (a) magnifies only the plateau up to $4.70 U_p + I_p^{(1)} + I_p^{(2)}$ (arrow 3). Only recombination of electrons leaving the atom in consecutive half-cycles of the laser pulse is enhanced. If instead for pulse combination (b) electrons are preferentially emitted in next but one half-cycles, the whole second plateau up to $5.55 U_p + I_p^{(1)} + I_p^{(2)}$ (arrow 4) is amplified, another clear indication that non-sequential double recombination proceeds as explained by the classical model.

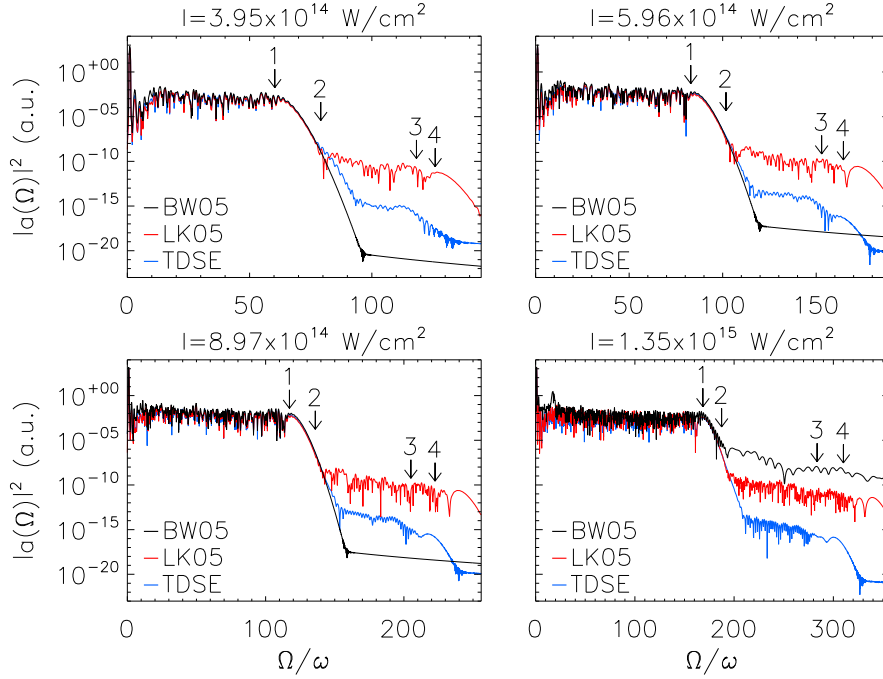


Figure 6.5: High-order harmonic spectra of the model Helium atom calculated from the densities produced by the BW05 and LK05 approximations of v_c compared to the results of the time-dependent Schrödinger equation. Spectra for different effective peak intensities of the $\lambda=780$ nm, $N=6$ -cycle laser pulse are shown.

6.4 High-Order Harmonic Spectra from TDDFT

In Sec. 6.2 we obtained an expression for the calculation of the expectation value of the acceleration $\langle a(t) \rangle$ (6.8) which depends on the density only. $\langle a(t) \rangle$ allows to calculate via Eq. (6.9) the high-order harmonic spectrum. We thus have an observable were the functional of the density is known exactly (as opposed to the ionization probabilities in Sec. 4.3 and the momentum distributions in Sec. 5.5). Potential disagreements between time-dependent density functional calculations and the exact results are thus solely due to differences in the densities. The high-order harmonic spectra now offer the possibility to compare the results of $|a(\Omega)|^2$ using densities calculated with different v_c directly to the results of the time-dependent Schrödinger equation presented in Sec. 6.3. We observe that as the density of the exact Kohn-Sham orbital is by construction equal to the density of the Schrödinger solution, it yields exactly the same spectra.

In Fig. 6.5 we compare values of $|a(\Omega)|^2$ for the LK05 (3.11) and BW05 (3.12) approximations of v_c to the high-order harmonic spectra calculated from the solution of the time-dependent Schrödinger equation. For both approximations the agreement with the exact result is very good in the range of the first plateau. The

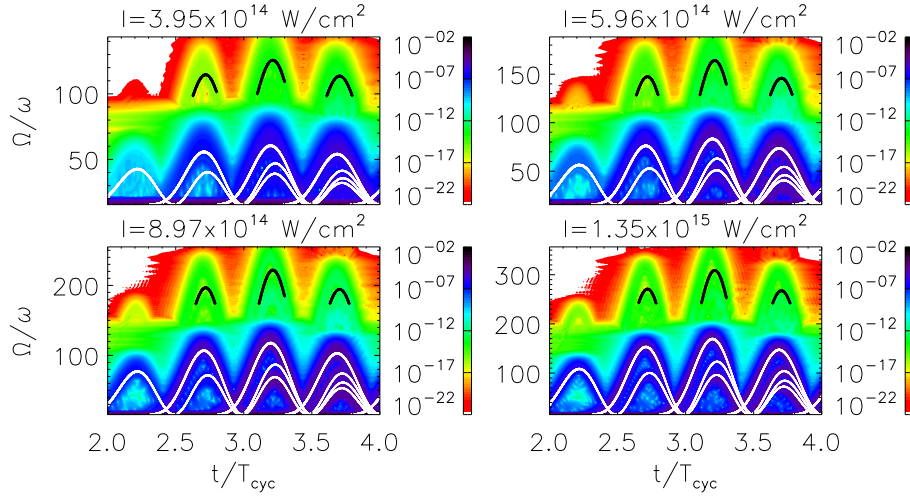


Figure 6.6: Frequency-time analysis of the emission of high-order harmonic radiation as calculated from a time-dependent density functional calculation with v_c^{LK05} . Contour plots of $|a(\Omega, t)|^2$ are compared to photon energies from the classical model (cf. Sec. 6.1) which are drawn in white and black for a selected time-interval of the $\lambda = 780$ nm, $N = 6$ -cycle laser pulse. Calculations for different effective peak intensities are shown.

high-order harmonic cutoff (6.4) indicated by arrow 1 is precisely reproduced and the structure of the spectrum is even quantitatively very similar to the Schrödinger results. For v_c^{BW05} the number of bound electrons $N(t)$ becomes smaller than one during the interaction with the laser pulse at the highest depicted intensity. Subsequently $v_{\text{hxc}}^{\text{BW05}}(t) = v_{\text{hx}}(t_0) \rightarrow v_{\text{hxc}}^{\text{BW05}}(t) = 0$ (cf. Eq. (3.12)), inducing a sudden change in the ionization potential enabling “transitions” of the remaining bound electron. This behavior leads to resonances at $\Omega/\omega \approx 20$ as in the case of the He^+ ion (cf. Fig. 6.2). Results for a calculation with $v_c = 0$ (TDHF) are quantitatively very similar to the LK05 results and therefore not presented here.

In the range of the second plateau we do not observe agreement with the time-dependent Schrödinger solution. Using v_c^{LK05} a second plateau is produced which is, however, by a factor of about 10^5 too high. Additionally, the second cutoff is not located at the position for the non-sequential double recombination cutoff predicted by the classical model (6.6) and verified by the Schrödinger solution. Instead it is located at $2(3.17U_p + I_p^{(1)})$, i.e., two times the value of the cutoff of the first plateau. In a calculation with $v_c = 0$ (TDHF) we observe a similar behavior. This evidences that the dominant effect contributing to the second plateau in a calculation using v_c^{LK05} and $v_c = 0$ is not non-sequential double recombination. Instead we attribute this effect to the nonlinearity included in the Hartree-exchange potential $v_{\text{hx}}(x, t)$ (3.8) as the density is used to calculate the effective potential. Evoking a physical picture we can think of the electron oscillating and emitting high-order harmonic radiation. As this motion is fed back into the potential in which the

electron moves, multiples of the frequencies emitted in the first plateau are also emitted. This view is confirmed by the existence of a third plateau with a cutoff of about $3(3.17U_p + I_p^{(1)})$. In the case of the BW05 potential we do not observe a second plateau for the three lowest intensities shown in Fig. 6.5. As the number of bound electrons $N(t)$ (3.10) does not fall below one for these intensities the potential of the BW05 calculation is the groundstate Hartree-exchange potential $v_{\text{hxc}}^{\text{BW05}}(t) = v_{\text{hx}}(t_0)$ (cf. Eq. (3.12)). Since no dynamic electron-electron interactions are included in v_c^{BW05} the non-existence of a plateau due to non-sequential double recombination was expected. In this intensity regime the system corresponds to two single-active electron equations for the respective electrons, explaining the similarity to the single-active electron results presented in Sec. 6.3. For the highest intensity in Fig. 6.5 the number of bound electrons drops below one during the interaction with the laser pulse and consequently $v_{\text{hxc}}^{\text{BW05}}(t) = 0$. This behavior induces a “noise” level which does not exhibit any further cutoffs about 10^8 times higher than the second plateau from the Schrödinger solution.

A frequency-time analysis supports the interpretation of the second plateau in approaches using the $v_{\text{hxc}}(t)$ potentials based on the nonlinear $v_{\text{hx}}(t)$ (3.8) as a replication of the first plateau. Calculating $|a(\Omega, t)|^2$ (6.12) for n^{LK05} and the intensities of Fig. 6.5 we attain the contour plots in Fig. 6.6. At the times when $|a(\Omega, t)|^2$ is large in the energy range of the first plateau, it is also enhanced in the range of the second plateau, i.e., whenever photons are emitted with a frequency Ω , then in a calculation with the v_c^{LK05} potential photons with 2Ω are emitted as well. This should be compared with Fig. 6.3 for the solution of the time-dependent Schrödinger equation where, for example, no enhancement in the range of the second plateau is observed for $2.0 \leq t/T_{\text{cyc}} \leq 2.5$. For the first plateau the time-dependent density functional calculation with v_c^{LK05} actually yields precisely the classically predicted energies though. We hence conclude that refined approximations of v_c will have to address the effects induced by the Hartree-exchange potential, with the second plateau of non-sequential double recombination serving as a sensitive benchmark of the quality of the approximation.

Chapter 7

Summary

A model Helium atom interacting with few-cycle laser pulses was studied using the time-dependent Schrödinger equation and time-dependent density functional theory.

From the solution of the Schrödinger equation we reproduced the experimentally observed enhanced double ionization probabilities due to a non-sequential ionization process with strong electron-electron interactions. The momentum distributions of the electrons as well as of the ion yielded valuable information about how double ionization proceeds at different intensities of the laser pulse. An electron which has left the atom can recombine at later times, emitting high-order harmonic radiation. We found a complementary process, non-sequential double recombination: Two electrons leave the atom sequentially and, through mutual interaction, recombine together, emitting a single photon.

Time-dependent density functional theory allows to describe the system by time-dependent Kohn-Sham equations for non-interacting electrons in an effective potential. In principle, this system can produce the exact time-dependent density and all observables through density functionals. In actual calculations two challenges are met. The exchange and correlation parts of the effective potential have to be approximated. In addition, for many observables functionals of the density are not known. In a system with strong electron-electron interactions these challenges are most pronounced so that ionization in the model Helium atom is especially suited to study them.

The results of the time-dependent Schrödinger equation were used as a reference for time-dependent density functional calculations. From the Schrödinger solution we constructed an exact Kohn-Sham orbital which would result from solving the Kohn-Sham equations with the exact effective potential.

We showed that for calculating ionization probabilities the knowledge of the exact density does not suffice. An accurate approximation of the functional for the observable is of utmost importance. An uncorrelated functional assuming the product of the Kohn-Sham orbitals to describe the wavefunction of the system was shown to be inadequate. We presented an appropriate functional which takes into

account electron correlations. It is based on the pair density of the electrons. This correlated functional can be formulated as the sum of the uncorrelated functionals and a correction term due to electron correlations. Employing a well-known groundstate correlation function to approximate the functional did not improve upon the uncorrelated approach. We therefore introduced an adiabatic approximation. This enabled us to reproduce the double ionization probabilities of the solution of the time-dependent Schrödinger equation, especially the characteristic “knee structure”, as a function of the intensity of the laser pulse. Making use of the dependence of the correction term on the number of bound electrons, an alternative approach using a fit function was presented. This approximation also enabled us to reproduce the double ionization probabilities.

An uncorrelated functional based on a product of the Kohn-Sham orbitals is also unable to reproduce the qualitative features of the momentum density of He^{2+} after the laser pulse. A functional of the Kohn-Sham orbitals was devised which includes correlation via the correlation function. It was shown that the phase of the correlated wavefunction is of minor importance compared to electron correlations. We demonstrated that for the exact correlation function this functional gives the correct qualitative features of the ion momentum density.

The exact functional of the density for high-order harmonic generation and thus for the radiation emitted in non-sequential double recombination is known. Hence, time-dependent density functional theory yields high-order harmonic spectra agreeing closely with the results from the time-dependent Schrödinger equation. However, the commonly used exchange-correlation potentials do not reproduce the typical features of non-sequential double recombination in the spectrum of the emitted radiation.

We evaluated the uncorrelated functionals for the ionization probabilities and the ion momentum density as well as the functional for the high-order harmonic spectra. Comparing to results obtained for the exact Kohn-Sham orbital then allowed us to assess the quality of different approximations of the correlation potential, as the exchange potential is known exactly for the Helium atom. We concluded that it is vital for the correlation potential to include a discontinuity at integer numbers of bound electrons. Furthermore, it needs to ensure that the ionization potential is held approximately constant until an electron has left the atom. The nonlinear “feedback” inherent in the effective potential through the Hartree potential was shown to lead to effects not present in the exact Kohn-Sham orbital and hence needs to be at least partly compensated by the exact correlation potential.

We have thus made significant progress in tackling a system generally regarded as showing the inadequacy of current implementations of time-dependent density functional theory. Future work will have to focus on further improving the approximation of the exchange-correlation potential and especially on investigating the role of electron correlations in the approximation of functionals for observables.

Appendix A

Numerical Implementation

The numerical implementation of the time-dependent Schrödinger and Kohn-Sham equations (Secs. A.1, A.2) for the model Helium atom (Chapter 3) are explained. We discretize both equations in Secs. A.3 and A.4 on a numerical grid. The approximation of the time-propagator is then highlighted (Secs. A.5, A.6) and it is shown how special care in the approximation can significantly improve the accuracy of numerical results. The groundstate of the system can be obtained by using the time-propagator (Sec. A.7). Due to the finite size of the numerical grid we have to make use of absorbing boundary conditions (Sec. A.8). In Sec. A.9 the parameters of the calculations used to acquire the numerical results in this work are detailed.

For notational clarity we will denote the electrons of the system with $k = 1, 2$ in this Appendix.

A.1 Time-Dependent Schrödinger Equation

The one-dimensional two-electron time-dependent Schrödinger equation (TDSE) for the model Helium atom is

$$i \partial_t \psi(x_1, x_2, t) = \hat{H}(x_1, x_2, t) \psi(x_1, x_2, t). \quad (\text{A.1})$$

To discuss the numerical implementation the Hamiltonian in velocity gauge and position space representation (3.5) is written in this chapter as

$$\hat{H}(x_1, x_2, t) = \sum_{k=1,2} \left(\hat{T}^k + \hat{H}_L^k + V^k \right) + W^{12}. \quad (\text{A.2})$$

The operators for the kinetic energy \hat{T}^k , the electron-laser interaction \hat{H}_L^k , the electron-nucleus interaction V^k and the electron-electron interaction W^{12} are given by

$$\begin{aligned} \hat{T}^k &= -\frac{1}{2} \partial_{x_k}^2, \\ \hat{H}_L^k &= -i A(t) \partial_{x_k}, \end{aligned}$$

$$\begin{aligned}
V^k &= V(x_k) = -\frac{2}{\sqrt{x_k^2 + \epsilon_{\text{en}}}}, \\
W^{12} &= W(|x_1 - x_2|) = \frac{1}{\sqrt{(x_1 - x_2)^2 + \epsilon_{\text{ee}}}}.
\end{aligned} \tag{A.3}$$

The dipole approximation for the laser field is used (cf. Sec. 3.1).

A.2 Time-Dependent Kohn-Sham Equation

In the model Helium atom both electrons are described by the same Kohn-Sham orbital (cf. Sec. 3.4). Hence, the one-dimensional time-dependent Kohn-Sham equation (TDKSE) we have to solve is

$$i \partial_t \phi(x, t) = \hat{H}^{\text{KS}}(x, t) \phi(x, t). \tag{A.4}$$

The Hamiltonian (3.7) is written analogously to the Schrödinger Hamiltonian (A.2) as

$$\hat{H}^{\text{KS}}(x, t) = \hat{T} + \hat{H}_L + V + V_{\text{hxc}} \tag{A.5}$$

in velocity gauge, using Eq. (A.3) with $k = 1$ and

$$V_{\text{hxc}} = v_{\text{hx}}(x, t) + v_{\text{c}}(x, t) = \int dx' \frac{|\phi(x', t)|^2}{\sqrt{(x - x')^2 + \epsilon_{\text{ee}}^{\text{KS}}}} + v_{\text{c}}(x, t), \tag{A.6}$$

the Hartree-exchange-correlation potential for the model Helium atom.

A.3 Discretization of the TDSE

In order to make the Schrödinger (A.1) and Kohn-Sham (A.4) equations numerically accessible we describe the system on a numerical grid. N_x grid points in each direction of the two-electron space are used with an equidistant spacing of Δx between grid points. The two-electron wavefunction $\psi(x_1, x_2, t)$ in discretized form is thus a matrix on the grid

$$(\boldsymbol{\psi})_{ij}(t) = \psi(i \Delta x, j \Delta x, t). \tag{A.7}$$

with $i, j = -N_x/2, \dots, N_x/2 - 1$ and N_x even.

We will now discuss how the operators (A.3) are discretized on this grid. An operator acting on x_1 has to be applied successively for all values of x_2 , i.e., for all j to the columns $\vec{\psi}_i^{(j)} = (\boldsymbol{\psi})_{ij}$. Correspondingly, an operator acting on x_2 has to be applied to the i rows $\vec{\psi}_j^{(i)} = (\boldsymbol{\psi})_{ij}$.

For the first spatial derivative in \hat{H}_L^k a Simpson approximation is employed

$$\frac{\partial}{\partial x} \psi \approx \mathbf{M}_1^{-1} \boldsymbol{\Delta}_1 \vec{\psi}, \tag{A.8}$$

which is correct to fourth order in Δx . The matrices are given by

$$\mathbf{M}_1 = \frac{1}{6} \begin{pmatrix} 4 & 1 & & & \\ 1 & 4 & 1 & & \\ & & \ddots & & \\ & & & 1 & 4 \\ 1 & & & & 4 \end{pmatrix}, \quad \mathbf{\Delta}_1 = \frac{1}{2\Delta x} \begin{pmatrix} 0 & 1 & & & \\ -1 & 0 & 1 & & \\ & & \ddots & & \\ & & & -1 & 0 \\ & & & & -1 & 0 \end{pmatrix}. \quad (\text{A.9})$$

The second spatial derivative in \hat{T}^k is approximated by a fourth-order Numerov expression

$$\frac{\partial^2}{\partial x^2} \psi \approx -2 \mathbf{M}_2^{-1} \mathbf{\Delta}_2 \vec{\psi}. \quad (\text{A.10})$$

The matrices are

$$\mathbf{M}_2 = -\frac{1}{6} \begin{pmatrix} 10 & 1 & & & \\ 1 & 10 & 1 & & \\ & & \ddots & & \\ & & & 1 & 10 \\ 1 & & & & 10 \end{pmatrix}, \quad \mathbf{\Delta}_2 = \frac{1}{(\Delta x)^2} \begin{pmatrix} -2 & 1 & & & \\ 1 & -2 & 1 & & \\ & & \ddots & & \\ & & & 1 & -2 \\ & & & & 1 & -2 \end{pmatrix}. \quad (\text{A.11})$$

In order for the time-propagation (see below) to be unitary, one has to ensure that the Hamiltonian is hermitian, i.e. $\hat{H} = (\hat{H}^*)^\text{T}$. \hat{H}_L^k and \hat{T}^k are hermitian if $\mathbf{M}_1^{-1} \mathbf{\Delta}_1$ is anti-hermitian and $\mathbf{M}_2^{-1} \mathbf{\Delta}_2$ is hermitian. It is easily calculated that replacing the (1,1) and (N_x, N_x) elements in \mathbf{M}_1 , $4 \rightarrow 2 + \sqrt{3}$ and in $\mathbf{\Delta}_1$, $0 \rightarrow \sqrt{3} - 2$ ensures the anti-hermiticity of $\mathbf{M}_1^{-1} \mathbf{\Delta}_1$. $\mathbf{M}_2^{-1} \mathbf{\Delta}_2$ is already hermitian. The discretized operators (A.3) of the Hamiltonian are thus

$$\begin{aligned} \hat{\mathbf{T}}^k &= \mathbf{M}_2^{-1} \mathbf{\Delta}_2, \\ \hat{\mathbf{H}}_\text{L}^k &= -i A(t) \mathbf{M}_1^{-1} \mathbf{\Delta}_1. \end{aligned} \quad (\text{A.12})$$

Analogously, the electron-nucleus interaction is discretized as the diagonal matrix

$$(\mathbf{V}^k)_{ij} = V(i \Delta x) \delta_{ij}. \quad (\text{A.13})$$

The electron-electron interaction depends on the position of both electrons and is therefore written as the nondiagonal matrix

$$(\mathbf{W}^{12})_{ij} = W(|i \Delta x - j \Delta x|). \quad (\text{A.14})$$

In the above formulas, k denotes the first or second electron. As pointed out above, the matrices then act either on rows or columns of ψ . This is ensured when writing the time-dependent Schrödinger equation in discretized form by inserting δ_{ij} ,

$$\begin{aligned} i \partial_t (\psi)_{ij} &= \sum_{i'j'} \left[(\hat{\mathbf{T}}^1)_{ii'} \delta_{jj'} + (\mathbf{V}^1)_{ii'} \delta_{jj'} + (\hat{\mathbf{H}}_\text{L}^1)_{ii'} \delta_{jj'} + (\hat{\mathbf{T}}^2)_{jj'} \delta_{ii'} \right. \\ &\quad \left. + (\hat{\mathbf{H}}_\text{L}^2)_{jj'} \delta_{ii'} + (\mathbf{V}^2)_{jj'} \delta_{ii'} + (\mathbf{W}^{12})_{ij} \delta_{ii'} \delta_{jj'} \right] (\psi)_{i'j'}. \end{aligned} \quad (\text{A.15})$$

A.4 Discretization of the TDKSE

The Kohn-Sham equation (A.4) is discretized completely analogously to the Schrödinger equation. Since we have only one orbital, this orbital is given by a vector on a grid with N_x grid points

$$(\phi)_i(t) = \phi(i \Delta x, t), \quad (\text{A.16})$$

where $i = -N_x/2, \dots, N_x/2 - 1$ and N_x even. The matrix representation of v_{hxc} is

$$(\mathbf{V}_{\text{hxc}})_{ij} = [v_{\text{hx}}(i \Delta x, t) + v_{\text{c}}(i \Delta x, t)] \delta_{ij}. \quad (\text{A.17})$$

With Eqs. (A.12), (A.13) and $k = 1$ the time-dependent Kohn-Sham equation in matrix form then is

$$i \partial_t (\phi)_i = \sum_{i'} \left[(\hat{\mathbf{T}})_{ii'} + (\hat{\mathbf{H}}_{\text{L}})_{ii'} + (\mathbf{V})_{ii'} + (\mathbf{V}_{\text{hxc}})_{ii'} \right] (\phi)_{i'} \quad (\text{A.18})$$

A.5 Time-Propagation of the TDSE Wavefunction

A.5.1 Short-Time Propagator

Given an initial state $\psi(x_1, x_2, t_0)$, a solution of the time-dependent Schrödinger equation (A.1) is given by

$$\psi(x_1, x_2, T) = U(T, t_0) \psi(x_1, x_2, t_0). \quad (\text{A.19})$$

U is the time propagator. Deducing the form of the time propagator from the Schrödinger equation for infinitesimal timesteps dt and taking the limit $dt \rightarrow 0$ (see, e.g., [59]) one has

$$U(T, t_0) = \hat{T} e^{-i \int_{t_0}^T dt' \hat{H}(x_1, x_2, t')}, \quad (\text{A.20})$$

where the time-ordering operator \hat{T} is used.

In our implementation we use N_t finite time-steps $\Delta t = (T - t_0) / N_t$. The time-dependence of \hat{H} and the effect of the time-ordering are negligible in the short interval Δt . Therefore the time propagator is approximated as

$$U(t, t_0) \approx \prod_{i=0}^{N_t-1} U(t_i + \Delta t, t_i), \quad (\text{A.21})$$

with the short-time propagator

$$U(t + \Delta t, t) \approx e^{-i \Delta t \hat{H}(x_1, x_2, t)}. \quad (\text{A.22})$$

A.5.2 Approximation of the Short-Time Propagator

The short-time propagator (A.22) can only be applied to the wavefunction ψ by simple multiplication if the Hamiltonian is diagonal. Diagonalizing the Hamiltonian in every timestep is numerically demanding. Therefore, we make use of the Crank-Nicolson approximation [68]

$$U_{\text{CN}}(t + \Delta t, t) = \left(1 + i\frac{\Delta t}{2}\hat{H}\right)^{-1} \left(1 - i\frac{\Delta t}{2}\hat{H}\right) \quad (\text{A.23})$$

of the short-time propagator

$$U(t + \Delta t, t) = U_{\text{CN}}(t + \Delta t, t) + \mathcal{O}[(\Delta t)^3], \quad (\text{A.24})$$

where $\hat{H} = \hat{H}(x_1, x_2, t)$. The order of the error follows from comparing the expansion of the short-time propagator

$$U(t + \Delta t, t) = 1 - i\Delta t \hat{H} - \frac{1}{2}(\Delta t)^2 \hat{H}^2 + i\frac{1}{6}(\Delta t)^3 \hat{H}^3 + \dots \quad (\text{A.25})$$

and the Crank-Nicolson short-time propagator

$$U_{\text{CN}}(t + \Delta t, t) = 1 - i\Delta t \hat{H} - \frac{1}{2}(\Delta t)^2 \hat{H}^2 + i\frac{1}{4}(\Delta t)^3 \hat{H}^3 + \dots \quad (\text{A.26})$$

Unitarity of the time propagator is conserved in this approximation as can be seen directly from Eq. (A.23). Since we already assumed our Hamiltonian to be non-diagonal, U_{CN} cannot be simply applied in the form given by Eq. (A.23). Instead, it yields an implicit equation

$$\left(1 + i\frac{\Delta t}{2}\hat{H}\right) \psi(t + \Delta t) = \left(1 - i\frac{\Delta t}{2}\hat{H}\right) \psi(t) \quad (\text{A.27})$$

which has to be solved for $\psi(t + \Delta t)$.

A.5.3 Short-Time Propagator Splitting

When using the Crank-Nicolson approximation (A.23) of the short-time propagator on a discretized grid, it is desirable to apply the approximation to the short-time propagators of individual parts of the Hamiltonian \hat{H} . This leads to implicit equations of the form of Eq. (A.27) for each part. By splitting the Hamiltonian \hat{H} as in Eq. (A.2) into a laser-interaction $\hat{H}_{\text{L}} = \hat{H}_{\text{L}}^1 + \hat{H}_{\text{L}}^2$ and an atomic part $\hat{H}_{\text{A}} = \hat{H} - \hat{H}_{\text{L}}$, we can numerically calculate a solution without the need to invert matrices, as will be shown in Sec. A.5.4.

A straightforward approach to the splitting of Eq. (A.22) then is

$$U(t + \Delta t, t) \approx e^{-i\Delta t \hat{H}_{\text{A}}} e^{-i\Delta t \hat{H}_{\text{L}}} + \frac{1}{2}[\hat{H}_{\text{A}}, \hat{H}_{\text{L}}](\Delta t)^2, \quad (\text{A.28})$$

with a second-order error in the timestep Δt due to the noncommutativity of \widehat{H}_L and \widehat{H}_A . This error follows from the Baker-Campbell-Hausdorff formula, which in its third-order form is given by

$$e^X e^Y = e^{X+Y+\frac{1}{2}[X,Y]+\frac{1}{12}[X,[X,Y]]-\frac{1}{12}[Y,[X,Y]]}, \quad (\text{A.29})$$

and subsequent expansion of the exponential function on the right hand side up to the lowest order of the error.

With $\tau = \Delta t/2$ we can alternatively approximate the short-time propagator (A.22) as

$$U(t + \Delta t, t) = e^{-i\tau \widehat{H}_L} e^{-i\Delta t \widehat{H}_A} e^{-i\tau \widehat{H}_L} + \epsilon(\widehat{H}_L, \widehat{H}_A) (\Delta t)^3. \quad (\text{A.30})$$

From repeated application of Eq. (A.29) the function ϵ follows as

$$\epsilon(\widehat{H}_L, \widehat{H}_A) = \frac{1}{12} i \left(\frac{1}{2} [\widehat{H}_L, [\widehat{H}_L, \widehat{H}_A]] + [\widehat{H}_A, [\widehat{H}_L, \widehat{H}_A]] \right). \quad (\text{A.31})$$

Equation (A.30) improves the result of Eq. (A.28) by one order, being exact up to the second-order in Δt . Since $[\widehat{H}_L^1, \widehat{H}_L^2] = 0$, we can split the short-time propagator further without introducing additional errors

$$U(t + \Delta t, t) = e^{-i\tau \widehat{H}_L^2} e^{-i\tau \widehat{H}_L^1} e^{-i\Delta t \widehat{H}_A} e^{-i\tau \widehat{H}_L^2} e^{-i\tau \widehat{H}_L^1} + \mathcal{O}[(\Delta t)^3]. \quad (\text{A.32})$$

There are different options to split the atomic part \widehat{H}_A . We define

$$\widehat{H}_A^k = \widehat{T}^k + V^k, \quad (\text{A.33})$$

$$\widetilde{H}_A^k = \widehat{T}^k + \frac{1}{2} (V^1 + V^2 + W^{12}). \quad (\text{A.34})$$

The whole atomic Hamiltonian is then $\widehat{H}_A = \widehat{H}_A^1 + \widehat{H}_A^2 + W^{12} = \widetilde{H}_A^1 + \widetilde{H}_A^2$. A straightforward splitting is given by

$$e^{-i\Delta t \widehat{H}_A} \stackrel{\text{(a)}}{=} e^{-i\Delta t \widetilde{H}_A^2} e^{-i\Delta t \widetilde{H}_A^1} + \mathcal{O}[(\Delta t)^2]. \quad (\text{A.35})$$

Because the \widetilde{H}_A^k do not commute this approach introduces an error of second order in Δt , as in the mathematically equivalent splitting of Eq. (A.28). To reduce this error we write

$$e^{-i\Delta t \widehat{H}_A} \stackrel{\text{(b)}}{=} e^{-i\tau \widetilde{H}_A^1} e^{-i\Delta t \widetilde{H}_A^2} e^{-i\tau \widetilde{H}_A^1} + \mathcal{O}[(\Delta t)^3], \quad (\text{A.36})$$

which has only an error of third order (cf. Eq. (A.30)). Apart from the error in Δt , a high symmetry in x_1 and x_2 is desirable in the numerical implementation, in order not to deviate from the physical symmetry of the system given by $\widehat{H}(x_1, x_2, t) =$

$\hat{H}(x_2, x_1, t)$. Using $[\hat{H}_A^1, \hat{H}_A^2] = 0$ and $[\hat{H}_A^k, W^{12}] \neq 0$ this suggests the following splitting

$$e^{-i\Delta t \hat{H}_A} \stackrel{(c)}{\approx} e^{-i\tau W^2} e^{-i\tau \hat{H}_A^1} e^{-i\Delta t W^{12}} e^{-i\tau \hat{H}_A^2} e^{-i\tau \hat{H}_A^1} + \mathcal{O}[(\Delta t)^3], \quad (\text{A.37})$$

which is, just as splitting (b), exact up to the second order in Δt .

When applying the split terms numerically the Crank-Nicolson approximation (A.24) is used, which has an error of $\mathcal{O}[(\Delta t)^3]$. The splittings of the short-time propagator (A.28), (A.30) and (A.35)-(A.37) introduce an error of at least third order in Δt . Therefore, only the splittings (b) and (c), combined with Eq. (A.32) are of the same order as the Crank-Nicolson approximation.

A.5.4 Discretization of the Split Short-Time Propagator

We use the discretization of our system in terms of matrices as described in Sec. A.3 to discretize the Crank-Nicolson approximation (A.23) of each part of the different splittings of the short-time propagator introduced in the previous section.

For the interaction with the laser field we obtain from Eq. (A.12) for the factors in Eq. (A.32)

$$\begin{aligned} e^{-i\tau \hat{H}_L^k} &\approx \left(\mathbf{1} + i\frac{\tau}{2} [-i A \mathbf{M}_1^{-1} \boldsymbol{\Delta}_1] \right)^{-1} \left(\mathbf{1} - i\frac{\tau}{2} [-i A \mathbf{M}_1^{-1} \boldsymbol{\Delta}_1] \right) \\ &= \underbrace{\left(\mathbf{M}_1 + \frac{\tau}{2} A \boldsymbol{\Delta}_1 \right)^{-1}}_{(\hat{L}_+^k)^{-1}} \underbrace{\left(\mathbf{M}_1 - \frac{\tau}{2} A \boldsymbol{\Delta}_1 \right)}_{(\hat{L}_-^k)}. \end{aligned} \quad (\text{A.38})$$

It is important to note that with Eq. (A.38) inverting \mathbf{M}_1 can be avoided when solving the ensuing implicit Eqs. (A.44). As pointed out at the beginning of Sec. A.5.3 this is the reason to split the full Hamiltonian into a laser-interaction and an atomic part. Just as in Eq. (A.15), matrices act on columns of the wavefunction in matrix form ψ for $k = 1$ and on rows for $k = 2$. Along these lines we acquire for the atomic Hamiltonian \hat{H}_A used in Eq. (A.37),

$$e^{-i\tau \hat{H}_A^k} \approx \underbrace{\left(\mathbf{M}_2 + i\frac{\tau}{2} (\boldsymbol{\Delta}_2 + \mathbf{M}_2 \mathbf{V}) \right)^{-1}}_{(\hat{A}_+^k)^{-1}} \underbrace{\left(\mathbf{M}_2 - i\frac{\tau}{2} (\boldsymbol{\Delta}_2 + \mathbf{M}_2 \mathbf{V}) \right)}_{(\hat{A}_-^k)}. \quad (\text{A.39})$$

Similarly, for the atomic Hamiltonian \tilde{H}_A from Eqs. (A.35) and (A.36) we have

$$\begin{aligned} e^{-i\tau \tilde{H}_A^k} &\approx \underbrace{\left(\mathbf{M}_2 + i\frac{\tau}{2} \left(\boldsymbol{\Delta}_2 + \frac{1}{2} \mathbf{M}_2 (\mathbf{V}^1 + \mathbf{V}^2 + \mathbf{W}^{12}) \right) \right)^{-1}}_{(\tilde{A}_+(\tau))^k} \\ &\quad \times \underbrace{\left(\mathbf{M}_2 - i\frac{\tau}{2} \left(\boldsymbol{\Delta}_2 + \frac{1}{2} \mathbf{M}_2 (\mathbf{V}^1 + \mathbf{V}^2 + \mathbf{W}^{12}) \right) \right)}_{(\tilde{A}_-(\tau))^k}, \end{aligned} \quad (\text{A.40})$$

where $(\mathbf{V}^1 + \mathbf{V}^2 + \mathbf{W}^{12})_{ij} = V(i \Delta x) + V(j \Delta x) + W(|i \Delta x - j \Delta x|)$. For the electron-electron interaction in Eq. (A.37) we just use the exponential function

$$\left(\widehat{I}^{12}\right)_{ij} = e^{-i \Delta t (\mathbf{W}^{12})_{ij}}. \quad (\text{A.41})$$

We can thus write explicitly for the short-time propagation of the wavefunction in matrix form

$$\begin{aligned} \psi(t + \Delta t) &= \left(\widehat{L}_+^2\right)^{-1} \left(\widehat{L}_-^2\right) \left(\widehat{L}_+^1\right)^{-1} \left(\widehat{L}_-^1\right) U_A \\ &\quad \times \left(\widehat{L}_+^2\right)^{-1} \left(\widehat{L}_-^2\right) \left(\widehat{L}_+^1\right)^{-1} \left(\widehat{L}_-^1\right) \psi(t), \end{aligned} \quad (\text{A.42})$$

with the atomic part of the short-time propagator for the different splittings (a)-(c) introduced above,

$$\begin{aligned} U_A^{(a)} &= \left(\widetilde{A}_+^2(\Delta t)\right)^{-1} \left(\widetilde{A}_-^2(\Delta t)\right) \left(\widetilde{A}_+^1(\Delta t)\right)^{-1} \left(\widetilde{A}_-^1(\Delta t)\right), \\ U_A^{(b)} &= \left(\widetilde{A}_+^1(\tau)\right)^{-1} \left(\widetilde{A}_-^1(\tau)\right) \left(\widetilde{A}_+^2(\Delta t)\right)^{-1} \left(\widetilde{A}_-^2(\Delta t)\right) \\ &\quad \times \left(\widetilde{A}_+^1(\tau)\right)^{-1} \left(\widetilde{A}_-^1(\tau)\right), \\ U_A^{(c)} &= \left(\widehat{A}_+^2\right)^{-1} \left(\widehat{A}_-^2\right) \left(\widehat{A}_+^1\right)^{-1} \left(\widehat{A}_-^1\right) \left(\widehat{I}^{12}\right) \left(\widehat{A}_+^2\right)^{-1} \\ &\quad \times \left(\widehat{A}_-^2\right) \left(\widehat{A}_+^1\right)^{-1} \left(\widehat{A}_-^1\right). \end{aligned} \quad (\text{A.43})$$

Equation (A.42) then yields implicit matrix equations for the split parts of the full Hamiltonian of the form of Eq. (A.27). These are then solved successively from the right by solving

$$\begin{aligned} \widehat{L}_+^1 \varphi^{(1)}(t) &= \widehat{L}_-^1 \psi(t) \\ \widehat{L}_+^2 \varphi^{(2)}(t) &= \widehat{L}_-^2 \varphi^{(1)}(t) \\ &\vdots \end{aligned} \quad (\text{A.44})$$

for the $\varphi^{(i)}$, yielding in the last step $\psi(t + \Delta t)$. This is accomplished easily numerically because the $\widehat{L}_\pm^k, \widetilde{A}_\pm^k, \widehat{A}_\pm^k$ are tridiagonal matrices and \widehat{I}^{12} requires multiplications only.

A.5.5 Comparison of Different Splittings

With Eqs. (A.42) and (A.43) it is clear how to propagate an initial state on the numerical grid in time. However, for actual calculations we have to compare the different options to split the atomic Hamiltonian according to Eqs. (A.35), (A.36) and (A.37).

From Eq. (A.35) we know that (a) is one order less exact in Δt than (b) and (c). However, in each timestep (a) involves only two matrix multiplications and

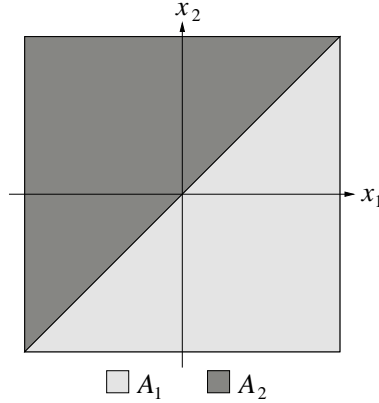


Figure A.1: Schematic illustration of the A_i . The difference of the norm of the wavefunction in A_1 and A_2 yields A , a measure of the asymmetry of the wavefunction.

solutions of implicit matrix equations for each electron. The numerical effort for (b) is already three matrix multiplications and implicit equations and for (c) it is four matrix multiplications and implicit equations. A good estimate is thus that the efforts of the implementations are related like (a):(b):(c) 1:1.5:2.

In order to decide which of the splittings (a)-(c) of the atomic Hamiltonian is suited best for our application we investigate the relative quality of the different approaches under conditions similar to the situation when propagating our one-dimensional model Helium atom in a laser field. There exist two important physical conditions which a suitable implementation has to fulfill as good as possible. It has to conserve symmetry of the wavefunction $\psi(x_1, x_2, t) = \psi(x_2, x_1, t)$, which follows from the symmetry of the Hamiltonian (A.2). In addition, a groundstate wavefunction acquired by propagation in imaginary time (cf. section A.7) has to be stable when propagated in real time without interacting with an external field, i.e., no density should leave the vicinity of the nucleus (and thus the grid).

To examine these criteria we choose a grid spacing $\Delta x = 0.4$ a.u. and a timestep of $\Delta t = 0.075$ a.u. as in our actual calculations (cf. Sec. A.9). The groundstate is calculated by propagating a Gaussian seed function $N_t^i = 1000$ timesteps in imaginary time with $\Delta t = -i0.075$ a.u. (cf. Sec. A.7). Because we are only interested in the splitting of the atomic part of the Hamiltonian, we do not apply a laser field and propagate the groundstate wavefunction for $N_t = 1000$ timesteps on a $N_x = 500$ grid with absorbing boundary conditions as described in Sec. A.8.

We calculate for $i, j \in \{1, 2\}$ at time $t = T$ after the propagation from

$$A_i = \int_{-\infty}^{+\infty} dx_i \int_{-\infty}^{x_i} dx_{j \neq i} |\psi(x_1, x_2, T)|^2 \quad (\text{A.45})$$

as a measure of the asymmetry the value

$$A = |A_1 - A_2|. \quad (\text{A.46})$$

Table A.1: Comparison of the quality of the different splittings of the atomic Hamiltonian (A.35)-(A.37). The change of n and A due to the real-time propagation is included in the columns Δn and ΔA .

	N_t	n	Δn	A	ΔA
(a)	0	1.00		3.02×10^{-16}	
(a)	1000	1.00	-1.25×10^{-4}	1.11×10^{-8}	1.11×10^{-8}
(b)	0	1.00		4.67×10^{-16}	
(b)	1000	1.00	-8.33×10^{-8}	1.30×10^{-12}	1.30×10^{-12}
(c)	0	1.00		7.89×10^{-16}	
(c)	1000	1.00	-9.73×10^{-7}	2.00×10^{-15}	1.22×10^{-15}

The respective A_i are shown in Fig. A.1 in the two-electron space. To be able to estimate the numerical stability of the groundstate we calculate the norm on the grid at time T

$$n = \int_{-\infty}^{+\infty} dx_1 \int_{-\infty}^{+\infty} dx_2 |\psi(x_1, x_2, T)|^2. \quad (\text{A.47})$$

The integrals are approximated by a Riemann sum and infinite integral limits are replaced by the boundaries of the grid. For a perfect propagation algorithm the groundstate would be stable ($n = 1$) and the wavefunction symmetric ($A = 0$).

From Tab. A.1 it is clear that the implementation (a) of the propagation algorithm leads to an unstable groundstate and an increasing asymmetry. We attribute this to the fact that both electrons are treated asymmetrically, i.e., that the differentiation is always done first with respect to x_1 (cf. Eq. (A.35)) as well as the fact that it is exact only up to the first order in the timestep.

The loss of norm in the course of propagation is reduced by four orders of magnitude by the improved splittings (b) and (c). The slightly better result for (b) is most likely due to the reduced number of numerical operations (cf. Eq. (A.36) vs. Eq. (A.37)) and the subsequent reduction of rounding errors. In terms of asymmetry, the groundstate asymmetry is comparable for (b) and (c), while the asymmetry developing in real-time propagation is better by three orders of magnitude for (c).

Since our analysis in actual calculations involves integrating out one variable, we decided to optimize the asymmetry behavior and therefore used propagation algorithm (c) for all numerical calculations presented in this work.

To illustrate the improvement of the algorithm (c) as compared to (a) we show in Tab. A.2 the average difference in asymmetry between the groundstate and the final state after propagation and interaction with different few-cycle laser pulses. The parameters of the calculations are detailed in Sec. A.9.

Table A.2: Growth of the asymmetry as compared to the groundstate asymmetry for splittings (a) and (c) after interaction of the model Helium atom with different laser pulses (cf. Sec. A.9). The average value for nineteen different effective peak intensities is presented for each laser pulse.

	λ	N	$\langle \Delta A \rangle$
(a)	614 nm	3	6.45×10^{-4}
(a)	780 nm	3	6.87×10^{-4}
(a)	780 nm	4	3.57×10^{-4}
(c)	614 nm	3	1.24×10^{-16}
(c)	780 nm	3	4.11×10^{-16}
(c)	780 nm	4	3.21×10^{-16}

A.6 Time-Propagation of the TDKSE Orbital

Since we have only one orbital in the Kohn-Sham equation we use Eq. (A.30) for the interaction with the laser field while the atomic part of the Kohn-Sham Hamiltonian

$$\hat{H}_A^{\text{KS}} = \hat{T} + V + V_{\text{hxc}} \quad (\text{A.48})$$

does not need to be split further. To ensure greatest analogy to Eq. (A.37) we use the ‘‘splitting’’

$$e^{-i\Delta t \hat{H}_A^{\text{KS}}} \stackrel{(c')}{=} e^{-i\tau \hat{H}_A^{\text{KS}}} e^{-i\tau \hat{H}_A^{\text{KS}}}. \quad (\text{A.49})$$

This leads to the atomic part of the short-time propagator in discretized form

$$e^{-i\tau \hat{H}_A^{\text{KS}}} \simeq \underbrace{\left(\mathbf{M}_2 + i \frac{\tau}{2} (\boldsymbol{\Delta}_2 + \mathbf{M}_2 \mathbf{V} + \mathbf{M}_2 \mathbf{V}_{\text{hxc}}) \right)^{-1}}_{(\hat{A}_+^{\text{KS}})^{-1}} \underbrace{\left(\mathbf{M}_2 - i \frac{\tau}{2} (\boldsymbol{\Delta}_2 + \mathbf{M}_2 \mathbf{V} + \mathbf{M}_2 \mathbf{V}_{\text{hxc}}) \right)}_{(\hat{A}_-^{\text{KS}})}. \quad (\text{A.50})$$

The explicit equation for the short-time propagation is then

$$\begin{aligned} \phi(t + \Delta t) &= \left(\hat{L}_+ \right)^{-1} \left(\hat{L}_- \right) \left(\hat{A}_+^{\text{KS}} \right)^{-1} \left(\hat{A}_-^{\text{KS}} \right) \left(\hat{A}_+^{\text{KS}} \right)^{-1} \left(\hat{A}_-^{\text{KS}} \right) \\ &\quad \left(\hat{L}_+ \right)^{-1} \left(\hat{L}_- \right) \phi(t). \end{aligned} \quad (\text{A.51})$$

This equation is solved successively as described for the time-dependent Schrödinger equation in Sec. A.5.4.

A.7 Groundstate Calculation

The Schrödinger equation (A.1) describes the time-evolution of an initial state $\psi_0 = \psi(x_1, x_2, t_0)$. In our case, the initial state is the groundstate of our two-electron model Helium atom, i.e., the solution of the stationary Schrödinger equation

$$E_0 \psi_0(x_1, x_2) = \hat{H}_0(x_1, x_2) \psi_0(x_1, x_2). \quad (\text{A.52})$$

The Hamiltonian is given by the Hamiltonian of the time-evolution (A.2) without the interaction with the laser field

$$\hat{H}_0(x_1, x_2) = \sum_{k=1,2} \left(-\frac{1}{2} \partial_{x_k}^2 + V(x_k) \right) + W(|x_1 - x_2|). \quad (\text{A.53})$$

The initial state used in the time-dependent Kohn-Sham equation (A.4) is the solution of the stationary Kohn-Sham equation

$$E_0 \phi_0(x) = \hat{H}_0^{\text{KS}}(x) \phi_0(x), \quad (\text{A.54})$$

with the groundstate Hamiltonian

$$\hat{H}_0^{\text{KS}}(x) = -\frac{1}{2} \partial_x^2 + V(x) + v_{\text{hx}}(x, t) + v_c(x, t). \quad (\text{A.55})$$

For the form of the softcore-potentials used in this work, no analytical solutions of Eqs. (A.52), (A.54) are known. Therefore, we determine the groundstate numerically. Observing that the groundstate is the state with the lowest energy, we use the propagation algorithm described above with the vector potential set to zero ($A = 0$) and an imaginary timestep $\Delta t_i = -i \Delta t$. The expansion of the wavefunction propagated one imaginary time ψ_i in terms of eigenfunctions of \hat{H}_0 is

$$\psi(-i\Delta t) = \sum_n c_n e^{-E_n \Delta t} \psi_n. \quad (\text{A.56})$$

Therefore, for bound states with $E_n < 0$ successive propagation in imaginary time amplifies the state with the lowest energy E_n (the groundstate) most. Normalization to one after each timestep thus leads to

$$\psi(-N_t^i i \Delta t) \approx \psi_0 \quad (\text{A.57})$$

after a sufficient number of imaginary timesteps N_t^i . In principle, this approach works for an arbitrary non-vanishing seed function. In order to reduce the number of imaginary timesteps N_t^i required, we use a Gaussian seed function, which is already close to the groundstate wavefunction. The same arguments hold for the Kohn-Sham equation. Thus, the groundstate Kohn-Sham orbital is determined in the same way.

Imaginary time-propagation to acquire the groundstate wavefunction has been successfully employed in numerous publications (see, e.g., [37, 39, 69]).

The groundstate energy of the respective system is then calculated as the expectation value of the Hamiltonian $E_0 = \langle \hat{H}_0 \rangle$. The system is discretized as described in Secs. A.3 and A.4. The integrals are approximated by a Riemann sum over the numerical grid.

A.8 Absorbing Boundary Conditions

A challenge posed by propagation in real space on a finite grid is the fact that probability density might propagate to the boundary of the grid. In general, this will lead to a reflection of the wavefunction and consequently to spurious effects in the properties of interest. One solution is to choose the grid large enough. Since this approach is limited by the numerical effort required, it is combined with “absorbing boundary conditions” [70, 71], which “dissipate” the probability density reaching the boundary.

We implement the absorbing boundary as an imaginary potential with small values at the center and rapidly increasing values close to the boundary of the grid. We use the explicit discretized matrix form

$$\left(\mathbf{V}_i^k\right)_{ij} = -iC \left(\frac{i - \frac{1}{2}N_x + \frac{1}{2}}{\frac{1}{2}N_x}\right)^{16} \delta_{ij}, \quad (\text{A.58})$$

centered on the grid with an even number of N_x grid points in each direction of the two-electron space and $i, j = -N_x/2, \dots, N_x/2 - 1$. C is a large but otherwise arbitrary factor. In the calculations presented here, we used $C = 50$.

The imaginary potential is included in the Hamiltonians of Eqs. (A.2), (A.5) by adding it to the electron-nucleus potentials V because of its similar structure, i.e., its diagonal form. In the formulas for the discretized short-time propagator of the Schrödinger equation we therefore use $\mathbf{V}^k \rightarrow \mathbf{V}^k + \mathbf{V}_i^k$. Analogously, we use in the Kohn-Sham equation $\mathbf{V} \rightarrow \mathbf{V} + \mathbf{V}_i$ with $k = 1$.

It is important to note that this approach does not conserve the unitarity of the time-evolution.

A.9 Parameters of Calculations

As a reference we will detail the parameters employed in the calculations of the results presented in Chapters 4 - 6.

The groundstate wavefunction is determined by propagating a Gaussian seed function for $N_t^i = 1000$ imaginary timesteps $\Delta t = i0.075$ a.u. on a grid with $N_x = 500$ gridpoints in each direction of the two-electron space (cf. Eq.(A.7)). A grid point spacing of $\Delta x = 0.4$ a.u. ($\Delta x = 0.2$ a.u. for the $N = 6$ pulse) was used.

All numerical calculations were performed with a timestep of $\Delta t = 0.075$ a.u. for $0 \leq i \Delta t \leq T$ with $i = 0, \dots, N_t$ and T the duration of the respective laser pulse. The number of grid points and grid spacings for the different laser pulses (cf. Tab. 3.1) are given in Tab. A.3. They are chosen to ensure that the norm of the wavefunction on the grid after the laser pulse is sufficiently close to one and that the relevant dynamics are described well by the discretized system.

Table A.3: Size of the numerical grid in each direction of the two-electron space N_x and spacing of grid points Δx used in the numerical calculations presented in the respective Chapter. For each laser pulse, simulations were performed for nineteen values of \hat{A} in the listed range. For the $\lambda = 780$ nm, $N=4$ laser pulse $N_x = 6500$ was used for the six highest values of \hat{A} .

λ (nm)	N	N_x	Δx	\hat{A}	Chapter
248 nm	3	1500	0.4 a.u.	0.41-2.60	4
614 nm	3	5500	0.4 a.u.	1.29-8.17	4
780 nm	3	5500	0.4 a.u.	1.29-8.17	4, 5
780 nm	4	5500/6500	0.4 a.u.	1.25-7.93	4
780 nm	6	1500	0.2 a.u.	1.23-7.76	6

Bibliography

- [1] T. Brabec and F. Krausz, *Rev. Mod. Phys.* **72**, 545 (2000).
- [2] G. G. Paulus, F. Lindner, H. Walther, A. Baltuska, E. Goulielmakis, M. Lezius, and F. Krausz, *Phys. Rev. Lett.* **91**, 253004 (2003).
- [3] A. Baltuška, T. Udem, M. Uiberacker, M. Hentschel, E. Goulielmakis, C. Gohle, R. Holzwarth, V. S. Yakovlev, A. Scrinzi, T. W. Hänsch, and F. Krausz, *Nature* **421**, 611 (2003).
- [4] M. Drescher, M. Hentschel, R. Kienberger, G. Tempea, C. Spielmann, G. A. Reider, P. B. Corkum, and F. Krausz, *Science* **291**, 1923 (2001).
- [5] P. Agostini and L. F. DiMauro, *Rep. Prog. Phys.* **67**, 813 (2004).
- [6] J. Ullrich, R. Moshhammer, A. Dorn, R. Dörner, L. P. H. Schmidt, and H. Schmidt-Böcking, *Rep. Prog. Phys.* **66**, 1463 (2003).
- [7] M. Protopapas, C. H. Keitel, and P. L. Knight, *Rep. Prog. Phys.* **60**, 389 (1997).
- [8] W. Becker, F. Grasbon, R. Kopold, D. B. Milošević, G. G. Paulus, and H. Walther, *Adv. At. Mol. Opt. Phys.* **48**, 35 (2002).
- [9] D. N. Fittinghoff, P. R. Bolton, B. Chang, and K. C. Kulander, *Phys. Rev. Lett.* **69**, 2642 (1992).
- [10] B. Walker, B. Sheehy, L. F. DiMauro, P. Agostini, K. J. Schafer, and K. C. Kulander, *Phys. Rev. Lett.* **73**, 1227 (1994).
- [11] T. Weber, M. Weckenbrock, A. Staudte, L. Spielberger, O. Jagutzki, V. Mergel, F. Afaneh, G. Urbasch, M. Vollmer, H. Giessen, and R. Dörner, *Phys. Rev. Lett.* **84**, 443 (2000).
- [12] A. Rudenko, K. Zrost, B. Feuerstein, V. L. B. Jesus, C. D. Schröter, R. Moshhammer, and J. Ullrich, *Phys. Rev. Lett.* **93**, 253001 (2004).
- [13] X. Liu, H. Rottke, E. Eremina, W. Sandner, E. Goulielmakis, K. O. Keeffe, M. Lezius, F. Krausz, F. Lindner, M. G. Schatzel, G. G. Paulus, and H. Walther, *Phys. Rev. Lett.* **93**, 263001 (2004).

-
- [14] A. Scrinzi, M. Y. Ivanov, R. Kienberger, and D. M. Villeneuve, *J. Phys. B: At. Mol. Opt. Phys.* **39**, R1 (2006).
- [15] M. Lewenstein, P. Balcou, M. Y. Ivanov, A. L'Huillier, and P. B. Corkum, *Phys. Rev. A* **49**, 2117 (1994).
- [16] W. Kohn, *Rev. Mod. Phys.* **71**, 1253 (1999).
- [17] J. S. Parker, L. R. Moore, D. Dundas, and K. T. Taylor, *J. Phys. B: At. Mol. Opt. Phys.* **33**, L691 (2000).
- [18] L. V. Keldysh, *Sov. Phys. – JETP* **20**, 1307 (1965).
- [19] F. H. M. Faisal, *J. Phys. B: At. Mol. Phys.* **6**, L89 (1973).
- [20] H. R. Reiss, *Phys. Rev. A* **22**, 1786 (1980).
- [21] A. Becker and F. H. M. Faisal, *Phys. Rev. A* **59**, R1742 (1999).
- [22] A. Becker, R. Dörner, and R. Moshhammer, *J. Phys. B: At. Mol. Opt. Phys.* **38**, S753 (2005).
- [23] L.-B. Fu, J. Liu, J. Chen, and S.-G. Chen, *Phys. Rev. A* **63**, 043416 (2001).
- [24] P. J. Ho, R. Panfili, S. L. Haan, and J. H. Eberly, *Phys. Rev. Lett.* **94**, 093002 (2005).
- [25] P. G. Burke, P. Francken, and C. J. Joachain, *J. Phys. B: At. Mol. Opt. Phys.* **24**, 751 (1991).
- [26] J. Zanghellini, M. Kitzler, C. Fabian, T. Brabec, and A. Scrinzi, *Laser Phys.* **13**, 1064 (2003).
- [27] L. Feng and H. W. van der Hart, *J. Phys. B: At. Mol. Opt. Phys.* **36**, L1 (2003).
- [28] M. Kitzler, J. Zanghellini, C. Jungreuthmayer, M. Smits, A. Scrinzi, and T. Brabec, *Phys. Rev. A* **70**, 041401 (2004).
- [29] J. Caillat, J. Zanghellini, M. Kitzler, O. Koch, W. Kreuzer, and A. Scrinzi, *Phys. Rev. A* **71**, 012712 (2005).
- [30] E. Runge and E. K. U. Gross, *Phys. Rev. Lett.* **52**, 997 (1984).
- [31] *Density Functionals: Theory and Applications*, edited by D. Joubert (Springer, Berlin Heidelberg, 1998).
- [32] *A Primer in Density Functional Theory*, edited by C. Fiolhais, F. Nogueira, and M. A. L. Marques (Springer, Berlin Heidelberg, 2003).

-
- [33] *Time-Dependent Density Functional Theory*, edited by M. A. L. Marques, C. A. Ullrich, F. Nogueira, A. Rubio, K. Burke, and E. K. U. Gross (Springer, Berlin Heidelberg, 2006).
- [34] C. A. Ullrich, S. Erhard, and E. K. U. Gross, in *Super Intense Laser Atom Physics IV*, edited by H. G. Muller and M. V. Fedorov (Springer, Netherlands, 1996), pp. 267–284.
- [35] V. Vényard, R. Taïeb, and A. Maquet, Phys. Rev. A **65**, 013202 (2001).
- [36] V. Vényard, R. Taïeb, and A. Maquet, Laser Phys. **13**, 465 (2003).
- [37] D. Bauer, Phys. Rev. A **56**, 3028 (1997).
- [38] D. G. Lappas and R. van Leeuwen, J. Phys. B: At. Mol. Opt. Phys. **31**, L249 (1998).
- [39] D. Bauer and F. Ceccherini, Opt. Express **8**, 377 (2001).
- [40] M. Petersilka and E. K. U. Gross, Laser Phys. **9**, 105 (1999).
- [41] N. T. Maitra, K. Burke, H. Appel, E. K. U. Gross, and R. van Leeuwen, in *Reviews in Modern Quantum Chemistry*, edited by K. D. Sen (World Scientific, Singapore, 2002), pp. 1186–1225.
- [42] D. Bauer, *Theory of Intense Laser-Matter Interaction*, www.mpi-hd.mpg.de/keitel/dbauer/pdf/tilmi.pdf, (2006).
- [43] P. Hohenberg and W. Kohn, Phys. Rev. **136**, B864 (1964).
- [44] R. van Leeuwen, Int. J. Mod. Phys. B **15**, 1969 (2001).
- [45] M. Lein and S. Kümmel, Phys. Rev. Lett. **94**, 143003 (2005).
- [46] R. van Leeuwen, Phys. Rev. Lett. **80**, 1280 (1998).
- [47] J. Schirmer and A. Dreuw, *private communication*, (2006).
- [48] M. Lein, E. K. U. Gross, and V. Engel, Phys. Rev. Lett. **85**, 4707 (2000).
- [49] N. E. Dahlen and R. van Leeuwen, Phys. Rev. A **64**, 023405 (2001).
- [50] A. S. de Wijn, S. Kümmel, and M. Lein, Verhandlungen der DPG (Frühjahrstagung, Frankfurt, 2006), 49 (2006).
- [51] J. P. Perdew, R. G. Parr, M. Levy, and J. L. Balduz, Phys. Rev. Lett. **49**, 1691 (1982).
- [52] M. Mundt and S. Kümmel, PRL **95**, 203004 (2005).
- [53] A. S. de Wijn, S. Kümmel, and M. Lein, *to be published* (2006).

- [54] A. D. Becke, J. Chem. Phys. **88**, 1053 (1988).
- [55] J. P. Perdew and Y. Wang, Phys. Rev. B **46**, 12947 (1992).
- [56] J. C. Kimball, J. Phys. A: Math. Gen. **8**, 1513 (1975).
- [57] A. K. Rajagopal, J. C. Kimball, and M. Banerjee, Phys. Rev. B **18**, 2339 (1978).
- [58] F. Wilken and D. Bauer, Phys. Rev. Lett. *accepted* (2006).
- [59] F. Schwabl, *Quantenmechanik* (Springer, Berlin Heidelberg, 2002).
- [60] H. Rottke, X. Liu, E. Eremina, W. Sandner, E. Goulielmakis, K. O. Keeffe, M. Lezius, F. Krausz, F. Lindner, M. G. Schätzel, G. G. Paulus, and H. Walther, J. of Mod. Opt. **53**, 149 .
- [61] P. Koval, F. Wilken, D. Bauer, and C. H. Keitel, Phys. Rev. *submitted* (physics/0609010) (2006).
- [62] D. B. Milošević, G. G. Paulus, D. Bauer, and W. Becker, J. Phys. B: At. Mol. Opt. Phys. **39**, R203 (2006).
- [63] A. L’Huillier, P. Balcou, S. Candel, K. J. Schafer, and K. C. Kulander, Phys. Rev. A **46**, 2778 (1992).
- [64] B. Sundaram and P. W. Milonni, Phys. Rev. A **41**, 6571 (1990).
- [65] K. Burnett, V. C. Reed, J. Cooper, and P. L. Knight, Phys. Rev. A **45**, 3347 (1992).
- [66] S. C. Rae, X. Chen, and K. Burnett, Phys. Rev. A **50**, 1946 (1994).
- [67] R. Kienberger, M. Hentschel, M. Uiberacker, C. Spielmann, M. Kitzler, A. Scrinzi, M. Wieland, T. Westerwalbesloh, U. Kleineberg, U. Heinzmann, M. Drescher, and F. Krausz, Science **297**, 1144 (2002).
- [68] J. Crank and P. Nicolson, Proc. Cambridge Philos. Soc. **43**, 50 (1947).
- [69] D. Bauer and P. Koval, Comput. Phys. Comm. **174**, 396 (2006).
- [70] D. Neuhasuer and M. Baer, J. Chem. Phys. **90**, 4351 (1989).
- [71] C. Buth, R. Santra, and L. S. Cederbaum, Phys. Rev. A **69**, 032505 (2004).

Acknowledgment

In the course of obtaining the results presented in this diploma thesis I was privileged to enjoy the extensive support of Priv.-Doz. Dr. Dieter Bauer. His excellent supervision and impressive knowledge paired with an openness for discussions were a constant source of motivation.

In addition, stimulating contact with Prof. Dr. Manfred Lein helped to focus some of the approaches presented in this work. I very much appreciated the interesting professional (and private) conversations with many researchers and students at the Max Planck Institute for Nuclear Physics. Furthermore, I am very happy that Prof. Dr. Peter Schmelcher has agreed to serve as a referee for this work.

Finally, I would like to thank Heidemarie Wilken and Bernd Flach-Wilken for backing me financially as well as personally and Kathrin Reinhold for supporting me in every way possible during the past year.

Erklärung gemäß Prüfungsordnung

Ich versichere, daß ich diese Arbeit selbständig verfaßt und keine anderen als die angegebenen Quellen oder Hilfsmittel benutzt habe.

Heidelberg, den

(Florian Wilken)

